ISSN:2538-516X

Journal of Civil Engineering Researchers

Volume: 4; Number: 1; March 2022

J-Researchers

J-Researchers

JOURNAL OF CIVIL ENGINEERING RESEARCHERS

Volume 4, Number 1, March 2022

Contents

JOURNAL OF CIVIL ENGINEERING RESEARCHERS

Evaluation of an aftershock Effect on Steel moment frame structures in various soil types

Javad Pourali[a] , Ehsan Omranian[b] , Gholamreza Abdollahzadeh[b],*

[a] Engineering Faculty, Chaloos Branch, Islamic Azad University, Chaloos 46615-397, Iran

[b] Faculty of Civil Engineering, Babol Noshirvani University of Technology, Babol, Iran

Article History: Received 30 December 2021; accepted 19 February 2022.

Abstract

The aftershocks may weaken or collapse structures that were previously damaged under the main earthquake and have not yet been repaired. In this paper, the seismic performance of an 8-story Steel moment frame structures designed in four types of soil is evaluated under the seismic sequence of earthquake and aftershock. The results showed that the seismic performance of the studied frame under the influence of severe aftershocks can be significantly different from the main earthquake mode alone. For example, in type 1 soil, aftershocks can increase the structure displacement by more than 50% compared to the main earthquake mode alone. It was also found that most aftershocks cause a significant increase in the durable displacement of the roof and in a small number of cases it also reduces it. In addition, the impact of aftershocks on the building damaged by the main earthquake will be much greater than in the case in which the structure under the main earthquake has not suffered much damage.

"Keywords: Aftershock, Mainshock, Seismic sequence, Steel moment frame, Residual inter-story drifts"

1. Introduction

The earthquake is a natural phenomenon that has repeatedly horrled man in human history and has destroyed many cities and villages along with severe human and financial casualties. Historical evidence has shown that large earthquakes are often followed by repeated aftershocks and form a sequence of earthquakes and aftershocks. Strong aftershocks can increase the level of damage to structures with new damage and may also cause weakening or collapse of structures that were previously damaged under the main earthquake. (But, due to the short time between the occurrence of the aftershock and the main earthquake, they have not been repaired yet)[1]. An example of this is the main earthquake in Chile on February 27, 2010 (Mw = 8.8), which caused severe damage to the southern and central regions of Chile with 360 aftershocks with a magnitude of more than5 between February 27 and April 26. Among these aftershocks were 21 magnitudes greater than 6 [9]. The first analytical study on the nonlinear behavior of single-degree-of-liberty (SDOF) systems exposed to the time-history records of the 1972 Managua Post-

Earthquake was conducted by Mahin (1980). He observed that displacement demand ductility (the ratio of maximum inelastic displacement to system yield displacement) in elastoplastic SDOF systems at the end of the main aftershock increases slightly relative to the original earthquake. Mahin examined the effects of this sequence on structures by setting two records of major earthquake and aftershock. This had one major drawback; it did not take into account the effects of the system's free vibration on the distance between the main earthquake and the aftershock. In subsequent studies, a time interval between the main earthquake and the aftershock was considered and it was assumed that at this distance the system would stop moving. Later, some other researchers used a distance of 20 to 100 seconds in their research depending on the type of structures [4,5]. In fact, this time interval is considered only to end the free vibration time of the system, which by examining the behavior of the structures studied in this study, 40 seconds was found to be a suitable number. Figure 1 shows a schematic of how earthquake and aftershock acceleration maps are placed one after the other.

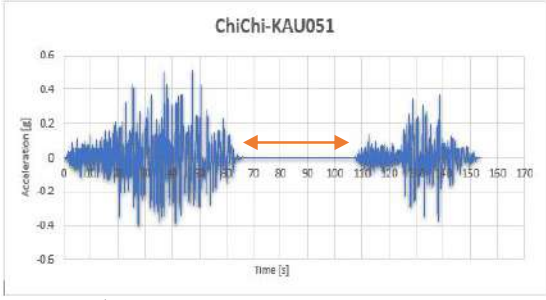

figure 1. How to place the acceleration of earthquake and aftershock

Garcia (2012) examined the characteristics of a wide range of earthquakes and corresponding aftershocks on the seismic response of buildings and showed that the dominant period, as well as the duration of the main earthquake and aftershocks, were statistically weakly correlated. Therefore, the production of artificial seismic sequences from the main earthquake as a basis for the production of aftershocks, even with a smaller amplitude, does not make sense because the frequency and duration of the earthquake are completely different [7]. Therefore, it can be said that it is necessary to use real data to evaluate the performance of existing structures under seismic sequences. Abdullahzadeh et al. (2017) with the help of real seismic sequences and by examining the energy distribution in buildings designed by conventional elastic methods as well as modern plastic design methods based on performance, found that aftershocks have a destructive effect on floors that suffer more damage under the main earthquake. Have seen will have [8]. Recently, several researches have been conducted in the field of seismic evaluation of structures under seismic sequences, in all of which the effect of aftershock in increasing the vulnerability of the structure has been confirmed [10,11]. However, design codes still do not explicitly consider the effects of aftershocks and the cumulative damage caused by them in the design of earthquake-resistant structures. The reason for this is probably due to the many uncertainties in the capacity of structures damaged after the main earthquake, the complexity of aftershock characteristics and the probability of their occurrence and the general lack of system fragility models to evaluate the performance of structures [2, 12].

2. Modeling

To evaluate the vulnerability of MDOF structures (several degrees of freedom) under the effect of earthquake and aftershock sequence, an 8-story building in Tehran of medium steel bending frame type in 4 types of soil (A, B, C, & D) based on LRFD method Article 10 of the National Building Code and the fourth edition of Standard 2800 [6] were designed. These structures have three openings of 5 meters in each direction and the height of the floors is 3.2 and the height of the parking lot is 2.7. First, the design of this building was done according to the residential use and located on a relatively high-risk area according to the definition of 2800 standard with the help of Etabs software. Then, for two-dimensional analysis of the critical frame, the selection and seismic performance of this frame were evaluated using time history analyzes by applying natural earthquake and aftershock records using OpenSees finite element software. Figure 3 shows the three-dimensional and two-dimensional views of the designed frame.

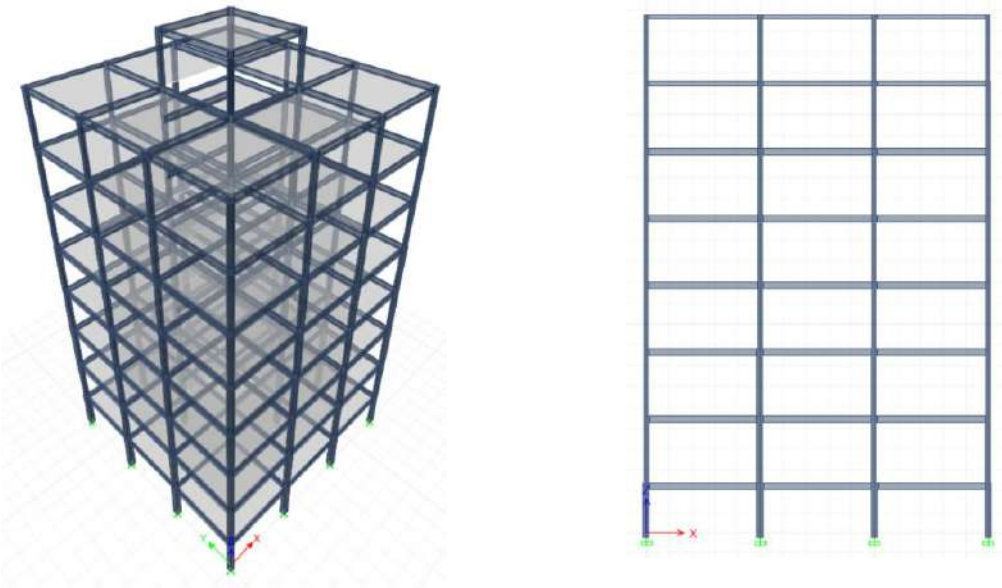

Figure 3. Three-dimensional and two-dimensional view of the designed frame

In the definition of steel, non-linear materials (steel02) in the OpenSees material library were used and the cross-section of the members was made of fiber.This command separates the cross section into smaller areas and summarizes the stress-strain response of the materials for these areas to obtain the resultant behavior. Tables 1 and 2 provide a list of sections designed in the critical frame.

Table No. 1- List of designed beam sections

Type C soil	Type C soil	Type B soil	Type A soil
PG-W180X6-F150X10	PG-W180X6-F150X8	IPE180	**PG-W180X6-F150X8**
PG-W240X6-F150X12	PG-W180X6-F150X15	IPE240	**PG-W180X6-F150X10**
PG-W240X6-F150X15	PG-W300X6-F150X10	IPE270	**PG-W200X8-F150X10**
PG-W350X6-F150X20	PG-W300X6-F150X12	IPE300	**PG-W240X6-F150X8**
PG-W400X6-F150X12	PG-W300X6-F150X15	PG-W250X8-F200X12	**PG-W300X6-F150X10**
PG-W400X6-F150X25	PG-W300X6-F150X20	PG-W250X8-F200X15	**PG-W240X6-F150X12**
		PG-W300X8-F200X15	

Table 2 - List of designed sections of the column

Type C soil	Type C soil	Type B soil	Type A soil
BOX240X15	BOX180X8	BOX150X10	BOX180X8
BOX250X8	BOX200X8	BOX200X10	BOX200X8
BOX250X10	BOX200X10	BOX200X12	BOX200X10
BOX250X12	BOX200X12	BOX200X15	BOX240X10
BOX250X20	BOX240X10	BOX250X10	BOX240X12
BOX300X20	BOX240X12	BOX250X12	BOX240X20
	BOX240X15	BOX250X15	
	BOX240X20	BOX250X20	
	BOX300X20		

Past studies have shown that records must be scaled to the desired hazard level to achieve proper seismic behavior [3]. In this study, 12 raw accelerometers were extracted from PEER site data in accordance with the soil type and were compared and scaled according to the instructions of the fourth edition of the 2800 standard. Table 3 shows the characteristics of each of the corresponding earthquake and aftershock accelerometers.

Table No. 3- Characteristics of earthquake and aftershock acceleration

Soil Type	Name of earthquake	Station	Magnitude of earthquake	magnitude of the aftershock	Shear wave velocity
A	Chi-Chi	HWA002	7.62	6.2	789
	Chi-Chi	KAU051	7.62	6.2	1004
	Northridge	WONDERLAND	6.69	5.28	1222
B	Chi-Chi	CHY074	7.62	6.2	665
	Mamooth	Long valley dam	6.06	5.91	496
	Northridge	Pacoima Kagel Canyon	6.69	5.28	550
C	HOLISTER	Holister	5.6	5.5	198
	Imperial Valley	Holtvile	6.53	5.01	202
	Northwest	Jiashi	6.1	5.8	240
D	Chi-Chi	CHy054	7.62	6.3	172
	Chi-Chi	ILA044	7.62	6.3	160.6
	Whittier	Carson	5.99	5.27	160

It should be noted that regarding the scale of aftershocks, the adaptation coefficient was used to maintain the PGA ratio of earthquake and aftershock. According to Table 4, the ratio of PGA aftershock to the main earthquake is:

TABLE 4 - RATIO OF PGA AFTERSHOCK TO MAIN EARTHQUAKE

SOIL TYPE	Name of earthquake					
A	Chi-Chi-KAU051		Northridge-Wonderland		Chi-Chi-HWA002	
	pga after / pga ma	**-0.7365**	pga after / pga ma	**0.528706**	pga after / pga ma	**0.353661**
B	Chi-Chi-CHY074		Mamooth-Long valley Dam		Northridge-Pacomia	
	pga after / pga ma	**-1.3782**	pga after / pga ma	**1.1206**	pga after / pga ma	**-0.50448**
C	Northwest-Jiashi		Holister-Holister		Imperial-Holtvile	
	pga after / pga ma	**0.873402**	pga after / pga ma	**-0.61133**	pga after / pga ma	**-0.44463**
D	Chi-Chi-CHy054		Whittier-Carson		Chi-CHi-ILA044	
	pga after / pga ma	**-0.80387**	pga after / pga ma	**0.443668**	pga after / pga ma	**0.367758**

3. Comparison of floor drift distribution

The frames are exposed to the seismic sequences of the accelerometers presented in Table 3 under time history analysis, and the drift changes of the classes in height are shown in Figures 1 to 4. As can be seen from the diagrams for floor drift in four soils, aftershocks in some cases lead to a sharp increase in structural drift, for example in the Northridge Earthquake type A soil in some floors (such as the 7 floor). The quake has more than doubled. In the Chi-Chi earthquake, kau041 also increased slightly. But in chici-HWA002 earthquake, no increase in structural drift was observed. This issue is justified by the very low intensity of aftershocks in the recent earthquake. In the chici-HWA002 earthquake, the maximum ground acceleration (PGA) of the aftershock was 35% of the main earthquake and therefore the main damage occurred during the main earthquake And aftershock damage did not have much on the main structure. However, according to the 2800 standard guidelines, if these three records are selected for design, maximum results should be used. Therefore, it is observed that aftershocks can have very destructive effects (increasing displacement up to more than double) that ignoring these effects in the design process can have catastrophic consequences during an earthquake. Another issue that seems to be important is the change of drift direction. . For example, in the structure under study under the Northridge earthquake, the fifth-floor drift caused by the main earthquake is equal to - 0.25% while this value has reached + 0.25% during the aftershock. This change in drift direction may cause severe damage to the structure, and it is possible that the structure will not be able to withstand such a deformation during severe earthquakes.

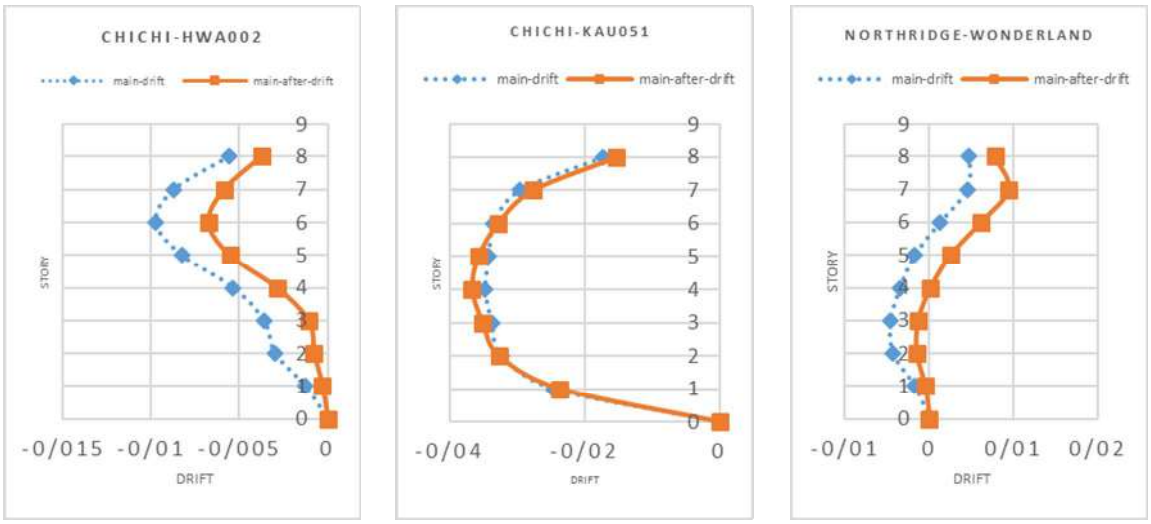

Graphs 1. Type A soil drift change diagrams

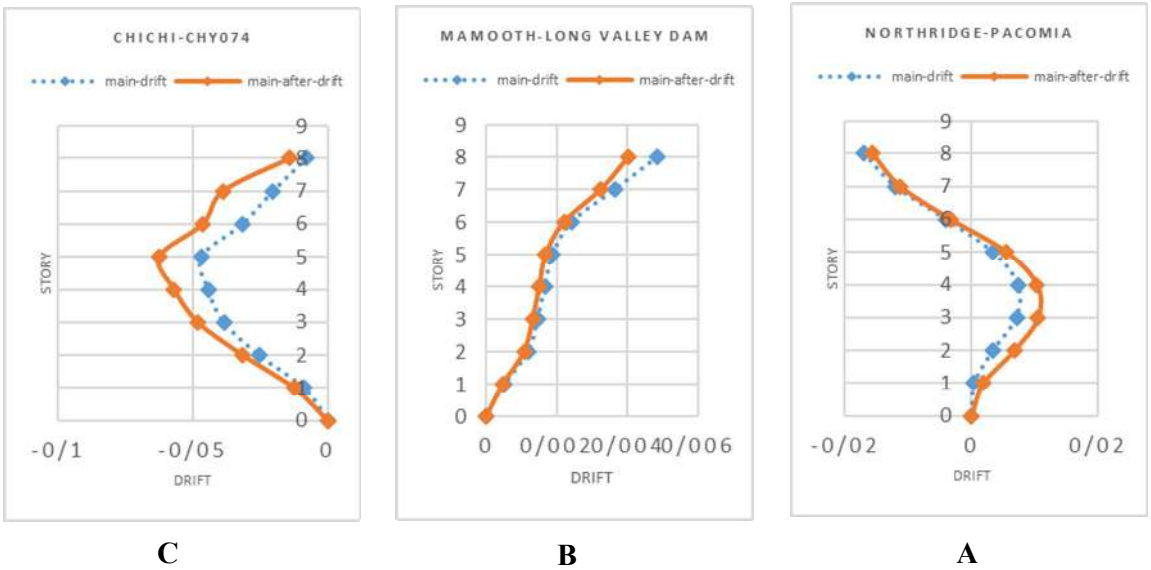

C

Graphs 2. Type B soil drift change diagrams

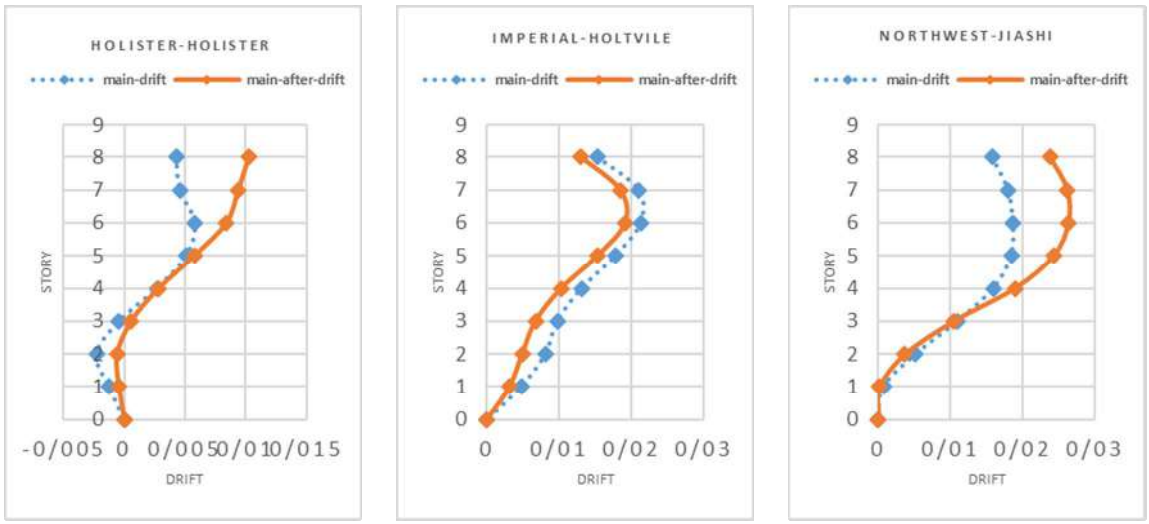

C **B** **A**

Graphs 3. Type C soil drift change diagrams

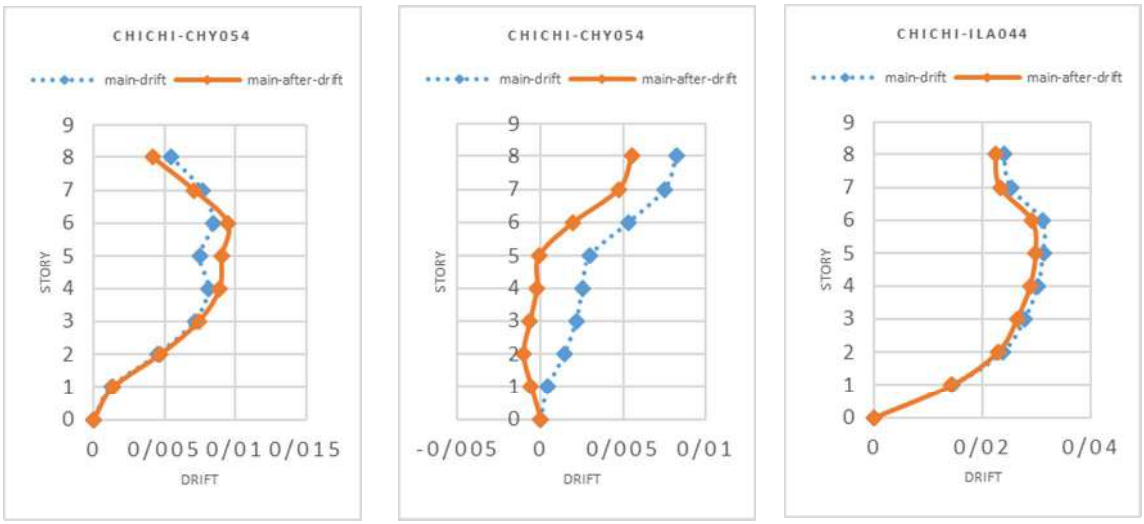

C **B** **A**

Graphs 4. Type D soil drift change diagrams

4. Comparison of permanent displacement distribution of floors

Examining the drift distribution of floors at the collapse level of the damaged structure, it was found that with the increase of damage under the main earthquake, the distribution of damage is more concentrated in the same floors damaged in the main earthquake, while the same record in a healthy structure causes the failure of another floor.Comparison of permanent displacement distribution of floors. Finally, the remaining displacement of the elements in both healthy and damaged structures is investigated. The parameter of relative displacement, which is considered as a good representative for damage to structural members, also strongly depends on the type of damage caused by the main earthquake. The drift changes of the floors in the primary and damaged structures in different soil types are shown in Figures 5 to 9. As can be seen from Figures 5 to 9, the permanent displacement of the roof under the effect of seismic sequence is sometimes less than the permanent displacement of the roof under the effect of the main earthquake alone. This phenomenon expresses the important issue that aftershocks do not necessarily increase the permanent displacement of the structure. In examining the permanent displacement of the roof, it should be noted that the structure may not stop at its maximum permanent displacement due to successive earthquakes and as a result have less permanent displacement, although in this case, the damage to the structure has increased.

Tables 4 to 8 show the ratio of residual displacement of the structure under a series of earthquakes compared to the main earthquake.

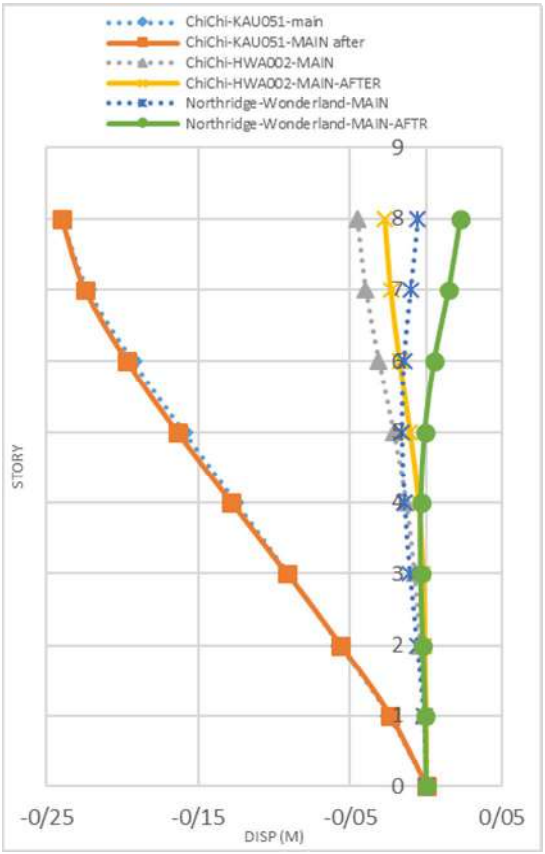

Chart 5. Permanent displacement diagrams Soil type A.

Table 4- Ratio of displacement ratio of the structure under the effect of the seismic sequence in comparison with the main earthquake In type A soil

Record name	floors							
	ST8	ST7	ST6	ST5	ST4	ST3	ST2	ST1
ChiChi-HWA002	0.59	0.58	0.55	0.49	0.38	0.27	0.25	0.24
Northridge-Wonderland	-4.04	-1.42	-0.35	0.06	0.24	0.33	0.34	0.3
ChiChi-KAU051	1	1.01	1.02	1.03	1.02	1.01	0.99	0.96

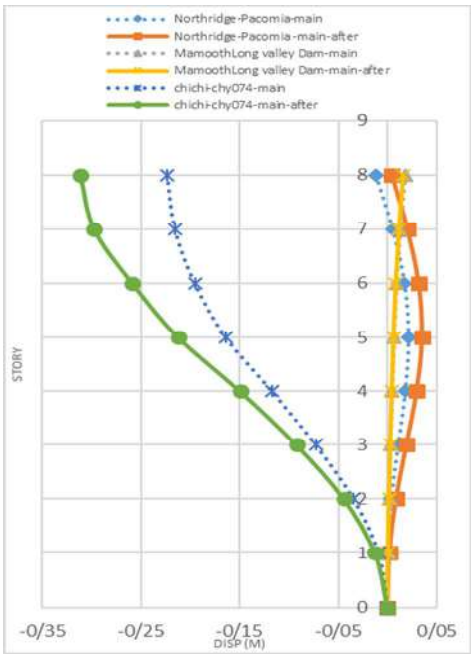

Chart 6. Permanent displacement diagrams Soil type B.

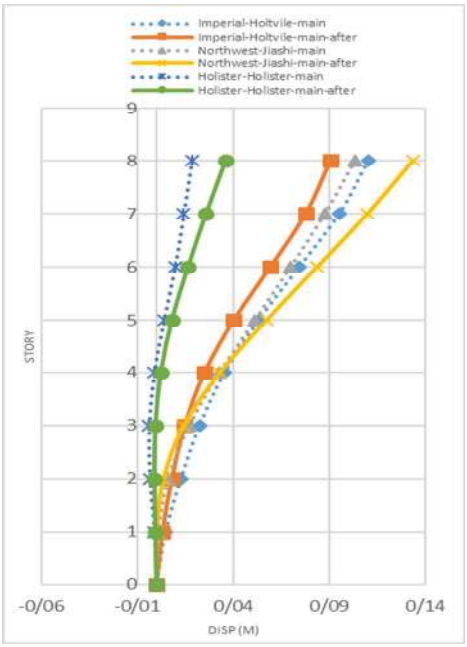

Chart 7. Permanent displacement diagrams Soil type C.

Table 5- Ratio of displacement ratio of the structure under the effect of the seismic sequence in comparison with the main earthquake In type B soil

Record name	floors							
	ST8	ST7	ST6	ST5	ST4	ST3	ST2	ST1
MamoothLong valley Dam	0.88	0.90	0.90	0.90	0.90	0.90	0.90	0.91
NorthridgePacomia	-0.39	3.92	1.82	1.62	1.62	1.77	2.32	4.91
chichichy074	1.40	1.38	1.33	1.30	1.28	1.27	1.29	1.43

Table 6- Ratio of displacement ratio of the structure under the effect of the seismic sequence in comparison with the main earthquake In type C soil

Record name	floors							
	ST8	ST7	ST6	ST5	ST4	ST3	ST2	ST1
MamoothLong valley Dam	0.88	0.90	0.90	0.90	0.90	0.90	0.90	0.91
NorthridgePacomia	-0.39	3.92	1.82	1.62	1.62	1.77	2.32	4.91
chichichy074	1.40	1.38	1.33	1.30	1.28	1.27	1.29	1.43

Table 7- Ratio of displacement ratio of the structure under the effect of the seismic sequence in comparison with the main earthquake In type D soil

Record name	floors							
	ST8	ST7	ST6	ST5	ST4	ST3	ST2	ST1
Imperial-Holtvile	0.82	0.82	0.80	0.76	0.71	0.66	0.63	0.67
Northwest-Jiashi	1.29	1.25	1.20	1.12	1.01	0.85	0.65	0.19
Holister-Holister	1.94	1.81	1.70	2.09	-1.78	0.13	0.30	0.36

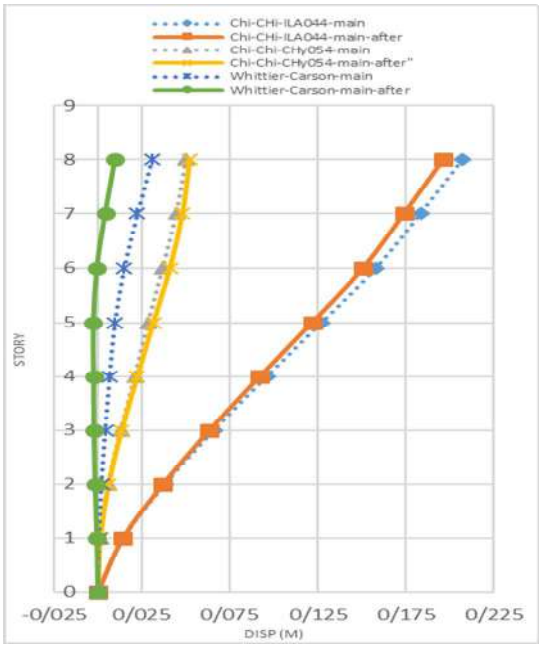

Chart 8. Permanent displacement diagrams Soil type D.

5. Conclusion

To evaluate the response of steel MDOF structures under the effects of seismic sequencing, an 8-story building with medium Steel moment system in 4 types of soil (A, B, C & D) was designed according to version 4 of 2800 standard by LRFD method. Then, the most critical frame of each structure was selected for modeling in opensees software and finally, the performance of steel bending frames was investigated through applying natural records of an original earthquake and scaled aftershock according to standard criteria 2800 in terms of maximum relative displacement within the floor and relatively lasting displacement which is considered as a good representative for structural organ damage and the following results were obtained.

1- The distribution of structural drift in each accelerometer is different. For example, in the acceleration of the Northridge Earthquake type A, the drift of the 6th and 7th floors had the highest increase, but in the 051 earthquake - Chi-Chi, the drift of the 3rd and 4th floors increased. However, aftershocks can sometimes have severe effects on the displacement of the structure and can even increase displacement by more than 50% in the structure (such as soil structure type 1 under earthquake and North Earthquake aftershocks), so aftershocks should be used in conventional designs. Be considered

2- Comparing the residual displacement of the elements in the two healthy and damaged structures, it was found that the residual displacement in the damaged structure is strongly dependent on the type of damage caused in the main earthquake. In fact, depending on the category of damage caused by the earthquake to the healthy structure, the focus of damage in the damaged structure has changed. This result can be seen due to the shape of the behavioral curves for structures with different percentages of damage. In some stimuli, there was no significant difference between the behavior of damaged and healthy structures.

3- By examining the drift distribution of floors in the collapse level of the damaged structure, it was found that with the increase of damage under the main earthquake, the distribution of damage is more concentrated in the same damaged floors in this earthquake, while the same record in a healthy structure causes damage in another floor.

References

1. G. yeo & A. Cornell S(2005)"tochastic Characterization and Decision Bases under Time-Dependent Aftershock Risk in Performance-Based Earthquake Engineering", PEER report.

2. Nazari. N, De Lindt.W, Li.Y,(2015)"Quantifying Changes in Structural Design Needed to Account for Aftershock Hazard", Journal of Structural Engineering.

3. Kiani, J. and Khanmohammadi M. (2015). New approach for selection of real input ground motion records for incremental dynamic analysis

(IDA). Journal of Earthquake Engineering 19, no. 4: 592-623.

4. Mahin SA. (1980) *Effects of duration and aftershocks on inelastic design earthquakes*. In: Proceedings of the seventh world conference on earthquake engineering. vol. 5. p. 677–9.

5. Fragiacomo M, Amadio C, Macorini L. (2004) *Seismic response of steel frames under repeated earthquake ground motions*. Eng Struct;26:2021–35.

6. Earthquake Design Regulations, Standard 7, Edition 4, Building and Housing Research Center, Journal No. Z-1, First Edition 2014

7. Ruiz-Garcia J. Mainshock–aftershock ground motion features and their influence in building's seismic response. Journal of Earthquake Engineering 2012; 16(5):719–37.

8 Abdollahzadeh G.R., Mohammadgholipour A., Omranian E. (2017). Seismic evaluation of steel moment frames under mainshock-aftershock sequence designed by elastic design and PBPD methods Journal of Earthquake Engineering, (accepted).

9. Banon, H.,J.M.Biggs, and H.M.Irvine.."seismic Damage of Reinforced Concrete Frames." Journal of the structural Division,ASCE 107 (ST9) 1713-1981-1729

10. Hosseinpour F., and Abdelnaby A. E. (2017). Fragility curves for RC frames under multiple earthquakes. Soil Dynamics and Earthquake Engineering 98: 222-234.

11. Omranian E, Abdelnaby A. E., Abdollahzadeh Gh.R, Rostamian M., Hosseinpour F., Fragility Curve Development for the Seismic Vulnerability Assessment of Retrofitted RC Bridges under mainshock-aftershock seismic sequences, Structures Congress 2018 (accepted).

12. Abdelnaby, A. E.(2012)"Multiple earthquake effects on degrading reinforced concrete structures." Doctoral dissertation, Univ. of Illinois, Urbana-Champaign, IL.

J-Researchers

JOURNAL OF CIVIL ENGINEERING RESEARCHERS

Analytical and Experimental Study of Load-bearing Beams Made of Lightweight Concrete

Ghasem Azizi Daronkolaie

Phd student, Department of Civil Engineering, Islamic Azad University of Chalous

Journals-Researchers use only: Received: 07 February 2022; Accepted: 29 April 2022

Abstract

In recent years, the use of lightweight concrete in the world has grown exponentially. The reason is the lightening of the building and as a result the reduction of dead load and seismic force on the structures as well as better performance in terms of thermal insulation and energy saving. Therefore, it is necessary to study the potentials of using lightweight concrete in the construction industry. In this article, which is the result of analytical and experimental results about a special type of lightweight aggregate called Leica, the aim is to first achieve a lightweight concrete mixing design that has the necessary conditions as lightweight structural concrete. In this paper, during laboratory research, using Leica concrete grain style with an approximate compressive strength of 20 MPa and a specific gravity of approximately 1800 kg / m3 was obtained. Secondly, we investigated the structural behavior of concrete beams made with Leica lightweight aggregate experimentally and numerically. For this purpose, the first 5 concrete beams were made and examined in the laboratory, and finally, using ABAQUS finite element software, a suitable model was found to model such beams, which is in good coordination with the laboratory results. The compatibility of the results obtained from the modeling with the laboratory results is proof of the accuracy of the constructed model.

Keywords: Lightweight concrete beam, Finite element analysis, Laboratory study, Bending behavior of beams, ABAQUS

1. Introduction

Concrete includes aggregates, cement, and water, since aggregates account for 60 to 70% of the weight of concrete, so the idea of lightening them to produce lightweight concrete has been proposed. One of the main problems in the design and construction of buildings is the significant weight of the dead load, which is mainly due to the weight of the roofs and partition walls. Obviously, the use of lightweight materials reduces the dead load and thus reduces the weight of beams, columns, and foundations, which will ultimately lead to the economy of the design[1].

In recent years, the use of lightweight concrete in various forms such as lightweight concrete, fine-grained concrete, or concrete with air bubbles, has become very common and due to its unique advantages such as low specific gravity and good thermal insulation, in many cases, it has replaced ordinary concrete [2].

The low strength of lightweight concrete has been an important factor in limiting the scope of application of this type of concrete and taking advantage of it. Lightweight concrete that has sufficient strength and other physical properties have been improved due to weight loss will create a huge change in the use of this concrete. By consuming high-quality grains under special conditions, light concrete with a compressive strength of up to 500 kg/cm^2 can be obtained, and with the help of micro silica and superplasticizers, they have been able to increase the compressive strength of light concrete up to 700 kg/cm^2 and in some cases up to 1000 kg/cm^2 increase.

Grains weighing less than 1120 kg/cm^3 are generally considered light grains [3]. For comparison, themost common aggregates such as sand and gravel weigh about 1520 kg/cm^3 to 1680. The light grain has a low specific gravity due to its high porosity. Grains are classified according to their sources, production methods, and final application.

In general, the properties of lightweight aggregates and their products such as lightweight aggregate concrete including expanded clays, pumice, perlite, etc. can be summarized as follows:

- Low specific gravity, which reduces the dead load of the building and thus changes the physical characteristics of the design.
- Heat and sound of this property is due to the pores in the grain.
- Fire resistance; It is usually unlikely that the temperature of the fire will be higher than the temperature produced by these materials (about 1200 ° C).
- Qualitative resistance to freezing and re-melting.
- Neutral chemically.

Lightweight concrete refers to concretes that have a specific weight between 300 and 1850 kg/m^3. There are three general methods of producing lightweight concrete. In the first method, light porous materials with low specific gravity are used instead of ordinary aggregates. The resulting concrete is called lightweight concrete. The second method of producing lightweight concrete is based on creating several pores inside the concrete or mortar. These pores must be clearly cleaned of very small pores with air bubbles. This type of concrete is known as "sponge concrete", "aerated concrete" or "aerated concrete". The third method of producing lightweight concrete is to remove fine aggregates from the concrete mix so that numerous pores are created between the particles, and generally coarse aggregates with normal weight are used. This type of concrete is called "fine-grained concrete".

Despite the high cost of lightweight aggregates and the additional initial cost of using lightweight concrete, the total cost of a structure made of lightweight concrete is lower than conventional concrete. The use of lightweight concrete in prefabricated structures reduces its weight by half, which saves transportation costs. This savings well offsets the additional costs of lightweight aggregates. Sometimes the dead load is a prefabricated piece close to or more than the crane used in the factory or workshop. It also reduces crane movements. The economic advantages of using lightweight concrete are as follows [4]:

- Saving energy consumption and the possibility of using simple and technical labor.
- Saving energy consumption required to move building materials and transport them to different floors.
- Save on iron consumption.
- Significant savings in transporting building materials from the factory to the place of consumption.
- Saving energy consumption during the life of the structure.
- Impact of environment and climate on energy savings due to reduced air pollution.
- Saving during the construction of the building.
- The building becomes more resistant to earthquakes due to the reduction of dead load.

Due to the general desire to optimally design the structure so that while maintaining the durability and stability of the structure, costs are also reduced, so the use of lightweight concrete is a good solution in addition to reducing the dead load on the structure, the seismic force Significantly reduces. Therefore, in this study, we decided to study the structural behavior of lightweight concrete beams in a laboratory and then in order to develop studies and due to laboratory limitations and time and volume of testing, a finite element model suitable for test beams. We have found it so that it can be used for further studies in the future.

The second part of this article is an overview of light concrete research. In the third part, the studies were described, which are in two phases of laboratory and modeling with ABAQUS software. In the fourth part, the obtained results are examined, and finally, in the fifth part, the general conclusion is given.

2- Related Works

In [5] the flexural behavior of beams of lightweight concrete structures has been investigated and the flexural deformation, cracking behavior, and development of strains in the mill have been investigated. In this experiment, calcareous aggregates were used as lightweight coarse grains to produce lightweight concrete. Also, 6 different beams were made for the experiments. The test results showed that in the elastic stage and the beginning of

the first stage is larger than the other stages Lightweight concrete beams This stage is larger than the other stages and the reinforcement of lightweight concrete beams surrenders before the reinforcement of ordinary concrete beams. Also, crack distribution behavior and rupture behavior are similar for lightweight concrete structural beams and ordinary concrete.

In [6] Experimental research on the flexural behavior of structural beams made of lightweight concrete with oil palm pumice was performed, which examined features such as flexural deformation, cracking behavior, and ductility indices. The use of palm oil in lightweight concrete not only helps to solve the problem of disposal of these solid wastes but also helps to preserve natural resources. A total of 6 structural beams with different reinforcement ratios (0.52% to 3.9%) were used. All lightweight concrete beams show the usual structural behavior in bending in beams with low reinforcement before Compression of compressive concrete in the area of pure bending, flowing occurs in tensile reinforcement. They also show good ductile behavior and the width of the cracks in the loads do not exceed the allowable limit.

In [7], the flexural behavior and the effect of beams made of lightweight concrete structures were investigated. In this experiment, six bending beams with different dimensions and variable reinforcement ratios (from 0.33% to 1.3%) were used. Took. The designed compressive strength of concrete was 34 MPa. The test results showed that lightweight granular concrete beams have the same load capacity and fracture mode as normal weight concrete beams, but show greater flexural deformation and flexural ductility. The flexural ductility of both types of concrete beams decreases as the reinforcement ratio increases. On the other hand, increasing the beam dimensions leads to increased loading and flexural deformation in the flow strength and ultimate strength.

In [8], the bending behavior of structural beams made of lightweight concrete and ordinary concrete is predicted. In this study, the structural neural network (ANN) method was used to predict the flexural deformation values of the beams and compare the test results. In this test, 6 beams of concrete structures with rectangular cross-sections were prepared and subjected to net bending. Lightweight concrete structural beams had advantages over conventional concrete structural beams such as lower weight, lower seismic forces due to reduced volume, good thermal and acoustic insulation. The analytical results were compared with the test results and predictions by the neural network process in determining the amount of flexural deformation.

In [9] examines the applicability of shear models for deep beams with lightweight aggregate concrete. Tests were conducted to investigate the effects of shear span-to-effective depth ratio (a/d), ranging from 0.26 to 1.04, and an effective span–depth ratio (le/h), ranging from 2 to 3, on the failure mode and shear behavior of deep beams. Failure from the flexure mode showed a dominant pattern with increasing a/d. The le/h value minimally influenced the diagonal cracking and ultimate strength of deep beams. In contrast, a/d significantly affected the beam strength. These comparisons indicated that all of these shear methods can be used to predict the shear strength of lightweight aggregate concrete deep beams.

3- Laboratory Studies and Modeling

The main purpose of this study is to achieve lightweight structural concrete with lower specific gravity and higher compressive strength. Accordingly, in this experiment, 5 cubic samples were made of 10 × 10× 10 cm and after 28 days of curing in water, its specific gravity and compressive strength were determined.

3.1. Consumable materials

In this research, the cement used is Portland type 2 Neka and the water used is drinking water in Babol city. The micro-silica used in this research was in the form of a powder produced by Vand Shimi Company, whose specific particle surface is 20 m2 / gr. In this study, 10% of the weight of cement was replaced with micro silica and the amount of cement was reduced by the same amount. PCE superplasticizer was also used. Consumed sand was first passed through a sieve with a score of 4, so 0-5 mm of sand was used in concrete. Its modulus of softness is equal to 2.6 The grain size of the consumed sand has acceptable compliance with the allowable range related to natural sand.

In this research, in order to clean the sands, first, the existing sands were washed and then sieved and used in the concrete mixing design. Natural sand has been used instead of 0.5 mm Leica grains. The one-hour water absorption of Leica seeds is 11.3%. For granulation, 500 g of Leica was selected. The light aggregate tested does not have acceptable compliance with the allowable range for light aggregate sand with a maximum size of 12.7 mm. Due to the

granulation, the consumed Leica is of coarse light grain type.

Internal reinforcement is ribbed and types AIII. The flow stress of size 20 and 8 rebars are equal to 4624 and 4930, respectively. In this research, 10 × 10 × 10 cm cubic samples have been used to determine the compressive strength. The cube shape of the molds, the size of the sides, and the smoothness of the surfaces inside the mold must conform to the recommended specifications [10]. After performing several initial mixing designs to prepare lightweight concrete with suitable structural strength for the desired beams, the mixing design of Table 1 has been used:

Table 1

Lightweight concrete mixing plan for one cubic meter of concrete

cement (kg)	Micro-silica (kg)	Super lubricant (kg)	Water (kg)	Sand (kg)	Leica (kg)	Percentage of water to cement	Size of Leica (mm)	Special Weight (kg/cm3)
475	47/5	7	199/5	803	268	0/42	5-10	1800

3.2. Structural design and how to test the beams

All beams are made with a length of 100 cm and cross-sectional dimensions of 20 × 20 cm. All beams have 6 rebars with a diameter of 20 mm and the joints are designed according to the Iranian concrete regulations. According to this regulation, we have:

$$V_s < 2V_C \rightarrow S_{max} = d/2$$

$$V_s > 2V_C \rightarrow S_{max} = d/4$$

Therefore, in the middle 1.3 of the beam, because the amount of cut is less, so the braces are considered with a distance of 8 cm, and at the two ends of the beam, the distance of the braces is equal to 4 cm. closed stirrup with a diameter of 8 mm is also used in the design. A schematic of the four-point bending test system and the details of the beams are presented in Figure 1. The specific weight of the resulting concrete is 1800 and the compressive strength of the cube sample is 245.7. Figure 2 also shows the modeling of longitudinal and transverse beams in ABAQUS software.

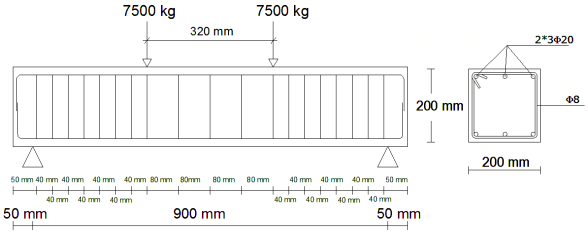

Fig. 1. Schematic of the test system and details of the beams

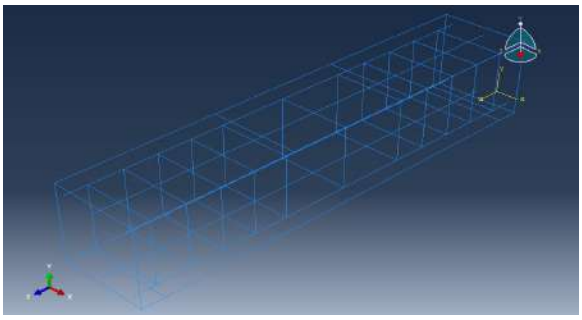

Fig. 2. Modeling of longitudinal and transverse beam reinforcements in ABAQUS

All beams were tested after 90 days from the date of concreting. To determine the path of cracks caused by the application of load, the surface of the beam was covered with white lime and after determining the exact location of the load (distances of one-third of the supports), the location of the displacement was marked. After placing the beam in the device, the load was applied to the upper beam by a jack with a capacity of 100 tons and entered the tested beam through it. In order to read the load (in terms of kg) and its related displacement, a load gauge and displacement meter were used, respectively, and for each amount of load applied by the hand jack, the relevant load and displacement were read and recorded.

3.3. Modeling using ABAQUS software

Since ABAQUS is a widely used general modeling tool, its use is not limited to mechanical analysis of solids and structures (stress-displacement). Using this software, various issues such as heat transfer, mass penetration, thermal analysis of electrical components, acoustics, soil mechanics and piezoelectric can be studied.

Using ABAQUS software, although it provides a very wide range of capabilities to the user, is a relatively simple task and by which the most complex issues can be easily modeled. For example, problems involving more than one component can be modeled by creating a geometric model of each component and then attributing the behavior of the material to each component and then assembling the various components. In most modeling, even models with high nonlinear degrees, the user has to determine only the engineering data such as the geometry of the problem, the behavior of the material concerned, the boundary conditions and the loading of the problem. In this dissertation, ABAQUS / CAE has been used for modeling.

In this paper, Dynamic Explicit analysis method is used. In this method, in the implicit solution method, a set of equations must be solved simultaneously and as a system of equations. Now for the problems that depend on time and we want to solve them by implicit method, the set of equations mentioned must be solved in any time development. As mentioned, in the explicit method, the dynamic equation (or the equation of motion) was applied at the beginning of each temporal evolution (at time t). Alone could be solved. But in the implicit method, which uses Newton's iterative method, the dynamic equation of equilibrium is written at the end of the temporal evolution (at time $t + \Delta t$). This causes the internal forces, in addition to acceleration, to join the set of unknowns, which makes it impossible to solve the equation of each node alone, and the equations must be written for all nodes and then solved simultaneously.

This method automatically selects the temporal development size. Of course, this value can also be selected by the user because the implicit solution method, unlike the explicit method, is convergent without any conditions. For this reason, the size of the development time in implicit solution is usually larger than the explicit solution method. For a nonlinear problem, the set of equations obtained in a time pattern is solved iteratively, and in each time pattern, several iterative steps are required to obtain an answer within the set tolerances.

4- Review and Compare the Results

In this section, the structural behavior of laboratory and modeled beams is investigated, the results of compressive strength and four-point bending tests (load diagram - displacement diagram) are explained, and then the results of finite element analysis using the model The samples are made in the software, and finally, a comparison is made between the laboratory results and the modeling.

In order to study the structural behavior of beams, five concrete beams including Leica light concrete with the amount and arrangement of rebars, cross-sectional dimensions, amount of cementitious materials, and the ratio of water to the same cementitious materials have been made, which are detailed in Section 3.

4.1. Compressive Strength and Specific Weight

The results of the compressive strength test of cube samples of 10 × 10 × 10 cm and their specific gravity are presented in Table 2.

Table 2

Compressive strength and specific dry weight of tested samples

Beam	f_{cu} (N/mm^2)	Dry specific gravity (kg/m^3)
B1	24/62	1795
B2	23	1790
B3	25/62	1798
B4	26	1801
B5	23/62	1792

4.2. Investigation of the Structural Behavior of Laboratory Beams

In this section, the flexural behavior of the beams is investigated. Table 3 presents the results of the four-point bending test of laboratory beams.

To investigate the displacement of the beams, the load-displacement curve is examined. These curves are shown in Figure 3. As can be seen in these figures, the curves of Leica lightweight concrete beams are linear up to 12500, 11600, 13100, 13200, 10400 kg, respectively, but then the slope of the

curve decreases, which indicates the flow of longitudinal rebars.

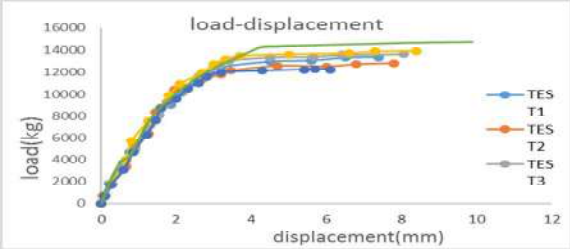

Fig. 3. Load-displacement curves for laboratory and modeled samples

According to the manual calculations, we know that the tensile steel has flowed while the steel that is in the compression zone has not yet flowed, and due to the flow of tensile steel, the cross-section failure is flexible. As can be seen in the above figures, after the steel starts to flow, many displacements occur without a significant increase in load, which indicates the good formability of Leica lightweight concrete.

Table 3

Recorded values from Leica lightweight concrete beam test

Beam 1		Beam 2		Beam 3		Beam 4		Beam 5	
load (p)	displacement	load (p)	displacement	load (p)	displacement	load (p)	displacement	load (p)	displacement
(kg)	(mm)	(kg)	(mm)	(kg)	(mm)	(kg)	(mm)	(kg)	(mm)
720	0/06	670	0/08	700	0/12	550	0/07	630	0/05
1800	0/2	1700	0/25	1750	0/3	1800	0/25	1695	0/25
3700	0/6	3050	0/6	3900	0/65	4000	0/65	3350	0/65
4700	0/75	4700	0/85	4550	0/9	5700	0/8	5150	0/9
7250	1/3	6250	1/2	7150	1/3	7500	1/25	6400	1/25
8500	1/55	7600	1/45	8100	1/55	8800	1/6	8350	1/45
9050	1/85	8750	1/6	9550	1/9	9900	1/8	9250	1/75
10100	2/15	9550	2	10350	2/25	10950	2/1	10400	1/95
11100	2/5	10550	2/3	11650	2/6	12000	2/7	11150	2/55
11550	2/8	11050	2/6	11800	2/8	12800	3	11400	2/7
11950	2/9	11600	2/8	12650	3/15	13200	3/3	11800	3/2
12500	3/2	12000	3/2	13100	3/4	13500	3/7	12150	3/45
13000	4/5	12150	4/3	13400	4/5	13650	5	12600	4/7
13100	5/6	12250	5/4	13450	5/65	13750	6/6	12550	6
13350	6/5	12300	5/7	13600	6/4	13900	7/3	12750	6/8
13400	7/4	12250	6/1	13680	8/05	13950	8/4	12850	7/8

The final rupture load of Leica lightweight concrete beams is 13400, 12250, 13680, 13950, and 12850 kg, respectively. Figure 4 shows laboratory tested RC beam and failure 5 shows the shape of arrow 3 (for example) before and after failure.

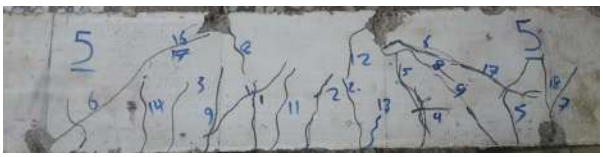

Fig. 4. Laboratory Tested RC beam failure

A. Before failure

B. After failure

Fig. 5. Laboratory beam before and after failure

Comparison of the final load of Leica lightweight concretes shows that although its specific gravity and compressive strength are lower than ordinary concrete, it has an acceptable final strength for use in a structural beam. The weight of concrete, Leica lightweight concrete beam with a specific weight of 1800 kg / m3 and compressive strength of 24.57 MPa is about 25% less than the weight of ordinary concrete, which by making the weight of concrete lighter, significant advantages can be achieved, including forces on The structure shrinks.

Failure of the specimens occurred by creating shear and flexural cracks and flexural shear in the tensile zone and crushing of concrete in the compressive zone.

4.3. Results of Modeled Beam Structural Behavior

In this research, the powerful ABAQUS finite element software has been used for modeling and static analysis on Leica lightweight concrete beam samples.

Figure 3 shows the load-displacement diagram of the modeled beam. Also, the displacement contour obtained for the beam modeled in finite element software is shown in Figure 5.

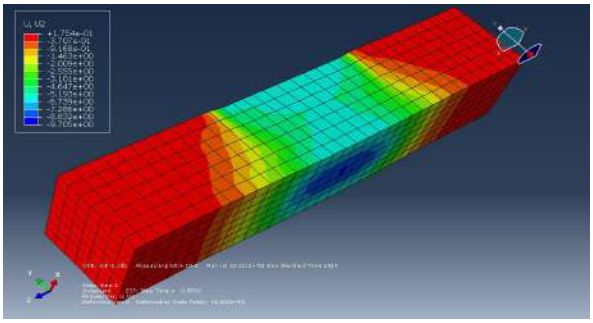

Fig. 6. Displacement contour in the direction of applying force

According to Figure 3, it can be seen that the modeling results are consistently consistent with the laboratory results.

Due to the shape of the above diagrams and the final strength and displacement of the samples, in laboratory samples and modeled samples, it is observed that there is an acceptable match between the results and the accuracy of the software output results can be ensured.

The relationships in the regulations are based on ordinary concrete, while the concrete used in this research is lightweight concrete, so the bearing capacity obtained based on the relationships with laboratory results is not necessarily the same.

There is a possibility of executive errors in the laboratory, so the accuracy of the results is less than the modeling result in ABAQUS software.

4.4. Investigation of Failure Mode of Laboratory and Modeled Beams

Figure 6 shows the main stress distribution in the modeled beam.

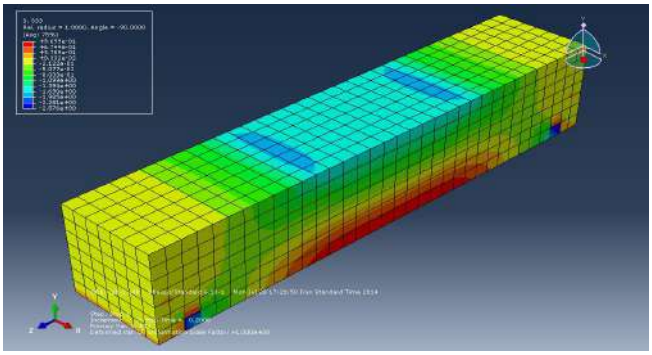

Fig. 7. The main stress contour of the modeled beam (N/mm^2)

As we know, cracking occurs in places where the stress has reached the cracking stress of concrete. Therefore, the distribution of von-mises stress and shear stress of beams is also shown in Figure 7.

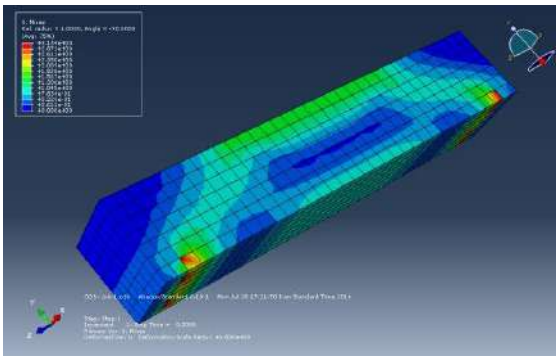

A.

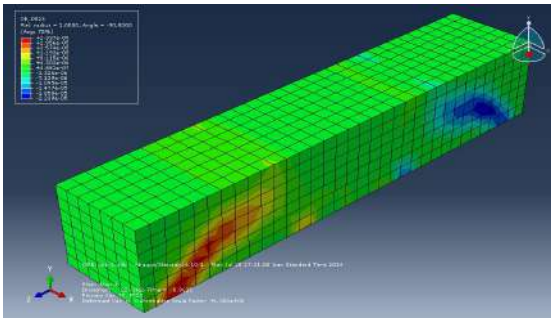

B.

Fig. 8. A. Tension contour B. Modeled beam shear stress contour (N/mm^2)

Comparing the laboratory results with the modeling results, we conclude that the crack shape corresponds to the stress distribution resulting from finite element analysis, and this is another testament to the accuracy of the modeling and the reliability of the model.

As can be seen in the figures above, shear cracks have occurred at the endpoints of the beam, in view of what has been said about shear cracks in the beams, and it should be noted that due to laboratory limitations it is possible to perform experiments on beams. There was no higher, such a result is not far from the mind.

As can be seen in the figures above, in places such as supports or loads, local rupture occurs due to the concentration of existing stress, which was not unexpected.

On the other hand, we know that at the moment of final beam failure, in places where the plastic strain has exceeded 0.0035, crushing occurs in concrete. For this purpose, Figure 8 shows the plastic strain distribution of concrete beams.

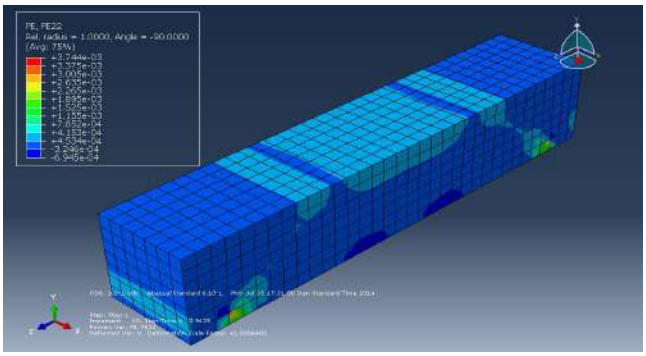

Fig. 9. Plastic strain contour

As can be seen in the figure, at the points where the beam is modeled, the strain is beyond the plastic strain of the concrete, crushing has occurred, which means at the point of support and the place of force application, as shown by the laboratory results in Figure 4. Shown, matches.

5- Result

According to the new approach of the construction industry, which seeks to reduce the dead load of the building and, consequently, reduce the seismic force on the structure, we are witnessing the rapid emergence and flourishing of the use of lightweight concrete in this industry. In this research, laboratory and analytical study of bending behavior of structural beams made of lightweight concrete have been investigated. For this purpose, five structural beams were examined in a laboratory, and finally, one beam was modeled using ABAQUS finite element software. The results of these studies are given below.

Load-displacement diagrams The middle of the span of all beams is drawn, which, regardless of the slight differences observed in the diagrams, can be said to be consistent with each other. The amount of load at which the tensile reinforcements start to flow is about 12/160 tons. The final load that the made beams can withstand is about 13.226 tons, in this case, the displacement of the middle of the span is about 7.55 mm. The ABAQUS finite element software model has acceptable compatibility with laboratory results. The crack distribution in the laboratory samples corresponds to the distribution of stresses obtained from the modeled beam, which is a testament to the accuracy of the modeling. Local failure has occurred at points of the beam that are under load and at the fulcrum, which can be seen in both laboratory and modeling results.

Comparing the results obtained in this study with the numerical results obtained by using the regulatory relations that are for ordinary concrete, we conclude that the bearing capacity of beams with light concrete is less than ordinary concrete, but according to The reduction of sample weight and the fact that this difference in capacity is negligible, the use of lightweight concrete in structural members such as beams or columns is recommended.

References:

[1] Kim HungMo, U. JohnsonAlengaram, Mohd ZaminJumaat. Bond properties of lightweight concrete – A review, Construction and Building Materials, Vol 112, 1 June 2016, Pages 478-496

[2] Karl-Christian Thienel, Timo Haller, Nancy Beuntner. Lightweight Concrete—From Basics to Innovations, 2020, Materials, Vol 13, Issue 5.

[3] Bagheri AS, Rahmani AS, Ruh Shahbaz J. 2001, Laboratory study of engineering properties of lightweight concrete made with natural lightweight aggregate (Pumice), the first international conference on concrete and development.

[4] Yazdi J. "Lightweight concrete and its application in the construction industry", Tabriz Lightweight Insulation Industrial and Mining Company.

[5] Mayasserm. Jomaa'h, Hosam A. Daham, Saad M. Rao' of, Flexural behavior of lightweight concrete beams, European Journal of Scientific Research, 20 II Vol. 58 No. 4, PP. 582-592.

[6] Delsye C.L. Teo, Md. Abdul Mannan and Johan V. Kurian. Flexural behavior of Rein Forced Lightweight Concrete beams made with oil palm shell (OPS), Journal of Advanced Concrete Technology, 2006, Vol. 4, No. 3, PP. 1-10.

[7] Chung- Hao Wu, Yu- Cheng Kan, Chung – Ho Haung, Tsong Yen and Li- Huai Chen. Flexural behavior and Size effect of full Scale Reinforced Light Weight Concrete beam. 2011, Journal of Marine Science and Technology, Vol. 19, No.2, PP. 132-140.

[8] Meh met Kamanli, M. Yassar Kaltakci, Fatih Bahadir. Fatich S.balik, H Hasnu Korkmaz, M Sami Don Duren and M. Tolga Cogurcu, Predicting The Flexural behavior of reinforced Concrete and lightweight Concrete beams by ANN, Indian Journal of engineering & materials Since, 2012, Vol. 19, PP. 87-94.

[9] Tao Wu, Hui Wei, Xi Liu. Experimental investigation of shear models for lightweight aggregate concrete deep beams, Advances in Structural Engineering, 2017.

[10] BSEN. 12390-3: 2009- Testing hardened Concrete Compressive Strength of Test Specimens.

Journal of Civil Engineering Researchers

J-Researchers

JOURNAL OF CIVIL ENGINEERING RESEARCHERS

Evaluation of Modified Seismic Model Using Shear Keys at Steel Beam Connections to Concrete Colum

Lobat Hosseinzadeh[a*]

[a]*PHD Student of civil engineering,Islamic Azad University,Chaloos Branch,Iran*

Article History: Received date 2022.02.05; revised date : 2022.03.10; accepted 2022.05.24

Abstract

Reinforced concrete columns to steel beam connections are recently considered as structural system. This system takes the advantages of both through optimally combining metal and concrete structural elements. There are two connections through beam and through column connections. This study first reviewed the literature; then, the authors modeled a sample connection experimentally carried out in a laboratory by Cheng Chih and Cheng Tung Chen in 2005 by ABAQUS finite element software and investigated seismic performance of RCS connections under back/forward and monotonic loadings. Once the finite element model was validated, a parametric study (studying web steel panel thickness at the joint, studying coating thickness, etc.) was conducted; and finally, a modified model was proposed following connection results were compared showing a more stable and desired behavior in addition to the increased capacity of the connections. The result showed that the use of a through-plate with shear keys in the joint zone will increase the strength of the joint and the formation of a plastic joint outside the joint and will greatly improve the joint behavior. So that the contribution of concrete in the shear capacity of this area has increased, which was 73% for the modified model of Cheng and Chen. Also the use of a through-plate for RCS joints converts the forces transmitted from the beam to in-plane stresses and by shear keys, through two shear and support mechanisms, these forces are transferred to the concrete of the joint area and in consequence, these stresses are transferred to the concrete column.

Key terms: Steel beam connection to concrete column, Finite element method (FEM), RCS

1. Introduction

Numerical modeling is a widely economical time-saving applied technique to solve complex problems [1, 2]. In recent years, RCS systems, as one of the new building systems consisting of the

reinforced concrete columns and steel beams, have been widely considered in the design and construction of buildings in the United States and Japan [3]. In Japan large construction companies have developed their facilities and invested in research on RCS systems. As a result, a large number of beam-to-column details have been proposed to implement this system so far [4-6]. These systems are typically based on standards published by the Japan Institute of Architecture [7] and the Japan Building Center (BCJ). 1994) However, most of the new details of these connections are not covered by the standards. Developing basic design methods for RCS systems and connections is an urgent need in Japan. The study of the interconnection of RCS systems included the study of "composite and hybrid structures" as part of a joint US-Japanese seismic research program that began in April 1993 as a five-year research program [8]. Numerous experimental studies have been performed to study the performance of RCS. Sheikh, Deierlein, Yura and Jirsa [9] tested RCS internal connections on a scale of 3.2 at the University of Texas. RCS connections have also been tested by KANNNO [10] at Cornell University. Kim and Noguchi [11] studied the shear strength of RCS joints in detail through finite element analysis. To estimate the shear strength of RCS internal and external joints, experimental research including 9 RCS external joints was performed at the University of Michigan [12, 13].

Cheng and Chen [14] tested six RCS connections by considering different parameters such as Connection stirrups, beam cross-section effects and loading protocol. All research on this type of composite structure up to 2011 was reviewed by Li, Li, Jiang and Jiang [15]. Noguchi and Uchida [16] investigated two RCS frames focusing on connection failure and investigating connection mechanism states through nonlinear FEM analysis. Li, Li and Jiang [17] proposed a model and conducted a parametric study to investigate the behavior of composite concrete columns by continuous compound spiral ties and enclosed steel beams. Alizadeh, Attari and Kazemi [18] tested two new cases of RCS internal connections based on the strong column weak-beam (SCWB) criterion to study the performance of new details for RCS connections.

Xu, Fan, Lu and Li [19] proposed a new type of pre-pressed spring self-centering energy dissipation system (PS-SCED) that combines friction mechanisms between internal and external pipe components for energy supply. Cao, Feng and Wu [20] studied the seismic performance of reinforced concrete frames (RC) reinforced by steel bracing, which considers the effect of filler walls. Since the implementation of RCS connections of the through-beam is stronger than the connections of the through-column, therefore, in this research, a model will be investigated that in addition to ease of implementation, the resistance of the connection is not less than the connections of the beam type.

2. the Experiment conducted by Cheng Chih Chen and Chin Tun Chen

In this study, the seismic behavior of steel beam to the concrete slab and non-slab column connection was evaluated in National Center for Research on Earthquake Engineering (NCREE), Taiwan. A total of six cross-shaped connections were made and evaluated. All experimental samples were the same size with steel beams of H596×199×10×15 and a 65×65cm concrete column. According to load combining, beam sizes of the roof to the first floor were H596×199×10×15,H396×199×7×11,and,H500×200×10×16,respectively (samples of all tests were for the first floor). The concrete column was reinforced by 12 longitudinal rebar in #11.

Figure 1 represents the experiment. Prior to the experiment, a hydraulic jack imposes a fixed 1000 kN axial load over the column indicating the gravity load obtained by frame analysis. Then, the hydraulic drivers, at both beam ends, impose a cyclic load, as shown in Figure 2, through a triangular applied displacement. During the experiment, a horizontal driver at the top of the column keeps the column in the current state and only allows for in-plate rotation.

[3]

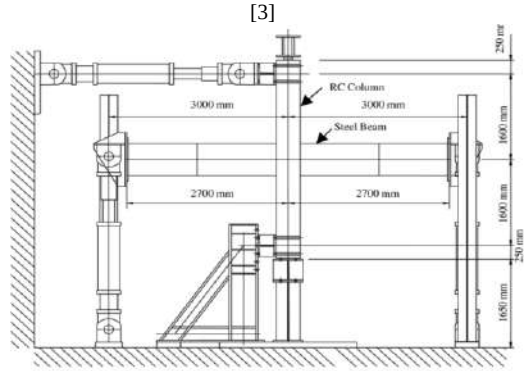

Figure 1: Schematic of experimental set up [3]

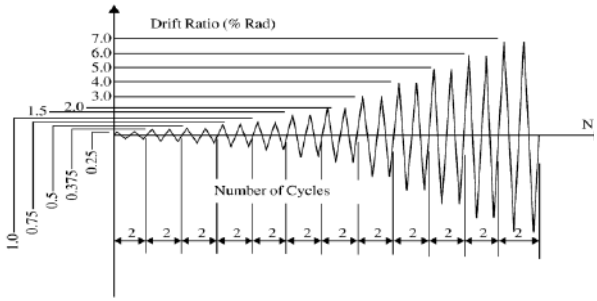

Figure 2: backward/forward displacement graph on beam ends

3. Finite element modeling through ABAQUS

ABAQUS was produced by ABAQUS Company, of active finite element software firms, in 1987. In the implicit nonlinear static analysis, the software applied two Static General and Static Rik's procedure analysis methods. This research used the nonlinear static general analysis method by Newton-Raphson convergence algorithm.

The initial development value for analysis is 0.001, the minimum development value is equal to a small value of 10-10 × 1, the maximum number of samples per step is 10,000 and the selection of samples is selected automatically.

3.1 Concrete compressive stress-strain curve

This graph is determined based on concrete uniaxial compressive test results. Three areas of the graph are introduced for under pressure concrete. The first part is assumed elastic to the load and resistance factor (LRF) stress, which is [4], where is the concrete compressive strength. strain associated to the stress is 0.0022. Young's modulus is also calculated by [4] and the Poisson ratio is 0.2. The second part, which is parabolic starts from LRF stress point up to reaching the highest concrete compressive strength, . It is obtained as follows:

$$\sigma_c = \left(\frac{kn - n^2}{1 + (k-2)n} \right) f_{ck} \quad (1)$$

Where,

$$\varepsilon_{c1} = 0.0022 \qquad k = 1.1 E_{cm} \times \frac{\varepsilon_{c1}}{f_{ck}} \qquad n = \frac{\varepsilon_c}{\varepsilon_{c1}} \quad (2)$$

Where, E_{cm} is the concrete elasticity modulus.

The third part of stress-strain curve is the descending graph from f_c to rf_c, where r is 0.85. Concrete ultimate strain (ε_{cu}) in stress failure rf_c equals 0.01.

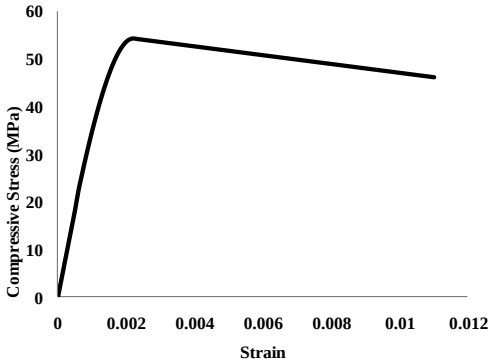

Figure 4: Concrete strain-stress curve at the compressive strength of f'_c =54Mpa

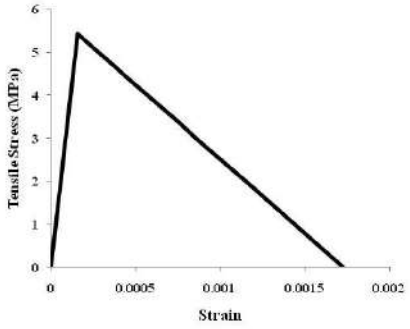

Figure 3: Concrete tensile stress-strain curve at compressive strength f'_c =54Mpa

3.2Steel materials

The two-line Elasto-plastic model is used for steel beams and rebar. Further, a similar behavior was also assumed for both strain and stress .

4. Boundary conditions

Concrete column, in the laboratory tests, belongs to the first floor jointed to foundation by a clamped connection. Therefore, in modeling, all translational and rotational column degrees of freedom U_1, U_2 , U_3 , UR_1 , UR_2 , UR_3 connected to the rigid plate anchor are also closed. Indeed, this boundary condition is applied to the rigid plate reference point influenced other nodes. In the laboratory test, a hydraulic driver keeps the column current status prior to testing such that it is only allowed in-plate rotation. In software, only UR2 degree of freedom is open to simulate upstream column boundary conditions. The beams, at both ends, may move upward and downward rotating in-plate. In the finite element model, at beam ends, only U3 and UR_2 degrees of freedom are open; while, U_1, U_2 , UR_1 , and UR_3 are close.

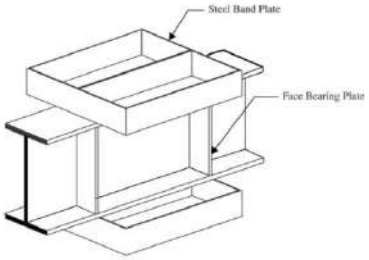

Figure 5: Steel connection including the beam and trace sheets [3]

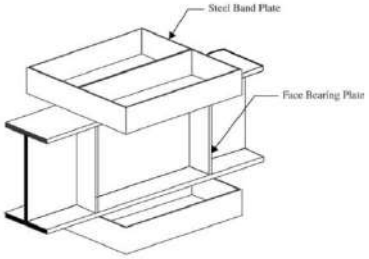

Figure 5: Steel connection including the beam and trace sheets [3]

5. Size and types of elements

The concrete column was modeled by 3D C3D8R elements accessed in ABAQUS library, which are, in fact, 8-point elements used for non-linear analyses including contacting two bodies, large deformations, plasticity, and failure. Steel beams and other connected components were also meshed by the elements. Rebar and anchor rigid plates were also modeled by T3D2 and R3D4 truss elements, respectively. In addition, to decrease analysis time, larger elements were mostly used and smaller elements were used in connection zones. Elements, in most beam and column zones, were 35 mm; while, the smallest was 18 mm.

6. Results of finite element analysis and INUC experimental results

As seen in Figure 7, numerical and experimental results were consistent in drifts smaller than 4% showing consistently similar behavior. They experience the maximum resistance at drift 4%; whereas, at higher drifts, the resistance may not

drop and is constantly up to the drift of 7% as the steel behavioral model was elasto-plastic in the finite element model with no failure. However, in the laboratory model, the resistance is dropped at higher cycles, once the resistance reaches the maximum of 4%.

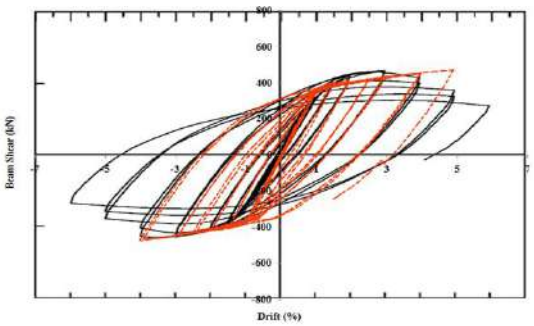

Figure 7: Comparison of beam shear graph to beam end displacement in FE and laboratory models

6.1 Main stress distribution of minimum connection

Connection shear resistance is measured based on concrete connection effective width, which is total width of inner and outer panel. Inner zone concrete is activated against the bruise of anchor plates and beam wings. Concrete presence outside beam wings range depends on activation of horizontal pressure pickets formed by double sheets bruising and or steel column on the concrete up and down the connection. Pressure shaft at the compressive picket end is dealt with beam up and down horizontal controls. Up and down beam controllers are required to deal with beam horizontal and perpendicular tensile forces. Beam perpendicular forces are balanced and beam parallel forces are transferred to the outer compression zone. This section tried to represent the mechanisms formed in concrete inner and outer connection of finite element results. Figure 8 clearly shows how these mechanisms are formed.

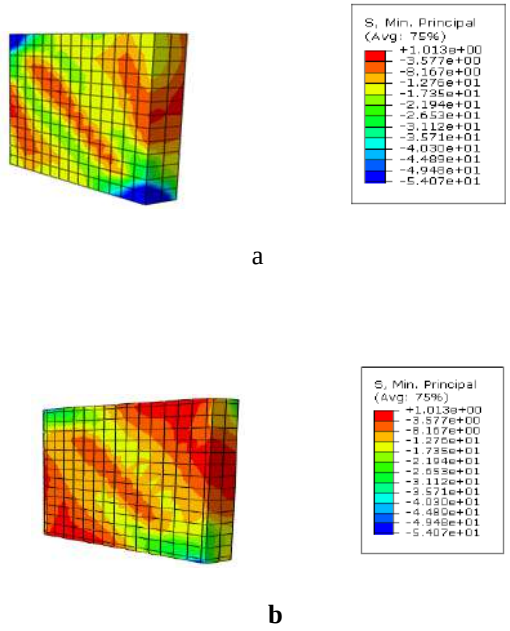

Figure 8: Diagonal compressive pickets in a. inner concrete panel, b. outer concrete panel

7. Modified model

In this model, Cheng and Chen's model is modified such that beam wings are removed at connection zone; and the middle plate extends out the connection by adding cross-beam effect; the beam is connected to the connection by welding beam web and wing to the middle plate, as seen in Figure 15. Moreover, the middle plate is designed such that middle plate cross-section is larger than beam plastic cross-section (Z_p); and consequently, the plastic joint is transferred out the connection. Hence, middle plate thickness is 20 mm. In addition, beam effect perpendicular to beam main axis is regarded considering perpendicular steel panel. Thus, connection zone is turned into four springs, where five rows of L-shaped plates were used (see Figure 9b). Furthermore, the stirrups of joint zone is removed and SCP plates of 15 mm thickness are used instead of SBP.

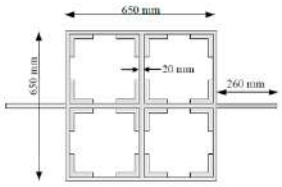

a. Connection steel characterization

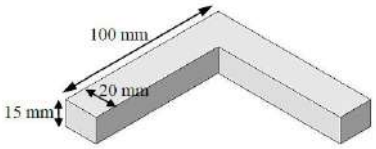

b. Specification of shear keys

7.1 Evaluation of the proposed bonding strength comparing Cheng and Chen model

Comparing the results of Cheng and Chen and the proposed modified model revealed that shear responses are larger than the proposed model drift in terms of hardness and strength. Finite element model responses for Cheng and Chen and the proposed model by middle plate and shear keys under unilateral uniform loading are shown in Figure 10.

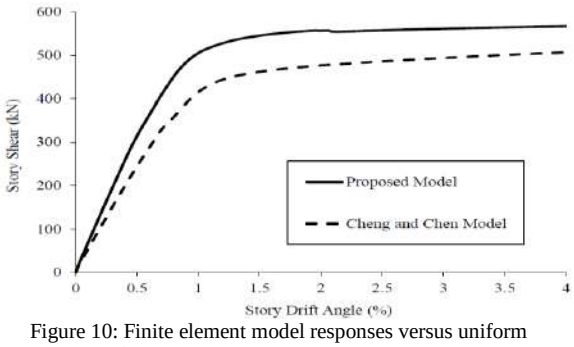

Figure 10: Finite element model responses versus uniform loading for Cheng and Chen and the proposed models

7.2 Stress distribution in a middle plate and shear keys

As Cheng and Chen considered drift of 1.4%, the modified model used this drift to study the mechanisms, too. At drift 1.4%, web steel plate approaches the yield tension from the middle zone; by drift gradual increase, most zones reaches to the yield tension. Since the joint zone is properly reinforced, steel beam web tensions reach the yield threshold at the middle connection zone; however, plastic joint is not formed in the connection. Figure 11 represents path tension distribution contours in steel beam web at drift 1.4%.

7.3Tension distribution in concrete junction

As seen in Figure 18, concrete junction is activated versus bruising of shear keys and SCP plates. Activation of concrete junction depends on two friction factors between steel and concrete considered by shear keys. In general, the friction coefficient is increased leading to better simulation and compressive picket at concrete junction. SCP is the second factor, which helps in forming concrete picket at the junction and better circulation of the forces. This section tried to show concrete junction mechanisms of the finite element model. Figure 12 illustrates how this mechanism is formed.

7.4 Studying plastic joint mechanism

As previously mentioned, new connection is designed such that the plastic joint is formed inside and no inside connection reaches up to the yielding threshold. This is a desired mechanism as structure repair and rehabilitation are enabled following beam plasticization. While, if it occurs inside the connection, it would be impossible to repair and rehabilitate the structure. The proposed model analysis showed that plastic strains are formed inside beam elements clearly indicating plastic joints in the beams. However, wing buckling, as seen in Figure 13, occurs at the compressive wing.

7.5 Cracking in concrete column

In this model, as displacement is applied to the beam ends, like Cheng and Chen model, and regarding that the column is only allowed to in-plate rotation (one clamped end), the rotation is small which causes little damage to the column and few cracks at concrete column junction. In addition, transverse cracks occur just above and below steel

beam. Figure 14 shows cracking finite element analysis results, which are few.

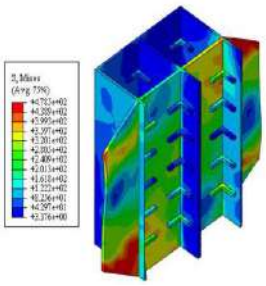

Figure 11: Mises tension distribution contours in the middle plate and shear keys at drift 1.4%

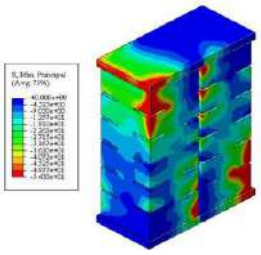

Figure 12: Minimum main tension distribution contour at concrete junction

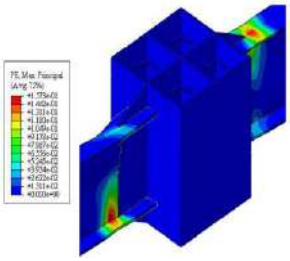

Figure 13: Plastic strain distribution contour at steel zone

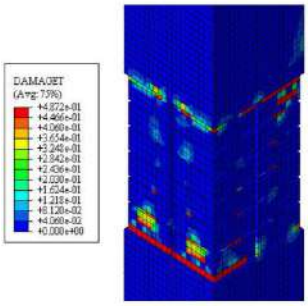

Figure 14: Concrete cracking distribution contour

7.6 Various force elements at junction

Therefore, according to Table 1, junction shearing contribution of various elements is obtained by finite element analysis results through ABAQUS at drift 1.4% is:

Table 1: Share of various force elements at junction at drift 1.4%

Middle plate panel	231 KN
Concrete junction contribution	655 KN
Junction shear capacity	889 KN
The force created in the concrete picket	1976 KN

8. Conclusion

1. Beam and column set is transformed by four components including beam bending, column bending, joint crushing, and connection panel shearing.

2. Connection is divided into three shear resistance components: steel web panel, internal concrete panel, and external concrete panel. All these components are activated against shear force. Steel panel firstly yields; next, shear capacity of web steel panel slowly increases. And then, indoor and outdoor concrete panels resist against shear force.

3. Applying middle plate with shear keys at junction causes increased connection resistance and plastic joint outside connection and largely improves connection behavior. Therefore, junction concrete contribution in shear capacity increases at this zone, which is 90% for Nishiyama and Kuramoto model and 73% for Cheng and Chin.

4. Middle plate for RCS connections turn to beam transferred forces into in-plate tension; then, the forces are transferred to concrete junction through shear and anchor mechanisms by shear keys. However, the tensions are consequently transferred to the concrete column.

References

[1] H.H. Asli, M. Arabani, Analysis of Strain and Failure of Asphalt Pavement, Computational Research Progress in Applied Science & Engineering 08(01) (2022).

[2] M. Feizbahr, C. Kok Keong, F. Rostami, M. Shahrokhi, Wave energy dissipation using perforated and non perforated piles, International Journal of Engineering 31(2) (2018) 212-219.

[3] A. Joorabchian, Z. Li, K.D. Peterman, Experimental and numerical investigation of fixed-height cold-formed steel wall assemblies bearing on concrete slabs, Thin-Walled Structures 166 (2021) 107940.

[4] A.I.o.J. (AIJ), Proc., Symp. on Mechanical Behavior of Beam to Column Connections for Composite RCS Systems, Tokyo, Japan, 1994.

[5] S. Ghods, A. Kheyroddin, M. Nazeryan, S.M. Mirtaheri, M. Gholhaki, Nonlinear behavior of connections in RCS frames with bracing and steel plate shear wall, Steel and Composite Structures 22(4) (2016) 915-935.

[6] S.M. Mirtaheri, M. Nazeryan, M.K. Bahrani, A. Nooralizadeh, L. Montazerian, M. Naserifard, Local and global buckling condition of all-steel buckling restrained braces, Steel Compos. Struct 23(2) (2017) 217-228.

[7] A. AIJ, Standards for Structural Calculation of Steel Reinforced Concrete Structures, Architectural Institute of Japan (2001).

[8] H. Yamanouchi, 'US–Japan cooperative structural research project on composite and hybrid structure. Part 1: Overall research program, Summaries, Technical Papers of Annual Meeting, Architectural Inst., Jpn, 1994, pp. 1521-1522.

[9] T.M. Sheikh, G.G. Deierlein, J.A. Yura, J.O. Jirsa, Beam-column moment connections for composite frames: Part 1, Journal of Structural Engineering 115(11) (1989) 2858-2876.

[10] R. KANNNO, Strength, deformation, and seismic resistance of joints between steel beams and reinforced concrete columns, Doctor Dissertation presented to the Faculty of Graduate School of Cornell University (1993).

[11] K. Kim, H. Noguchi, A study on the ultimate shear strength of connections with RC columns and steel beams, J. Struct. Construct. Eng 507 (1998) 163-169.

[12] G. Parra-Montesinos, J.K. Wight, Seismic response of exterior RC column-to-steel beam connections, Journal of structural engineering 126(10) (2000) 1113-1121.

[13] G. Parra-Montesinos, J.K. Wight, Modeling shear behavior of hybrid RCS beam-column connections, Journal of Structural Engineering 127(1) (2001) 3-11.

[14] C.-T. Cheng, C.-C. Chen, Seismic behavior of steel beam and reinforced concrete column connections, Journal of constructional steel research 61(5) (2005) 587-606.

[15] W. Li, Q.-n. Li, W.-s. Jiang, L. Jiang, Seismic performance of composite reinforced concrete and steel moment frame structures–state-of-the-art, Composites Part B: Engineering 42(2) (2011) 190-206.

[16] H. Noguchi, K. Uchida, Finite element method analysis of hybrid structural frames with reinforced concrete columns and steel beams, Journal of structural engineering 130(2) (2004) 328-335.

[17] W. Li, Q.-n. Li, W.-s. Jiang, Parameter study on composite frames consisting of steel beams and reinforced concrete columns, Journal of Constructional Steel Research 77 (2012) 145-162.

[18] S. Alizadeh, N.K. Attari, M. Kazemi, The seismic performance of new detailing for RCS connections, Journal of constructional steel research 91 (2013) 76-88.

[19] L.-H. Xu, X. Fan, D. Lu, Z.-X. Li, Hysteretic behavior studies of self-centering energy dissipation bracing system, Steel and Composite Structures 20(6) (2016) 1205-1219.

[20] P. Cao, N. Feng, K. Wu, Experimental study on infilled frames strengthened by profiled steel sheet bracing, Steel and Composite Structures 17(6) (2014) 777-790.

J-Researchers

JOURNAL OF CIVIL ENGINEERING RESEARCHERS

Evaluation of High Capacity Helical Piles in Silty-Clay Soil

Farhad Nabizadeh [a,*]

[a]*Department of Civil Engineering, Islamic Azad University of Chalous, Iran*

Article History: Received date: 28 December 2021; revised date: 30 January 2022; accepted date: 26 February 2022

Abstract

Helical piles have been extensively used as a deep foundation system for small to large load ranges and are thus suitable for various applications. Therefore, a concern over qualifying and quantifying their axial bearing capacities and performance characteristics seems to be warranted. This paper discusses design considerations, installation procedures, and results of full-scale field load tests. In this study, axial static loading tests on single, double, and triple helix helical piles under grouted and un-grouted conditions have been conducted. The field study has been performed on silty-clay soil, to investigate the behavior of helical piles. Also, the results of the piles load tests were interpreted using six methods presented in literature to predict the ultimate load capacity (Qu) for each pile. Results showed that in the silty-clay soil, grouted and un-grouted helical piles had a similar performance while grouted piles showed greater axial compressive strength. According to various limit load methods evaluation, it was concluded that the values for two methods of Chin, Decourt were close to the site values.

Keyword: Capacity, Helical piles, Field Study, Post Grouting

1. Introduction

Helical piles are used in the construction of structures such as buried pipelines, telecommunication and transmission towers, machine foundations, as well as commercial and residential buildings which might be exposed to uplift forces [1,2]. Among their construction and performance advantages over the conventional concrete and steel piles, one can mention their light weight, high compressive and uplift capacities, short installation time with minimal noise and vibration levels, suitability for construction in limited access conditions, installation in frozen or swampy soil conditions, cost-effectiveness, and provision of overturning and uplift stability immediately after installation due to the elimination of the curing that is encountered in concrete anchors [3].

Another advantage of helical piles, which makes them ideal for urban areas, is that they do not cause loud noises during installation process.

The helical piles' axial capacities can be assessed analytically via either the individual bearing or cylindrical shear methods. The assumption of the individual bearing method is that bearing failure happens at each individual helix. The assumption of

* Corresponding author. Tel.: +989113914437; e-mail: f_nabizadeh2002@yahoo.com.

the cylindrical shear method is the formation of a cylindrical shear failure surface which connects the uppermost and lowermost helixes. The axial capacity of this cylindrical shear failure surface is the sum of shear resistance along the cylindrical surface, bearing resistance above the top helix (for uplift loading) and beating resistance below the bottom helix (for compression loading), as well as adhesion along the top portion of the steel shaft above the helix level.

Byrne et al. indicated the possibility of using large diameter helical piles for offshore wind turbines, for which there are many advantages [4]. Abdelghany et al. reported a significant increase in anchor shaft's resistance to buckling and additional corrosion protection for the grouted column [5].

In this study, the behavior of helical piles in silty clay was investigated through a field study on the piles with different numbers of helixes. Also, the effect of post-grouting on the strength of these piles was assessed. The specific objectives of this study were: (1) to estimate axial compressive and tensile capacities, (2) to assess grouting effect on helical piles, (3) to compare axial compressive capacities of the helical piles. In order to achieve these objectives, six full-scale load tests were conducted including axial compressive tests. A report of the testing program is presented in the next sections.

2. Testing Procedure

2.1. Geotechnical Condition

The pile test was performed in a site in the city of Sari located in the north of Iran. The geotechnical study was conducted in the site and standard penetration (SPT) and cone penetration (CPT) tests were carried out. Soil stratigraphy in the test site consisted of silty-clay layers with middle layers of sand extended to the depth of 30 m, underlain by stiff layers of silt and clay extended to the depth of 40 m. A rock layer ranging from sandstone to soft siltstone was encountered at the depths of greater than 40 m. Ground water level was 0.5 m below the existing ground surface. The soil properties are summarized in Table 1.

Based on the test results, which were for the piles up to 28 m deep, the N-value derived from SPT was 20 and it reached 30 at deeper parts. Also, CPT results showed that at the depth of greater than 20 m, cone penetration resistance was about 5884 kPa and cone friction resistance ranged from 196 to 392 kPa.

2.2. Pile Installation and Test Set-up

Field behavior of the helical piles was studied by assessing the piles with one, two, and three helixes and the length of 6m. Also, the effect of post-grouting on the behavior of the piles was evaluated using the piles with the shaft diameter of 117 mm and helix diameter of 250 mm. The configurations for different piles considered for the helical pile load test program are summarized in Table 2. The configurations of typical test helical piles and double helix pile used in this study are shown in Figures 1&2.

The helical pile shaft was turned into the ground by torsion using a truck mounted auger or hydraulic torque motor attached to a hydraulic machine. A photograph showing installation equipment is shown in Figure 3.

Installation begins by attaching the helical pile lead section to the torque motor using a drive tool and drive pin. The lead section should be positioned and aligned at the desired location and inclination. Next, axial force should be applied to push the pilot point into the ground and the plumpness and alignment of the torque motor should be checked before rotation begins. Then, the pile should be advanced to the soil in a smooth and continuous manner at a rate of rotation typically less than 30 rpm. Installation torque and depth should be recorded at the selected intervals. Constant axial force should be applied while rotating helical piles to the ground. Helical piles are generally advanced until the termination criteria are satisfied. Termination criteria for helical piles involve achieving the required final installation torque and obtaining the minimum depth [6].

Table 1: Summary of soil properties

Depth(m)	Soil description	SPT N-value	Total unit weight (kN/m^3)	Undrained shear strength ($_{kPa}$)	Frictional resistance angle (°)
0-10	Silty clay layers with middle layers of sand	22	14.2-15.2	12-20	18~20
10-20	Silty clay layers with middle layers of sand	24	14.7-15.7	15-20	18~20
20-30	Silty clay	17	15.7-16.7	20-30	15~17
30-40	Silty clay	30	16.2-17.2	25-35	15~17
> 40	Silty clay	> 50	16.7-17.7	40-60	16~20

Table 2: Summary of pile configurations

	No. of helices	Shaft diameter, (mm)	Helix diameter(mm)	Helix thickness(mm)	Prototype anchor depth (m)
Pile	1	117	250	6	6
Pile	2	117	250	6	6
Pile	3	117	250	6	6

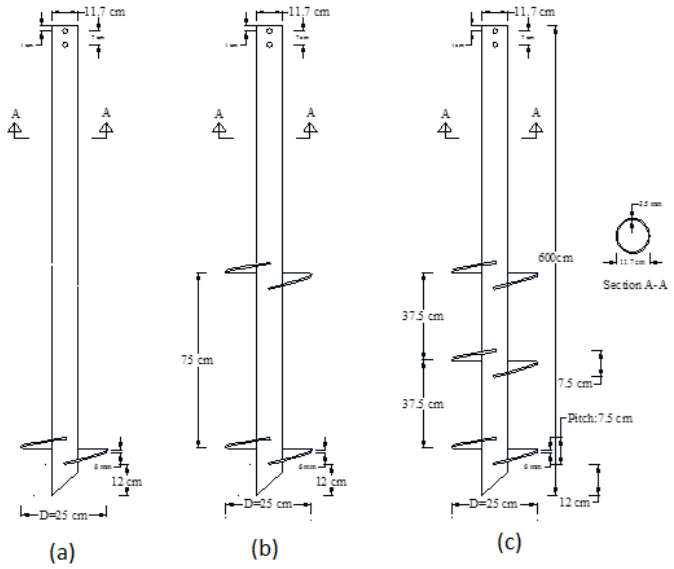

Figure1: Typical test helical piles configurations, a) single helix pile; b) double helix pile; c) triple helix pile

Figure2: The piles used in this study

Figure 3: Helical pile installation equipment

The axial compression load tests were carried out in accordance with ASTM standards D 1143-07. Since the main objective of the load tests was to determine the ultimate bearing capacity of the pile, Procedure A (Quick Test) was adopted for all the tests wherein numerous small load increments were applied and maintained constant over short time intervals [7].

The following specific test procedures using Procedure A for Quick Tests for the piles under axial compressive or uplift loads were applied:

1. Apply test loads in the increments equal to 5% of the anticipated failure loads and maintain load constant for 5 min. Monitor movements using LDTs at the intervals of 30 sec.

2. Add load increments until reaching a failure load, but do not exceed the safe structural capacity of the pile or reaction apparatus.

3. Unload the test pile in five increments and hold for 5 min with the same monitoring intervals as for loading. A photograph showing axial compression load test is shown in Figure 4(a,b&c).

(a)

(b)

(c)

Figure 4: Test Set-up(a,b,c)

2.3. Post-grouting Operation

The primary purpose of grouting is to compact the soil under and around the pile point. In the grouting procedure, cement grout is placed around the shaft to fill the annulus created by the anchor connection couplings while being screwed into the soil to make the shaft connecting the anchors stiffer [8]. Grout is the most important component in grouted helical piles.

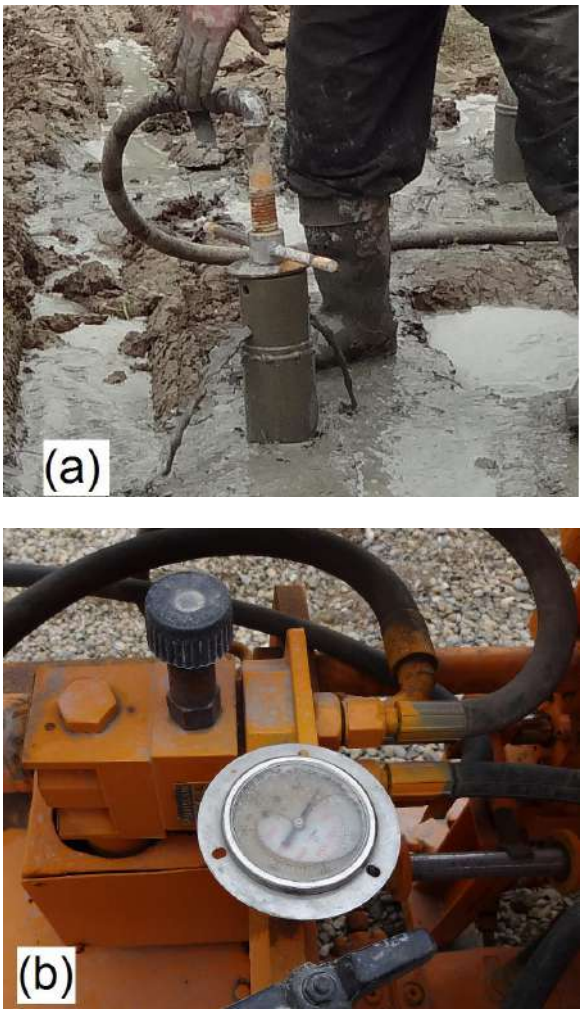

Figure5: a) Helical piles grouting operation b) Grouting pump

The ideal grout has a fine aggregate, such as silica fume (5-20% by weight), to increase the density and flow ability of the grout, is liquid enough to flow down around the pile shaft, and should bond to the anchor shaft so that skin friction capacity can be achieved.

In order to perform grouting, holes were made on the pile body. With plugging the top of the pile using the packer and creating some holes on the pile body from top to tip, grouting was made throughout the pile body. Using several separate grout flow paths provided a system that did not stop grouting operation. Grout is usually a mixture of water and cement with the water-to-cement ratio (W/C) of 0.4 to 0.55. Portland cement type II was thoroughly mixed with water in a colloidal mixer. The grout was compressed using a simple pump. In a condition that the pile provides an adequate reaction for the frictional resistance, pressure at the top of the pile can be achieved at 311 psi. A typical view of grouting operation is shown in Figure 5.

3. Review of methods of interpretation of the load test results

The methods of interpretation of the load test results depend on the limit or ultimate load which can be predicted by mathematical or graphical techniques. So determining the limit or ultimate load as accurate as possible is very important. There are six methods that can be used to predict the pile capacity from load-movement records of static loading tests. A summary of these methods is presented in this section.

3.1. Davisson's Method

Davisson's Offset Limit Method (ultimate load) offers the benefit of allowing the engineer, when proofing a pile for a certain allowable load, to determine in advance the maximum allowable movement for this load with consideration to the length and size of the pile. The pile load settlement curve is plotted to a convenient scale, so that the line represents the relationship between the load and shortening of an elastic free axially loaded column, Δ makes an angle of about 20 degrees with the load axis. It can be calculated from following equation:

$$\Delta = Q L / A E \quad (1)$$

Where, Q is the applied load, L is the length of the pile, A is the cross section area of the pile, and E is the modulus of elasticity of pile material. The offset limit load straight line is plotted parallel to the elastic line to intersect the load movement curve. Where OC is given by:

$$OC = 3.8 + D / 120 \quad (2)$$

Where, D is the pile diameter in mm. The load movement curve intersects the line at point C, the ordinate of which is 0.9 Qu according to the ECDF. This method provides a failure load value that tends to be conservative without dividing by the factor of 0.9 according to the ECDF that reduces the conservatism of the method. A primary advantage of this method is that the actual limit line can be drawn on the load movement diagram already before starting the test. The offset limit load criterion is primarily intended for interpretation of quick testing methods, but it can also be used when interpreting results from the slow methods. It is not suitable for testing methods that involve loading and unloading cycles. The Davisson Offset Limit is very sensitive to errors in the measurements of load and movement and requires well-maintained equipment and accurate measurements. However, it is easy to apply and has gained wide acceptance. The disadvantage of the offset limit load lies in the difficulty of determining the modulus of elasticity E for concrete piles and concreted pipe piles.

3.2. Chin-Kondner and Modified

Chin Methods Chin assumes that the relationship between load and settlement is hyperbolic. In this method each settlement value is divided by its corresponding load value. These are plotted against the settlement. The plotted values lie on a straight line approximately. The inverse slope of the straight line indicates Chin–Kondener Extrapolation Limits. This method was used to determine the loadmovement curve for which the Chin-Kondner plot is a straight line throughout. The calculated curve is shown in Figure 4 and it is given by the following equation:

$$S/Q = C1\ S + C\ 2 \quad (6)$$

Where: S = settlement of pile at pile load Q; C1, and C2 = slope and Y-axis intercept of the straight line, respectively. The Chin-Kondner limit load is of interest when judging the results of static loading tests, particularly in conjunction with the values determined according to Davisson's and Hansen's methods. Chin's method is affected by the limit of loading, as the pile is loaded near failure the greater predicted value of ultimate load, if the last two readings are omitted the resulting ultimate load value will be reduce by about 4%. Note that some analysts use the Chin-Kondner Extrapolation Limit as the pile capacity, after applying a suitably large factor of safety, this approach is not advisable. One should not extrapolate the results when determining the allowable load by dividing the extrapolated capacity by a factor of safety. Therefore, the ECDF, Part 4, 1991 reduces the resulting Chin-Kondner Extrapolation ultimate load by dividing it by 1.2.

3.3. Mazurkiewicz's Method

Bengt (1980) suggested this method which is based on the assumption that the load–settlement curve is approximately parabolic. A series of equal pile head settlement lines are arbitrary chosen using equal intervals and the corresponding loads are marked on the abscissa, as shown in Figure 5. For the marked loads on the load axis, a 45-degree line is drawn to intersect with the next vertical line running through the next load point. These intersections fall approximately on a single straight line, the intersection of this line with the load axis defines the ultimate failure load. Smaller settlement interval may introduce more accurate results.

3.4. De Beer's method

In this method, the load–settlement values were plotted on a double logarithmic chart. When the values fall on two approximately straight lines, the intersection of these defines a limit load that is considered a pile yielding load. The method is illustrated in Figure 6 for pile no. 1, as an example pile. Regarding the results a new definition must be introduced for this method namely yielding limit

load. All previously mentioned methods determine a failure load except De Beer. Therefore, one should distinguish between the failure load and the limit load to adopt the proper factor of safety. The pile failure load, which predicted from load–settlement relationships of piles loaded to pre-failure are based on assuming certain shapes of these relationships independent of pile geometry, soil properties, and rate of loading. But the limit load is the load at which the curve begins to be steeper sloped and enters into the plastic behavior zone. This method needs the pile to be loaded near failure, because when the pile is not loaded near failure, the plotted values of the load settlement fall on approximately one straight line and the limit load is not defined.

3.5. Decourt's Extrapolation Method

This method is applied by dividing each load by its corresponding movement and plotting the resulting values against the applied load. Figure 7 shows the result for pile no. 26, as an example pile. The part of the curve that tends to a straight line intersects the load axis. Linear regression over the apparent straight-line determines the required slope C1 and y- intercept C2 constants. Decourt's ultimate load is the value at the intersection with the load axis, Decourt's ultimate load Qu can be accurately calculated as the ratio between the y- intercept and the slope of the line as given in Eq. 7.

$$Qu = C2 / C1 \quad (7)$$

4. Results and Discussion

As mentioned, 6 single-helix, double-helix and triple-helix piles have been constructed in two sites including silty-clay, among which 3 of these 6 piles were used without grouting and 3 of them were used with grouting. The helix spacing to diameter ratio (S/D) was 1.5 and 3 for triple helix and double helix piles, respectively. The load displacement curves are shown in Figures 6 to 10 in comparison with the axial compressive load capacities of the piles tested under grouted and un-grouted conditions.

The results showed that in single-helix piles in silty-clay, compressive capacity increased by approximately 8% after grouting. Similar to the single-helix piles, the pile resistance has increased by about 10% in the double-helix piles. But, in the triple-helix piles, the final load has been increased by about 28% after grouting. The reason was the vast disturbance of the soil around the triple-helix piles, which showed an increase after grouting due to the influence of slurry in the soil around resistance.

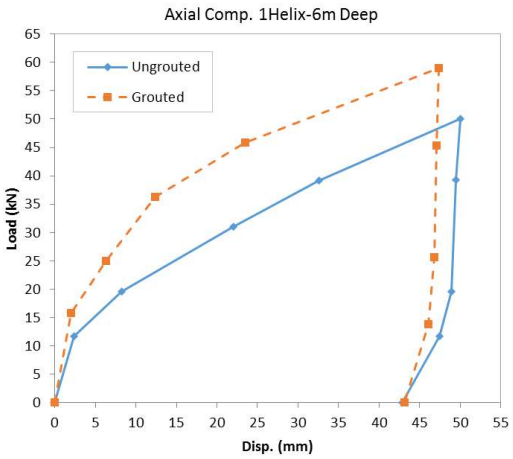

Figure 6: Axial compression load test on piles with one helix in silty-clay

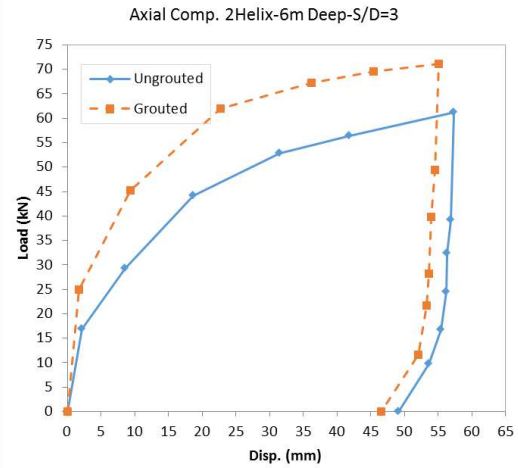

Figure 7: Axial compression load test on piles with two helixes in silty-clay

Generally, load-displacement curves can be divided into three main sections: the first part is done with displacement of about 2 mm linearly and, afterwards, a non-linear component that varied from 35 to 55 mm. It can be seen from the curves that the grouted piles in silty-clay soil have less displacement than the piles without grouting indicated that grouting operation caused an increase in pile resistance. In silty-clay soil, non-grouting triple-helix pile's bearing capacity was more than that of single and double-helix piles. A possible reason for this discrepancy could be that the triple-helix piles had cylindrical performance, and single and double-helix piles had individual performance; therefore, the increased number of helixes resulted in the increased capacity of loading and pile stiffness. In the un-grouted piles, there was no expected pile frictional resistance due to shallow depth and low levels of tension, but when the grouting was done, the resistance increased due to adhesion. Among the grouted piles, triple-helix piles were more effective because the soil of the upper part was scrabbled and grouting filled the cracks and with a further adhesion increase gives greater load capacity.

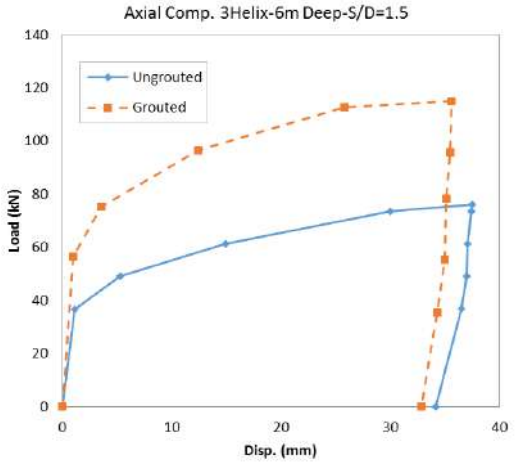

Figure 8: Axial compression load test on piles with three helixes in silty - clay

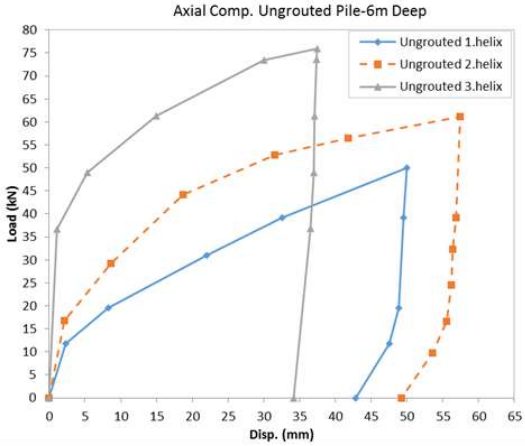

Figure 9: Axial compression load test on un-grouted piles in silty-clay

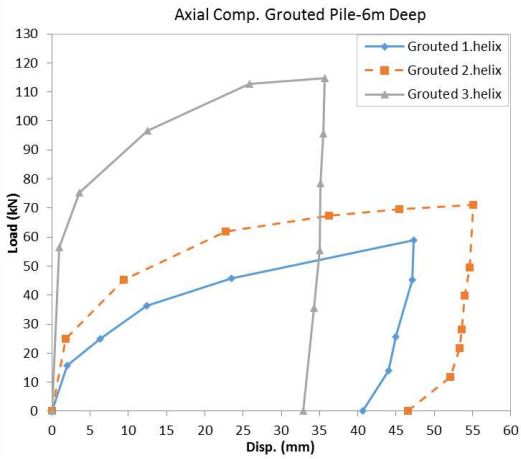

Figure 10: Axial compression load test on grouted piles in silty-clay

Generally, grouting operation in clay had compaction performance, so loading capacity increased.

Furthermore, as can be seen, when comparing load-displacement curves between the grouted and un-grouted helical piles, the data showed that both types of piles had a similar performance and the trend of both types of grouted and un-grouted axial compression load test curves are the same while grouted piles show greater axial compressive strength. The grouted helical piles deflected less at the failure load than the un-grouted ones. This stiffer

response was also very useful in structural support applications.

4.1. Estimation of Ultimate Load from Pile Load Test

A database of six axial static loading tests on single, double and triple helix helical piles under grouted and un-grouted conditions was compiled. The ultimate load capacity Qu for each pile test was predicted using the six different interpretation methods stated in section 3 that are used in the evaluation of the pile load test. A summary of predicted ultimate failure loads is presented in Table 3.

All six tests conducted at the site were assessed to achieve the ultimate load. The ultimate load values obtained for each pile using various methods discussed earlier is presented in Table 3.

As it can be seen from Table 3, the values determined using De Beer's and Davisson's methods are the lowest ones. This is because Davissons, and DeBeer's methods need the pile to be loaded to failure to be applicable and they were proposed to determine the limit load.

Choosing the best criteria for pile axial load capacity is quiet complicated since this is mostly depended on engineer's experiences and mechanism of failure. One of the conservative methods is Davisson's method.

Brinch-Hansen method is in good agreements with real ultimate resistance of pile which gives about 80% of ultimate load calculated based on static loading test.

Chin-Kondner and Decourt methods both are using extrapolation for determination limit load values, hence, the ultimate load gained from both is asymptotically.

As a straight engineering rule never to interpret static loading test result to gain ultimate load larger than the test load. Therefor allowable load should not calculated by dividing the limit loads obtained from Chin-Kondner's and Decourt's methods by a factor of safety.

The Mazurkiewicz method is easy to use and is more reliable especially for piles loaded near failure.

Shortcomings of De Beer's method are mentioned earlier. Hansen's 80%-criterion, Chin's and Decourt's extrapolation methods using the latter part of the load-movement curve and could extrapolated beyond the maximum load applied.

One of the advantages of Decourt's method is that a plot can be drawn while the static loading test is performing which allow the user to eyeball the projected capacity directly once a straight line plot starts to develop.

While in Chin-Kondner's method, if during the static loading test, a weakness in the pile develops, the curve would deviate from straight line. Hence it is significantly desirable plotting the readings as per Decourt's method as the test progresses. Finally these two methods estimate ultimate failure load reasonably.

5. Conclusions

In this study, the behavior of helical piles with different helixes in two sites with silty-clay and sandy soils was investigated. Moreover, the effect of grouting on pile's loading capacity was studied. The ultimate load capacity Qu for each pile test was predicted using the six different interpretation methods that are used in the evaluation of the pile load test. The findings of this study can be summarized in the following conclusions:

1- Compressive capacity increased by approximately 8% after grouting. Similar to the single-helix piles, the pile resistance has increased by about 10% in the double-helix piles. But, in the triple-helix piles, the final load has been increased by about 28% after grouting.

2- grouting operation in clay had compaction performance, so loading capacity increased.

3- In triple-helix pile in silty-clayey soil, adhesion of pile and soil increased along with grouting. As a result, pile resistance was increased in comparison with the un-grouted condition.

4- Load-displacement curves showed that in sandy soil, the initial stiffness of the triple-helix piles was more than that of the double and single-helix piles, respectively.

5- In general, variation of pile strength with different helix numbers was insignificant. But the results of this paper indicated that grouting could considerably improve helical pile's strength.

Table 3: Summary of predicted ultimate failure loads

		Davisson	Hansen	Chin	Mazur	De Beer	Decourt	Test Site Load
		Qu(kN)	Qu(kN)	Qu(kN)	Qu(kN)	Qu(kN)	Qu(kN)	Qu(kN)
1 Helix	Ungrouted	22.5	54.55	53.19	54	12.18	53.7	50
	Grouted	32.5	73.7	63.7	64.9	16.44	61.98	58.9
2 Helix	Ungrouted	33.7	63.7	64.7	65.3	24.17	63.85	63.1
	Grouted	50.2	70.35	72.1	74	36.7	70.63	71.1
3 Helix	Ungrouted	66.2	73.7	77.1	78.3	60	75.4	76
	Grouted	104.7	113.2	115.8	116.3	94.47	114.25	114.8

6- According to various limit load methods evaluation, it was concluded that the values for three methods of Chin, Decourt were close to the site values.

References

[1] El Sharnouby MM, El Naggar MH.; "Field investigation of axial monotonic and cyclic performance of reinforced helical pulldown micropiles"; Can Geotech J (2012) 49:560–73. doi:10.1139/t2012-017.

[2] Tsuha CHC, Aoki N, Rault G, Thorel L, Garnier J.; "Evaluation of the efficiencies of helical anchor plates in sand by centrifuge model tests"; Can Geotech J(2012) 49:1102–14. doi:10.1139/t2012-064.

[3] Cerato AB, Victor R.; "Effects of Long-Term Dynamic Loading and Fluctuating Water Table on Helical Anchor Performance for Small Wind Tower Foundations"; J Perform Constr Facil (2009) 23:251–61. doi:10.1061/(ASCE)CF.1943-5509.0000013.

[4] B.W. Byrne and G.T. Houlsby; “Helical Piles: An Innovative Foundation Design Option for Offshore Wind Turbines”; (2016), J. Phil. Trans. R. Soc. A; 1-17. Doi: 10.1098/rsta.2014.008.

[5] Abdelghany Y, El Naggar M.; "Full-Scale Field Investigations and Numerical Analyses of Innovative Seismic Composite Fiber-Reinforced Polymer and Reinforced Grouted Helical Screw Instrumented Piles Under Axial and Lateral Monotonic and Cyclic Loadings"; Adv. Soil Dyn. Found. Eng., (2014) p. 414–24. doi:10.1061/9780784413425.042.

[6] Perko HA.; "Helical Piles, A Practical Guide to Design and Installation"; Hoboken, New Jersey: John Wiley and Sons, INC (2009).

[7] American Society for Testing and Materials.; "Standard Test Methods for Deep Foundations Under Static Axial Compressive Load, ASTM D1143 / D1143M - 07"; Annu B ASTM Stand (2013) 04.08. doi:10.1520/D1143_D1143M.

[8] Vickars R, Clemence S.; "Performance of Helical Piles with Grouted Shafts"; New Technol. Des. Dev. Deep Found., (2000) p. 327–41.

J-Researchers

JOURNAL OF CIVIL ENGINEERING RESEARCHERS

Seismic strengthening of RC columns using enhanced steel jacket. FE modeling

M.R. Noori Shirazi* [a]

[a] *Assistant Professor of Civil Engineering, Academic Staff of Islamic Azad University, Chaloos Branch, Chaloos, Iran*

Article History: Received date: 26 December 2021; revised date: 28 January 2022; accepted date: 16 February 2022

Abstract

This paper presents a new rectified square steel jacket for retrofitting of poorly confined reinforced concrete columns in flexural plastic hinge regions. All of the analyses was carried out based on finite elements procedure. Having verified the FE modeling, a deficient RC column designed according to pre-1971 codes was considered and eleven specimen with various detail of retrofitting were investigated. Effects of increasing at thickness of plate stiffeners, geometric shape of stiffeners and stiffened length of jacketed column have been studied**.** The results obtained from the parametric study indicated effectiveness of rectified jacket and allow a series of guidelines to be established.

Keywords: RC square column; seismic retrofitting; rectified steel jackets; finite element analysis; ductility; energy dissipation

1. Introduction

Many existing reinforced concrete structures designed and constructed before the application of modern earthquake-resistant design codes are vulnerable to moderate and severe earthquakes scale [1] which recent earthquakes in many parts of the world have demonstrated it [2]. The columns are considered very critical members in many structures especially in bridges and building frames. Reinforced concrete columns which were designed according to practice which did not take into account the importance of plastic deformation and ductility capacity concepts, are commonly deficient in flexural ductility, shear strength, and flexural strength. Lap-splice in critical regions, premature termination of longitudinal reinforcement and poor confinement are the most common causes which affect the efficiency [3]. Although the diameter and spacing of the hoops vary somewhat for different structures in different countries, insufficient transverse reinforcement and inadequate detailing are typical of pre-1971 structures all over the world [4,5].

Based on extensive experimental studies which was carried out for retroffiting of the deficient RC columns, Although advanced composite materials and other methods have been recently studied, the steel jacketing has been widely applied for retrofiting of building and bridge RC columns which increase their strength and ductility [6,7,8].

Several researchers have investigated using of steel jackets for seismic retrofitting of non-ductile reinforced concrete columns. Tomii et al. (1993) proposed a retrofitting method with the so-called “bellows tube” for improving the efficiency of a square-tubed column. Beacause the stress transfer in the longitudinal direction is unavoidable, the initial yielding of the tube due to bending or axial loading is

* Corresponding author. Tel.: +98 1152220526; e-mail address: mr_nshirazi@iaut.ac.ir

expected that resulting in a reduced efficiency for transverse confinement [9]. Aboutaha et al. (1994) investigated the use of rectangular steel jackets for seismic strengthening and repairing of non-ductile rectangular reinforced concrete columns [10]. Priestley et al. (1994) investigated the use of elliptical steel jackets to enhance the shear strength of rectangular columns. However, the profile of the elliptical jacket increases the cross sectional area of retrofitted column and may not be favorable in high traffic viaducts in restricted urban zones. Aboutaha et al. (1996) tested a system, which combined a through bolt with a relatively thin rectangular jacket, and showed enhanced confinement efficiency [9]. Although rectangular jacketing can still be effective in certain circumstances, the relative poor performance of rectangular jackets in confining the concrete core has been experimentally verified (Chai et al. 1990; Mirmiran et al. 1998, 2000; Pessiki et al. 2001) [11]. The rectangular jacket can not effectively provide lateral confinement due to out of plane bulging of steel jacket (Sun et al., 1993; Harries et al., 1999; Tsai and Lin, 2001) [12]. Furthermore, a column retrofitted for shear improvement will normally also require enhanced flexural ductility, which will not be provided by rectangular steel jackets. Thus, confinement for enhanced compression strain capacity or improved lap-splice performance is unlikely to be effective [13]. For improvement of inappropriate behavior of rectangular steel jacket, some researchers proposed various methods. Xiao and Wu (2003) proposed partially stiffened steel jackets and investigated experimentally the efficiency of these jackets in improving ductility, flexural and shear strength in moment resisting frame structures [9]. Griffith et al. (2004) investigated the application of steel plates that attach to the flexural faces of concrete column using bolts and verified its efficiency in improving mechanical behavior of retrofitted column [11]. Ferrocement jacket was introducted by Kazemi and Morshed (2005). This reinforced jacket with expanded steel meshes was used for seismic shear strengthening of short R/C columns. The results of tests indicated that this jacket can be very effective for stregthening of short concrete columns [14]. Choi et al. (2009) proposed a new steel jacketing method for RC columns which two steel plates was applied in form of a double-layered jacket for retrofitting of column and was found the good effectiveness of jackets [15]. Calderón et al. (2009) investigated the design strength of stregthened RC columns using steel caging which is a variation of the steel jacketing technique [16].

To ensure a ductile behavior of a structure for the largest possible horizontal displacement demand, the formation of a plastic hinge at the base of the pier must be favored as the weakest link mechanism of the structure. For reinforced concrete piers, the available ductility is directly related to the longitudinal and transverse reinforcement details [17]. Previous studies (Ang et al. 1989; Wong et al. 1993) have shown that the concrete shear capacity in the plastic hinge region is reduced due to the degradation of concrete under cyclic loading which results decreasing of the shear capacity in the plastic hinge regions [3]. In the columns which were poorly confined in the critical region, the ultimate curvature becomes limited by the compressive strain in the range of 0.005, resulting in relatively low ductility capacity for these members [18]. Thus, stiffening of quad section steel jacketed specimens at the area nearest the ends of the column can be effective for improving the seismic performance of retrofitted columns and can be generalized application of it.

2. Enhanced steel jacket

2.1. Introduction

This method of steel jacketing was initially briefly introducted by Xiao and Wu (2003). At first, relatively thin steel plates were welded (using fillet welding) througthly at the height of the column to form a rectilinear jacket for shear strength enhancement, then additional confinement elements (stiffeners) with various types of desired configuration including thick steel plates, angle section and quad section tubes were welded in the potential plastic hinge regions at the ends of column to ensure the ductile behavior. The space between rectilinear jacket and concrete was filled using grout. For practical aplication, fillet discontinious welding and spacing between stiffeners was designed and selected based on the regulations of the ACI-318 code (2005) [19]**.** A schematic view of the jackets is illustrated in Figures 1(a), 1(b), and 1(c).

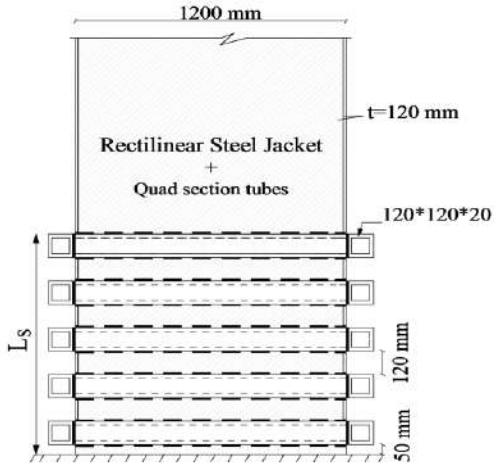

Fig. 1(a). Rectified steel jackets with various geometric shapes of stiffeners : (a) Quad section tube stiffeners

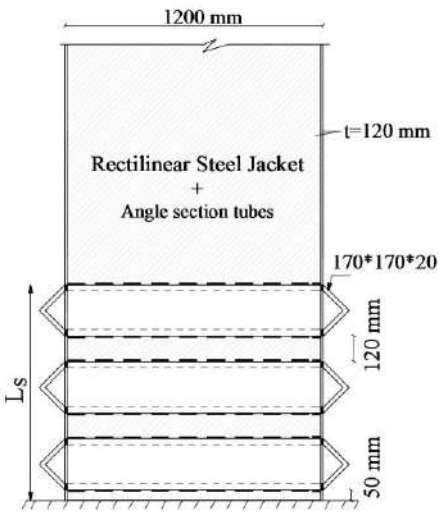

Fig. 1(b). Rectified steel jackets with various geometric shapes of stiffeners: (b) Angle section stiffeners

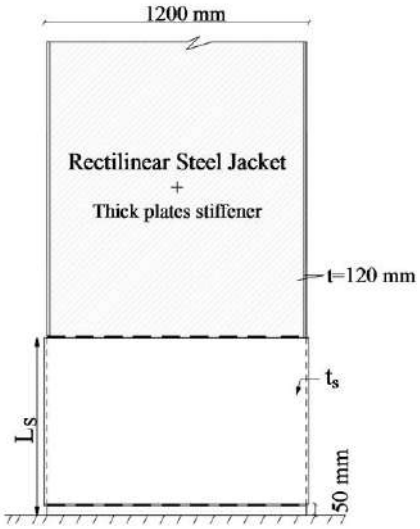

Fig. 1(c). Rectified steel jackets with various geometric shapes of stiffeners:; (c) Thick plate stiffeners

In order to incorporate the stiffeners for stiffening of rectilinear jacket, the potential plastic hinge length must be calculated. For an "as-built" column, i.e. without retrofit, the equivalent plastic hinge length L_p can be estimated using the following equation [20]:

$$L_p = 0.08L + 0.022 f_y . d_b \quad (1)$$

Where d_b= diameter of longitudinal bar, L=original height of the column and f_y= yield strength of the longitudinal reinforcement (MPa). In case of steel jacketed column, the equivalent plastic hinge region can be estimated using the following equation:

$$L_p = g + 0.044 f_y . d_{bl} \quad (2)$$

Where g = vertical gap between the toe of the jacket and the top of footing; f_y= yield strength of the longitudinal reinforcement (in MPa) and d_{bl} = diameter of longitudinal bar [17].

2.2. Research significance

The main characteristics of enhanced steel jacket are less space taken after retrofitting in comparison to the other steel jacket geometeric shapes, creating more flexural ductility at retrofitted column than FRP jackets, adaptability with architectural aspects of retrofitting work and convenience in practical application. Furthermore, the weight of retrofitted column will not be considerably increased and will result in less induced force to the reinforced structure under severe earthquake conditions. The aims of the present study are as follows:

a) Numerical study on the hysteretic behavior of the enhanced steel jacketed deficient RC column;
b) Undertaking nonlinear FE analyses for comparative study between the behavior of rectified and ordinary square steel Jacketed specimens;
c) Investigation about the effect of geometrical parameters on the behavior of retrofitted columns.

3. Finite element modeling

FE method is a powerful tool to effectively simulate the actual behavior of structures specially at the RC building and bridges [21]. In order to simulate as closely as possible the actual behavior of the confined concrete using steel jackets and carry out comparative investigation under axial and cyclic loadings, geometric and material nonlinear finite element analyses have been undertaken. The models were simulated using ANSYS 11.0 finite element software [22].

3.1. Description of the finite elements used, boundary and loading conditions

For modeling of concrete and grout, a 3-D solid element SOLID 65 with eight nodes and three degrees of freedom per node was used which allowing the treatment of nonlinear behavior, including cracking in tension and crushing in compression, plastic deformation and creep capabilities. This element can be used with or without reinforcing bars [23].

Quadrilateral shell elements SHELL 181 have been used for modeling of full height steel jacket. This

element is well suited to model linear, wrapped, and moderately thick shell structures and has plasticity, stress stiffening, large deflection and large strain capabilities allowing the simulation of buckling [23].

A three dimensional solid element SOLID 45 has been used to model the steel stiffeners and has plasticity, stress stiffening, large deflection and large strain capabilities.

For modeling of longitidual and transverse rebars, a three-dimensional spar element LINK 8 has been used. This element is a uniaxial tension-compression element with three degree of freedom at each node and has plasticity, stress stiffening, and large deflection capabilities for appropriate simulation of rebars.

Contact and probable sliding between the steel jacket and grout surface was simulated by the contact element CONTAC 52. The element is located between two adjacent nodes of steel jacket and grout surface, and is capable of modeling separation, sliding and contact between two nodes during the loading process. The element is capable of supporting compression in the direction normal the surfaces and shear in the tangential direction (Coulomb friction). The element has three translational degrees of freedom at each node. A specified stiffness acts in the normal and tangential directions when the gap is closed and not sliding. Fig. 2. shows three-dimensional node to node contact element [23].

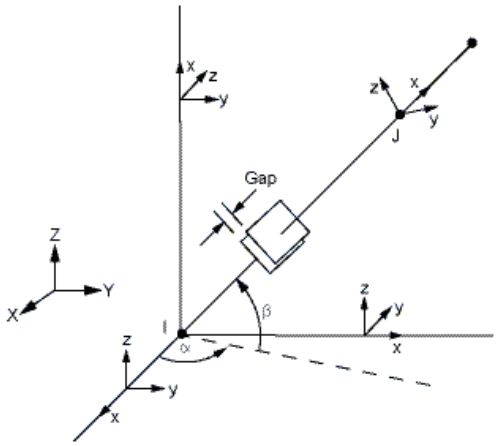

Fig. 2. Three-dimensional node to node element [23]

The number of finite elements included in each model, and the number of degrees of freedom, depend on the type of specimen. For example, for modeling the specimen SJS-AS-S1, 22000 finite elements were used.

3.2. Modeling of concrete, grout and steel

During the process of loading, the concrete in the column becomes confined, since the steel jacket prevents expansion of the concrete due to the Poisson effect. Therefore, it is necessary considering a constitutive model that takes into account the improved strength of the concrete due to confinement. The criterion used to separate the elastic from the inelastic behavior is based on the work developed by Willam and Warnke [24] for concrete under triaxial conditions in the tension and compression regime. The two main strength parameters which needed to define the failure surface are the ultimate tensile strength (f_t) and the ultimate compressive strength (f_c). Regarding the shear transfer coefficients, β_t = 0.25 and β_c = 0.75 are used for the open and closed cracks, respectively. For more information, see reference No.10. For concrete under triaxial conditions, the elastic modules E_x, the poison's ratio ν_{xy}, the values of ultimate tensile strength f_r and ultimate compressive strength f_c are isotropic material properties [23]. As shown in Fig. 3, for steel element and for typical reinforcing steel, the behavior is characterized by an initial linear elastic portion of the stress-strain relationship with a modulus of approximately 200 GPa, up to the yield stress f_y, followed by a strain plateau of variable length and a subsequent region of strain hardening [25].

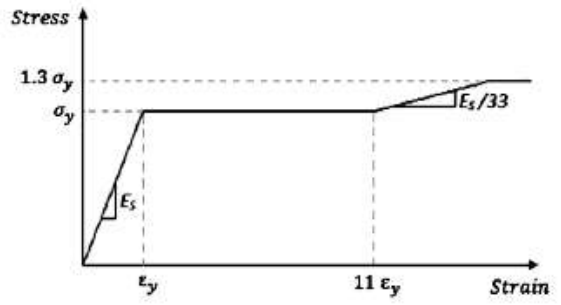

Fig. 3. The stress-strain curve for steel material [25]

For concrete modeling, the used Poisson ratio is $\nu = 0.2$ while the elastic modulus is calculated from below [26]:

$$E_{ci} = E_{co}(f_c / f_{cmo})^{1/3} \quad (3)$$

Where E_{ci} is the elastic modulus, f_c is the compressive strength, f_{cmo} and E_{co} have values as defined in CEB-

FIB Model Code 90. The tensile strength of concrete is obtained in Eq. (4) from f_c, which matches the one specified by CEB-FIB Model Code 90 [26].

$$f_t = f_{ctko,m}(f_c / f_{cko})^{2/3} \quad (4)$$

Where f_t is the tensile strength, f_c is the compressive strength, $f_{ctko,m}$ and f_{cko} are the following parameters defined in CEB-FIB Model Code 90 [26].

Based on founded data from previous carried out investigations, it was detected that after the loading process, the grout between jacket and RC column was undamaged. So it was modeled assuming linear elastic behavior with a Poisson ratio of $\nu = 0.2$ and an elastic modulus of 25 GPa. For modeling the nonlinear behavior of steel reinforcement and steel jacket, the well-known Von Mises yield criterion was used with elastic perfectly-plastic behavior. The elastic modulus used for both types of steel is $E_s = 2100\,MPa$ and Poisson ratio $\nu = 0.3$. The yield stress is $f_{ys} = 400MPa$ and $f_{yl} = 275MPa$ for the reinforcement steel and steel jacket, respectively.

3.3. Interaction between steel jacket and grout

The contact between grout and rectilinear jacket was modeled using contact elements. Coulomb's friction model was used for modeling of slippage as below equation:

$$\tau_{\lim} = a + \mu.p \quad (5)$$

Where $\tau_{\lim}$ is the limit shear stress, a is the contact adhesion, p is the contact normal pressure and μ is the coefficient of friction. In the case of contact cohesion $\mu = 0$ while for the case of friction coefficient between steel and grout the value $\mu = 0.2$ is convenient according to Johansson and Gylltoft [27, 28] and Adam et al. [29, 30].

3.4. Verification of the finite element model

In order to verify the accuracy and validity of the finite element model, the numerical result obtained from material and geometric nonlinear static analysis have been compared with the avilable experimental test data. For more information, see refrence No.7. By carrying out nonlinear structural analysis which Arc-length approach with Full Newton–Raphson Method were used to solve the system of equations, numerical result was compared with experimental data. Fig. 4. and Fig. 5 respectively illustrates deformed shapes of experimental-finite element model and experimental-numerical axial load-axial displacement curve under monotonically axial compressive loading at the end of analysis.

As can be seen, these deformed shapes are similar and for both state, the cross section out of plane bulging of square jacket is obvious. Also, an excellent match can be observed between the FE model and experimental specimen diagram. Considering these results, the finite element model is reliable enough to be used for nonlinear analyses.

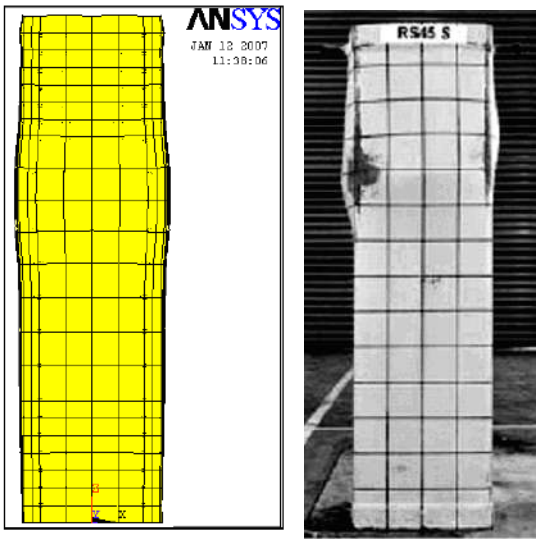

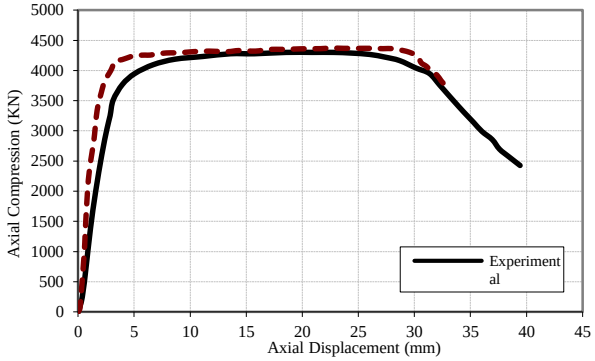

Fig.4. Deformed shapes, (a) Experimental Specimen [12]; (b) Finite Element model

4. Parameteric study

As has been explained in the previous section, the behavior of a RC column strengthened by a steel jacket can be predicted by means of FE modeling. In order to indicate the influence of enhanced jacket for retrofitting, a deficient large scale column designed based on pre-1971 codes [9, 17] which the lateral reinforcement of column was spaced equally at the height of column, was studied. This as-built colmn was regarded as a column located at the ground floor of a tall building. Some assumptions that considered at numerical investigation are as follows:
For all specimens, the thickness of rectilinear jacket was constant

- In all steel stiffeners, regardless of the geometric shape, the used cross section area for stiffeners in the unit length of column height was equal.
- At the base of column, The gap equal to 100mm was applied for preventing of increased moment capacity.
- The curvature in the RC column and the steel jacket is similar at each cross section (i.e., no separation occurs between the concrete and jacket).

4.1. Loading condition and material properties

For all of the analyses, the column specimen was restrained at the base while the top end of it was free (cantiliver column). For modeling the dead load of superstructure, an equivalent axial load about 10% of the gross sectional axial loading capacity, $A_g.f'_c$ [20], was applied for all cases. At the beginning of the analysis, the axial load was applied, then the columns were subjected to a cyclic loading pattern. A shematic view of the normalized displacement history which applied on the tip of the column, was illustrated in Fig. 6. [9]. The analyses were carried out using displacement control method in ANSYS software.

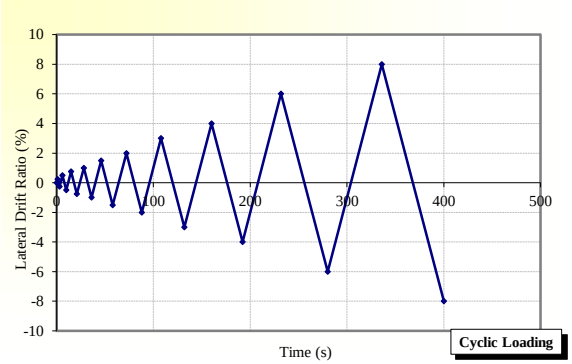

Fig. 6. Lateral drift ratio-time loading history [9]

4-2. Material and geometeric characteristics of column

Table 1 shows the geometric characteristics of as-built column. The summary of material strength and reinforcing bar is illustrated in Table 2, where f'_c =specified strength of concrete, f'_{c_g} = specified strength of grout, F_{yj} = yield strength of steel jacket, F_{yl} = yield strength of longitudinal reinforcement, F_{y_s} = yield strength of transverse reinforcement, ν_s = Poisson ratio of steel, ν_c = Poisson ratio of concrete, t_j = thickness of steel jacket. In Table 2, Lo. Bar and Tr. Bar are the number of longitudinal reinforcements and applied transverse reinforcement, respectively.

According to Table 3, a total of twelve column specimens were selected. At first, “as-built” specimen was retrofitted using designed rectilinear square steel jacket only (benchmark speciemen) and then three groups of enhanced steel jacketed specimens were considered. All of the stiffeners which applied for stiffening of rectilinear jacket in potential plastic hing region at the base of column, was designed and selected based on regulation of ACI-318 code (2005) [19]. At group 1, angle section stiffeners in three various stiffened length were used. At group 2 and group 3, quad section tubes and thick steel plate stiffeners were applied respectively at three lengths along the column height as well.

Table 1
Geometric characteristic of as-built column.

Column Height (mm)	Cross section Geometry	Cross section dimension	Slenderness ratio (L/b)
6000	Square	1200*1200	5

Table 2
Summary of Material Strength and Reinforcing Bars.

f_c'	f_{c_g}'	F_{yj}	F_{yl}	F_{yt}	F_{y_s}	ν_s	ν_c	t_j	Lo.Bar	Tr.Bar
40	80	275	345	303	275	0.3	0.2	12	34 Φ 32	Φ10 at 0.35

Table 3
Geometric properties of specimens

Specimen	Longitudinal Reinforcement	Transverse Reinforcement	Condition of Retrofitting	Full Height Steel Jacket Thickness	Detail of Stiffeners
RC	34Φ32	Φ10 at 350mm	"As-built "	12mm	-
SJO	34Φ32	Φ10 at 350mm	steel Jacket Only (SJO)-*Benchmark*	12mm	-
SJS-AS-S1	34Φ32	Φ10 at 350mm	SJO stiffened by Angle Section	12mm	3 Profile with 170*170*20
SJS-AS-S2	34Φ32	Φ10 at 350mm	SJO Stiffened by Angle Section	12mm	4 Profile with 170*170*20
SJS-AS-S3	34Φ32	Φ10 at 350mm	SJO Stiffened by Angle Section	12 mm	5 Profile with 170*170*20
SJS-QS-S1	34Φ32	Φ10 at 350mm	SJO Stiffened by Quad Section tube	12 mm	2 Profile with 120*120*20
SJS-QS-S2	34Φ32	Φ10 at 350mm	SJO Stiffened by Quad Section tube	12 mm	3 Profile with 120*120*20
SJS-QS-S3	34Φ32	Φ10 at 350 mm	SJO Stiffened by Quad Section tube	12 mm	4 Profile with 120*120*20
SJS-TP-S1	34Φ32	Φ10 at 350 mm	SJO Stiffened by Thick Plate	12 mm	h=800 mm, t=30 mm
SJS-TP-S2	34Φ32	Φ10 at 350 mm	SJO Stiffened by Thick Plate	12 mm	h=800 mm, t=35 mm
SJS-TP-S3	34Φ32	Φ10 at 350 mm	SJO Stiffened by Thick Plate	12 mm	h=800 mm, t=40 mm
SJS-TP-S4	34Φ32	10 at 350 mm	SJO Stiffened by Thick Plate	12 mm	h=800 mm, t=60 mm

According to Table 3, a total of twelve column specimens were selected. At first, "as-built" specimen was retrofitted using designed rectilinear square steel jacket only (benchmark speciemen) and then three groups of enhanced steel jacketed specimens were considered. All of the stiffeners which applied for stiffening of rectilinear jacket in potential plastic hing region at the base of column, was designed and selected based on regulation of ACI-318 code (2005) [19]. At group 1, angle section stiffeners in three various stiffened length were used. At group 2 and group 3, quad section tubes and thick steel plate stiffeners were applied respectively at three lengths along the column height as well.

An estimated length of 800 mm was selected taking into account a potential plastic hinge length of column. Then, Influence of different parameters on the behavior of the specimens was investigated.

4.3. Applied design concepts

Design criteria for steel jackets depend on the primary performance requirement of the retrofit

strategy, identified from a detailed evaluation procedure, including improvement of the flexural ductility, improvement of the integrity of the lap-splice region and improvement of the shear strength. In this study, poorly confined column which expected to sustain large inelastic rotations in plastic hinges, were designed for satisfying confinement requirement and achieving appropriate flexural ductility of column, of which thickness of rectilinear steel jacket was obtained. This jacket thickness was controlled in order to prevent the buckling at longitudinal reinforcement bars and finally, the required extra thickness was added to the total jacket thickness, obtained 12 mm. For more information, see reference No.4.

Based on available data on the geometric and material properties of specimens and in order to explain the design of enhanced steel jacketing method, the plastic hinge length in "as-built" and SJO specimens based on equations 1 and 2 were obtained 723 mm and 586 mm, respectively. These lengths were taken into account for applied length of stiffeners in order to stiffening and reinforcement of the rectilinear quad steel jacket. Based on the proposed method by Xiao and Wu (2003) and regarding the seismic provisions of ACI-318 code (2005) [19], the transverse reinforcement is specified as below to ensure the rotational deformability of the potential plastic hinges near column ends:

$$A_{sh} \geq 0.3\frac{S.h_c.f_c}{f_{yh}}\left(\frac{A_g}{A_{ch}}-1\right) \quad (6)$$

$$A_{sh} \geq 0.09S.h_c.\frac{f_c'}{f_{yh}} \quad (7)$$

where A_{ch}= total transverse steel cross-sectional within space S, f_c'= specified compressive strength of concrete; f_{yh} = specified yield strength of transverse reinforcement; A_g= gross area of section; A_{ch} = cross-sectional area of a column measured out-to-out of transverse reinforcement and h_c = the cross-sectional dimension of column core measured center-to-center of the outermost peripheral hoops. For more information, see reference No.4. Finally, the required area was obtained approximately 1650 mm² and this area was the basis of designing and selecting of Angle, Quad and thick plate stiffeners.

It has been found that the ASCE-ACI 426 approach for estimating the reinforced concrete column shear strength does not provide a particularly appropriate estimate [13]. Thus for calculating the ultimate shear strength, the Priestley approach was applied, shown in the following equation:

$$V_u = V_c + V_s + V_p \quad (8)$$

Where V_c = the minimum shear strength provided by concrete corresponding to large flexural ductility, V_s = the shear strength provided by transverse reinforcement, and V_p = the shear strength contributed by the presence of a compressive axial load, p, on the pier (Priestley et al. 1996). For more details of equation 8, see reference No.2. By replacing the available data for the studied column, V_c, V_s and V_p were obtained 204 KN, 480 KN, and 576 KN, respectively, and finally, the ultimate shear capacity of reinforced concrete column was obtained 1260KN.

5. Numerical results of analyses

The nonlinear material and geometeric FE analysis has been undertakened and the results of analysis which carried out for benchmark specimen was compared to the rectified square steel jacketed specimens. The influence of different parameters including energy dissipation, shear strength, ductility and plastic stiffness was investigated for all specimens.

5.1. Hystertic behavior of specimens

The behavior of the specimens was shown in the form of lateral force-displacement hysteretic relationship. The hysteretic curves for RC and SJO specimens are illustrated In Fig. 7.

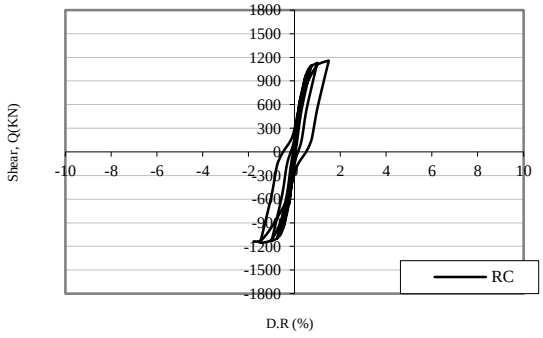

Fig. 7 (a). Lateral force-drift ratio hysteretic responses of specimens: (a) RC specimen;

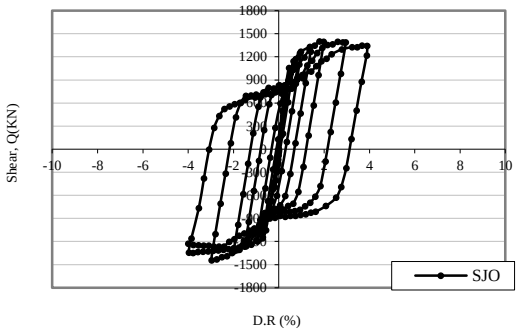

Fig. 7(b). Lateral force-drift ratio hysteretic responses of specimens:

; (b) SJO specimen

It can be seen in Fig. 7(a) that, for RC specimen the maximum shear force carried by the column was about 1153 KN, which was significantly less than the shear force corresponding to the nominal flexural resistance of the reinforced concrete section. Damages in concrete element in the base of column in "pull" direction lead to a loss in load carrying capacity of the column. In Fig. 7(b), in the benchmark specimen, the shear force in terms of relative displacement is linear up to the second cycle of loading. In fourth to sixth cycle of loading, inelastic deformation occurred without significant loss of capacity. A maximum shear force equal to 1397 KN was achieved in drift ratio of 2%, which is larger than the nominal flexural capacity. The significant loss of capacity in the "pull" direction between drift ratio of 2% and 4% is due to the longitudinal bars' failure in the base of column. Flexural cracks were formed at the base of column, which are associated with the formation of plastic hinge in the gap region. It has been found that, the column could not continue sustaining applied loads because of inadequate confinement of concrete core and out of plan bulging of steel jacket near the base of column. It is worth noting that Xiao and Wu (2003) investigated the behavior of ordinary steel jacketed column and concluded that maximum drift ratio in "push" and "pull" directions was respectively 6% and 4%. The column failure was initiated by the out of plane bulging of the steel jacket near column ends followed by rupture at welded corners and degradation of shear capacity was started at 1.5% lateral drift ratio because of higher exerted axial load on column [9].

In order to study the influence of angle section stiffeners on the behavior of a square steel jacketed specimen, three, four and five angle section profiles with dimensions of 170×170×20 (in mm) designed based on the aforementioned procedure, were used along the column height. Dimensions of the angle stiffener was controled for preventing of local buckling. Angle profiles were located equally in constant space of 120 mm. The hysteretic curves of shear force in terms of relative displacement for these specimens was shown in Fig. 8. For all specimens, the maximum shear force occurred at 4% of lateral drift ratio. For example, this quantity for SJS-AS-S3 specimen is about 1636 KN which is obviously larger than the calculated ultimate shear strength. By continuing the loading up to cycle No.8, degradation of shear capacity was observed and continued to the final cycle. In contrast to the benchmark specimen and in an equal cycle of loading, degradation of shear capacity decreased because of good confinement of concrete core and preventing the out of plane bulging in cross section of square steel jacket. In general, the hysteretic behavior of specimens is stable and increaseing in ductility for rectified steel jacketed specimens is intuitive.

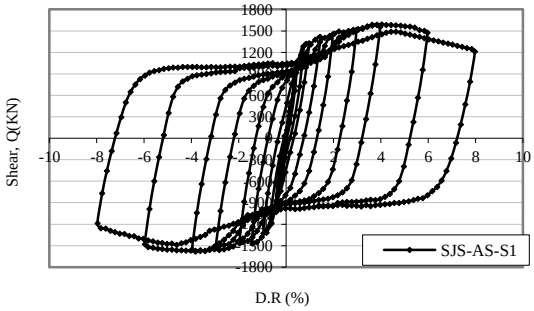

(a)

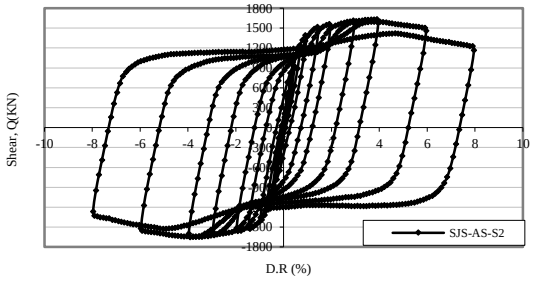

(b)

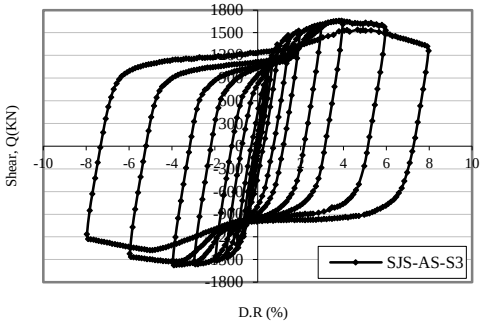

(c)

Fig. 8. Lateral force-drift ratio hysteretic responses of angle section stiffened steel jacket specimens: (a) 3 angle stiffened square steel jacket; (b) 4 angle stiffened square steel jacket; (c) 5 angle stiffened square steel jacket

It was observed that increaseing in the number of angle profiles or in other words the increasing in the confined length of column height results in a decrease in degradation of shear strength in drift ratio between 4 to 8%. It is worth noting that the investigation carried out by Xiao and Wu, indicated that the maximum lateral drift ratio was about 8% in "pull" and "push" directions (due to the limitation in travel range of the loading equipment) and degradation of specimens was started at 3% lateral drift ratio, because the applied axial load on the column was higher than present study. Excellent performance with significantly increased ductility and stable hysteretic behavior was observed for retrofitted specimens with ultimate drift ratio exceeding of 8%. All retrofitted columns with partially stiffened steel jacketing developed load-carrying capacities exceeding the calculated ideal flexural strength $V_i f$ at peak drift ratios exceeding 1%. An about 20% over-strength compared with $V_i f$ was developed at the peaks of subsequent loading cycles. This increase is considered to be the consequence of sufficient confinement and strain hardening of longitudinal steel [9]. In continue, three, four and five square section tubes with dimensions of 120×120×24 (in mm) were used for stregthening of rectilinear square steel jacket and were located equally in constant space of 120 mm. Dimensions of the stiffeners must be satisfactory for preventing the local buckling of stiffeners. The hysteretic curves of shear force in terms of relative displacement for these specimens are shown in Fig. 9.

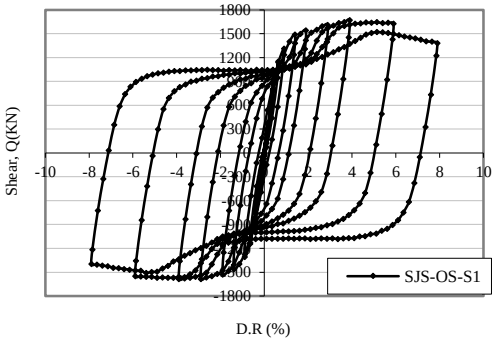

(a)

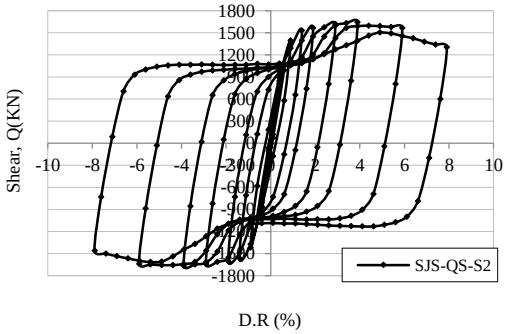

(b)

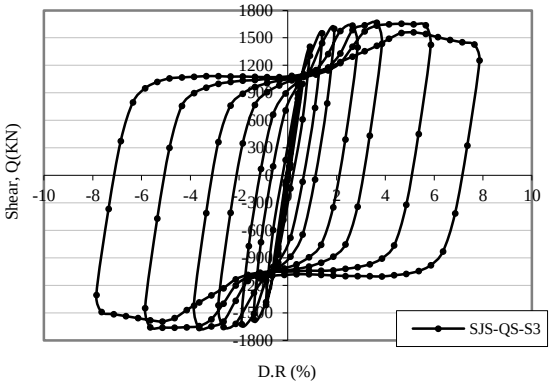

(c)

Fig. 9. Lateral force-drift ratio hysteretic responses of quad section stiffened steel jacket specimens; (a) 3 quad section tubes, (b) 4 quad section tubes; (c) 5 quad section tubes

All specimens were carried 10 cycles of loading in "pull" and "push" directions. The maximum shear capacity in all specimens was achieved in cycle No.8 of loading. For example, this quantity for SJS-QS-S3 specimen was about 1665KN which is obviously larger than the calculated ultimate strength V_u. In comparison to the benchmark specimen and at the

same lateral drift ratio (for example 1%), the degradation of shear strength was decreased and the specimen exhibited stable hysteretic behavior and enhanced ductility behavior. Regarding the Fig. 9, it is obvious that by increasing at the confinement length of stiffeners or in other words, by increasing at the number of profiles, degradation of shear strength in equal drift ratio slightly decreased because of appropriate hysteretic behavior of rectified steel jackets. It is worth noting that Xiao and Wu obtained similar results for this type of stiffeners. For more information see reference No.4.

In continuty of parameteric study, the length of the thick steel plate stiffener was considered 800 mm which is larger than the calculated potential plastic hinge length (586 mm). The various thicknesses of steel plate stiffener were selected including 30, 35, 40 and 60mm (designed thickness). In Fig. 10, the hysteretic curves of the shear force in term of the relative displacement for these specimens are illustrated.

As can be seen at Fig. 10, the maximum shear force for all specimens was observed in cycle No.8 of loading. For example, this parameter for SJS-TP-S4 specimen is equal to 1688 KN which is obviously larger than the calculated ultimate shear strength. The total hysteretic behavior of the column is stable and in comparison to the benchmark specimen (in the same cycles of loading), the degradation of column shear strength was obviously decreased. Considering these figures, it was found that an increase in the steel plate thickness can improve hysteretic characteristics of the column, but when the maximum moment resistance of cross-section has been achieved, this increase does not have a significant effect in improving the mechanical properties of the columns.

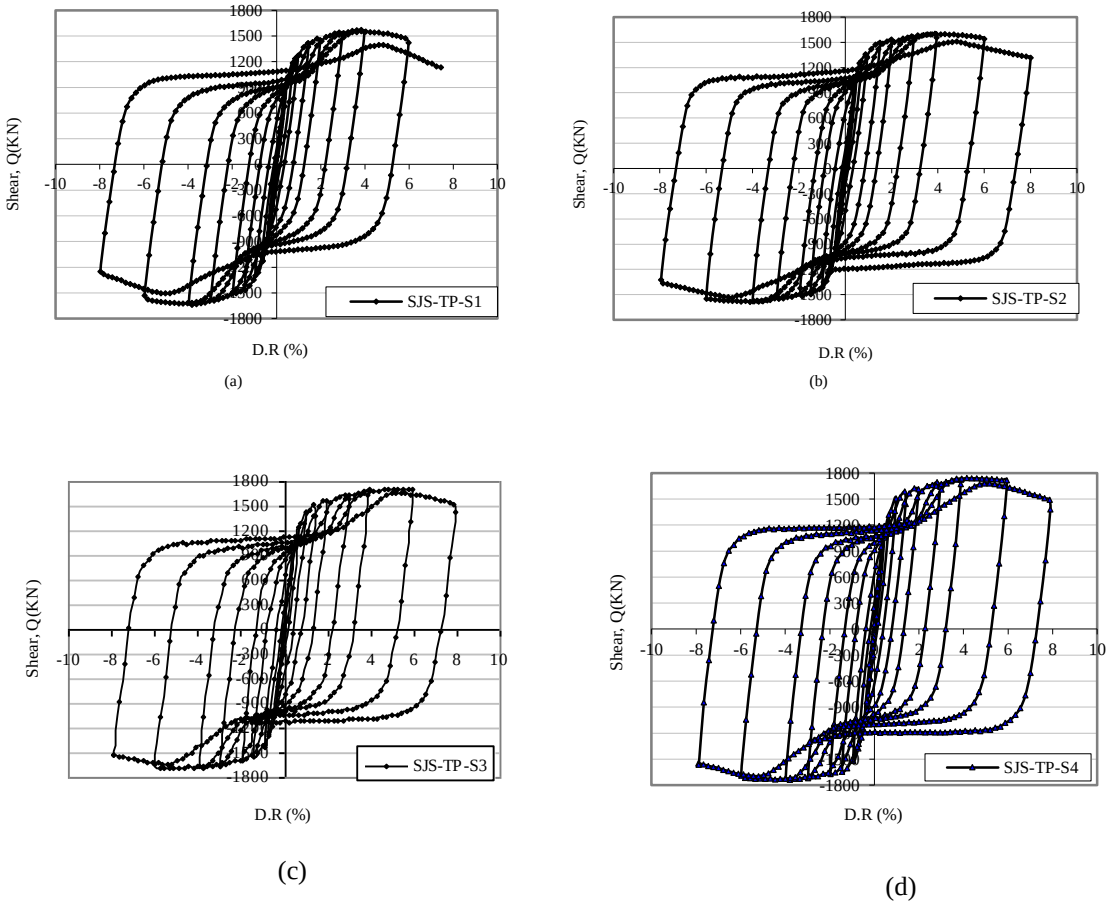

Fig. 10. Lateral force-drift ratio hysteretic responses for thick steel plated specimens: (a) steel plate stiffener (t=30 mm); (b) steel plate stiffener (t=35 mm); (c) steel plate stiffener (t=40 mm); (d) steel plate stiffener (t=60mm)

5.2. Envelopes of shear force versus lateral drift ratio

Fig. 11. illustrates the lateral load-displacement envelopes for comparison between rectified steel jacketed and other specimens.

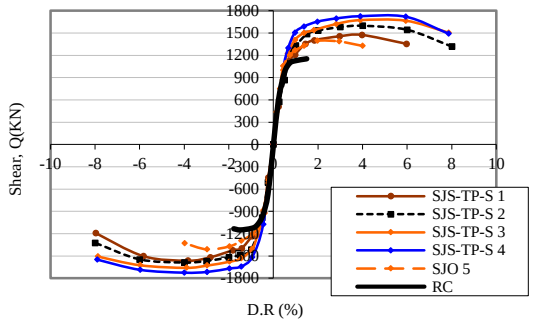

(a)

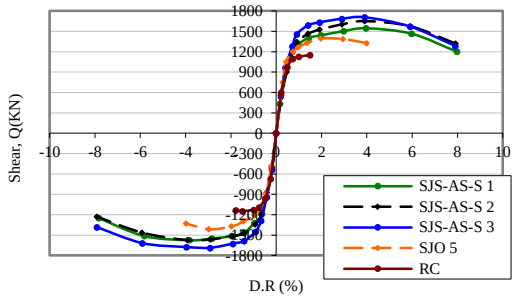

(b)

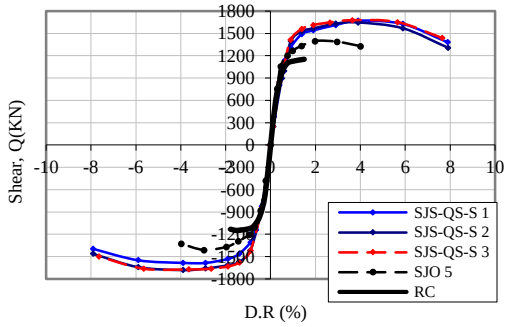

(c)

Fig. 11. Lateral load-displacement comparative envelopes between various specimens: (a) angle section stiffened square steel jacketed specimen versus RC and SJO; (b) quad section tube stiffened square steel jacketed specimen versus RC and SJO; (c) thick steel plated square steel jacketed specimen versus RC and SJO

Each point of envelope is the maximum shear force carried by the column at each corresponding cycle of loading. Due to the appropriate influence of stiffeners on strengthening of performance of square steel jacket, enhancement in shear strength and ductility ratio is obvious. For example, the SJS-TP-S4 specimen exhibited increasing equal to 18.8% in shear strength at cycle No.8 compared to the benchmark specimen, or the SJS-AS-S3 specimen**,** exhibited an increasing of 15.2% at shear strength ratio**.** Also comparisons between other specimens was depicted in this figure. For all specimens, ductility ratio was improved and less degradation in shear strength of specimens was observed as well, which indicates desirable effects of stiffeners on the improving the hysteretic behavior of square section steel jacket.

In Fig. 12. deformation of column specimens at the end of loading are illustrated

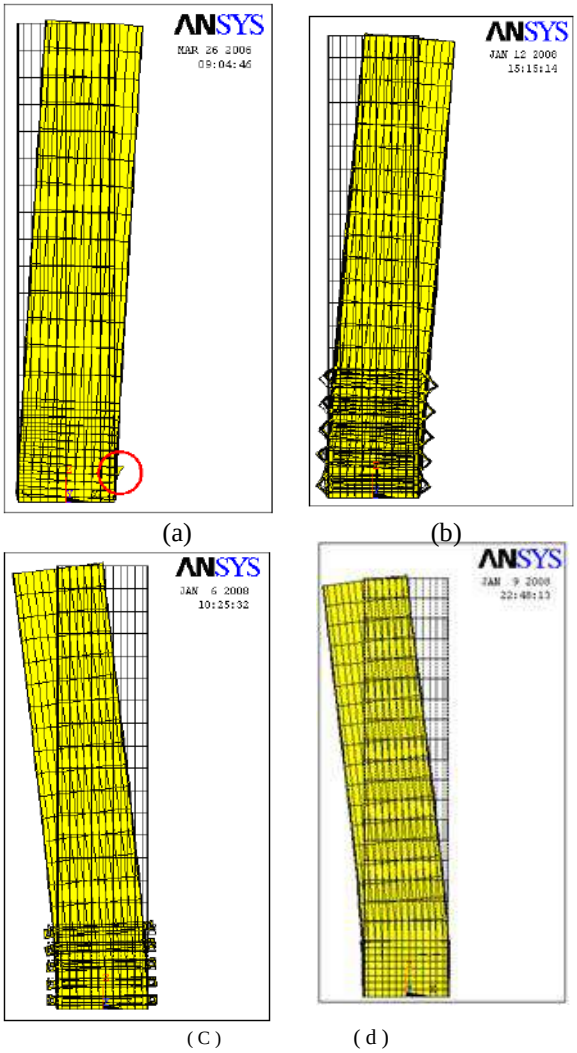

Fig. 12. Deformation of specimens at the end of analyses: (a) SJO specimen; (b) SJS-AS-S 3 specimen; (c) SJS-QS-S3 specimen; (d) S-SJS-TP-S4

For the benchmark specimen, the collapse of square steel jacket at the base of column was observed, thus ductility of the column was restricted by collapse in plastic hinge region. It can be seen that by application of stiffeners in the potential plastic hinge region, the confinement level of concrete core increased and desirable rotation ductility was obtained because of preventing out of plan bulging of square steel jacket. Thus, the column was able to withstand more deformation under lateral loading conditions. It is worth noting that the results obtained by Xiao and Wu (2003) confirmed achieved aforementioned results in the present study. For more details, please see reference No.4.

5.3. Energy dissipation

The ability of a structure to survive earthquake conditions depends mostly on its ability to dissipate the input energy. Various energy forms in structures include kinetic energy, damping energy, elastic energy, hysteretic energy and input energy. Therefore, investigation into the influence of rectified steel jacket on the hysteretic energy dissipation can be an effective criterion for evaluation and comparison of performance. The area enclosed by the corresponding load-displacement hysteretic curve is a criterion for dissipated energy in any particular cycle of loading [2]. In Fig. 13, the comparative investigation between various types of rectified steel jacketed and other specimens was illustrated.

It can be seen that at the steel jacketed specimens and in initial cycles of loading, the presence of jacket wasn't very effective, but in cycle No.5 of loading an obvious improvement in the energy dissipation process was observed. The dissipated energy of RC specimen decreased at final cycle of loading, whereas this quantity in other specimens has been increased because of good performance of steel jacket into hysteretic behavior of retrofitted column. In case of rectified steel jacketed specimens, using of angle and quad section stiffeners on a longer length of column height resulted in an increase of dissipated energy in each cycle of loading compared to the benchmark specimen.

For example, in SJS-AS-S3 specimen, dissipated energy was about 7.2% more than that of SJS-AS-S1 specimen or in SJS-QS-S3 specimen this quantity was approximately 8.7% more than that of SJS-QS-S1 specimen. Increasing the thickness of steel plate stiffeners led to an increasing at the dissipated energy in a cycle of loading compared to the benchmark specimen.

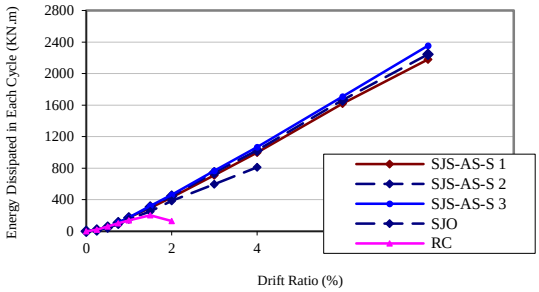

(a)

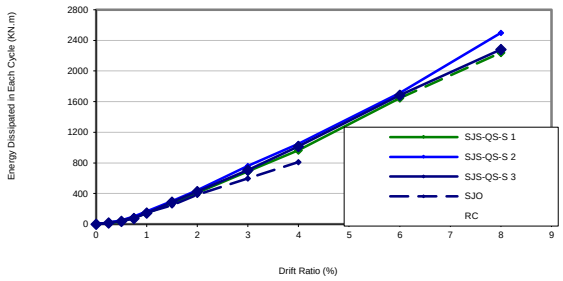

(b)

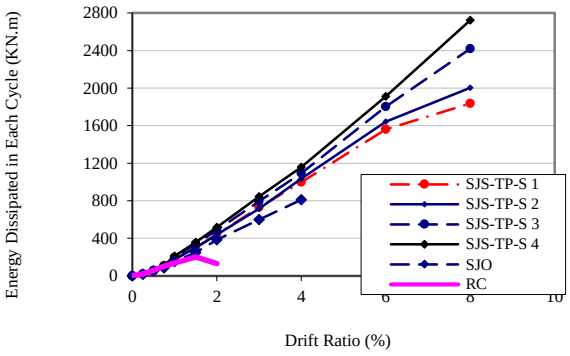

(c)

Fig. 13. Energy dissipated- lateral drift ratio comparative diagrams: (a) Angle section stiffened specimens versus RC and SJO; (b) Quad section stiffened specimens versus RC and SJO; (c) thick steel plated specimens versus RC and SJO

For instance, this quantity in SJS-TP-S4 specimens was approximately 11.2% more than that of SJS-TP-S1 specimen. It should be noted that increasing at the thickness of jacket can increase ductility and energy dissipation as long as the maximum moment resistance of cross-section is achieved [11]. Based on finding from aformentioned disscussion, it was founded that using different types of stiffeners for reinforcing the rectilinear square steel jacket for improving the ductility results in more energy dissipation in

comparison to the ordinary square steel jacketed specimen.

5.4. Stiffness deterioration

Ideally, the stiffness should not be degraded under cyclic loading history. Also it must be large enough to control drift and should be consistent to the deformation limits of non-structural elements. The stiffness of the specimen was evaluated using peak-to-peak stiffness (secant stiffness) from the load-displacement curves. The secant stiffness (k_p) is the slope of the line that joints load peaks in the same cycle [2]. It can be seen in Fig. 14. that at each group, one sample specimen for comparison was selected and adjusted with the benchmark and RC specimens. It is obvious that the initial slope (elastic stiffens) of curves is constant for all specimens except RC specimen, because the presence of the stiffeners has not any effect on it. After lateral cycle No.1 of loading and in drift ratio of 0.5%, degradition of stiffeness was initiallized but the intensity of it for enhanced steel jacketed specimens in comparison to RC and SJO specimen was less. For example, at SJS-QS-S3 specimen and in drift ratio of 2%, the secant stiffness of column was 48% more than that of the benchmark specimen. Also, it is found that the stiffeness for all enhanced steel jacketed specimens in each percent of drift ratio approximatly is same, thus the shape of stiffeners does not have a great influence at the secant stiffness of rectified steel jacketed specimens. The quantitative comparison between some parameters such as maximum shear strength, energy dissipated in cycle No.8, and plastic stiffness in cycle No.8 for rectified steel jacketed specimens and benchmark specimen is given in Table 4.

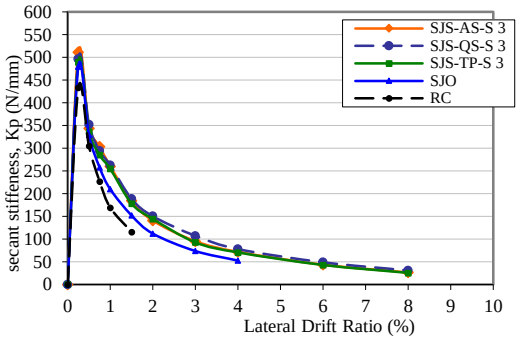

Fig. 14. Stiffness-Lateral displacement ratio relationship

Considering the maximum shear strength parameter, all rectified steel jacketed specimens have differences of a minimum of 15% more than that of the benchmark specimen. Also, the SJS-TP-S4 specimen has the maximum value of shear strength because of more thickness of stiffeners in cross section of the specimen. Considering the energy dissipation parameter, rectified steel jackets had at least a value of 8% improvement in comparison to the benchmark specimen**.** Furthermore, the SJS-TP-S4 specimen has absorbed maximum value energy of 1097 KN.m. For plastic stiffness in cycle No.8 of loading, stiffened steel jacketed specimens exhibited a minimum value of 34% increase against to the benchmark specimen. Also the SJS-QS-S3 specimen had a secant stiffness equal to 70.64 N/mm.

Table 4
Comparison of different parameters between rectified steel jacketed and benchmark specimens.

Specimen	Maximum Shear Strength (KN)	Ratio	Energy dissipated (KN.m)	Ratio	Stiffness plastic (N/mm)	Ratio
SJO	1420	1.00	810	1	52.65	1
SJS-AS-S3	1636	1.152	1068	1.32	71.9	1.36
SJS-QS-S3	1665	1.172	1048	1.29	77.94	1.48
SJS-TP-S4	1688	1.188	1107	1.36	70.64	1.34

6. Conclusions

In the present study, due to the unique desirable characteristics of square steel jackets, they were used for retrofitting of RC columns. Numerical models were verified from the experimental results and a parametric study using the nonlinear finite element analysis was carried out for investigation the influence of each of the parameters on the behavior of RC columns strengthened by steel jackets. The effects of the following parameters have been studied: increase in plate stiffeners thickness, geometric shape of stiffeners and results obtained from the parametric study allow a series of guidelines to be established. Strictly speaking, the scope of the conclusions is limited to the selected column specimens. However, it is likely that the conclusions are of more general applicability.

Considering to assumption of equal area for stiffeners, the geometric shape of stiffeners does not have a great influence on the dissipated energy, stiffness, and shear strength parameters.

Using of stiffeners for strengthening of square steel jackets, degradation of shear strength in the last same cycles of loading was decreased in hysteretic curves and resulted in increasing at shear strength of retrofitted specimens

Stiffeners was not effective at elastic stiffness of column, but along the inelastic range and in the final cycles of loading, plastic stiffness was increased for enhanced steel jacketed specimens.

Increasing in applied length of stiffeners led to increase in energy absorption capacity. It is also noticeable that based on the various finite element analyses, minimum length in which the stiffeners can be effective, must be about 10-20% larger than that of the analytical length of plastic hinge regions.

Increasing in thickness of plate stiffeners, improves hysteretic behavior and flexural capacity of columns, but this increasing was limited by achieved maximum flexural moment of column section.

References

[1] Liu Tao, Fengwei, Zhang Zhi-mei, Ouyang Yu. Experimental study on ductility improvement of reinforced concrete rectangular columns retrofitted with a new fiber reinforced plastics method. J Shanghai Univ 2008;12(1):7–14.

[2] Gobarah A, Biddah A, Mahgoub M. Rehabilitation of reinforced concrete columns using corrugated steel jacketing. J Earthquake Eng 1997; Imperial College Press,4(1):651-73.

[3] M. Saiid Saiidi, Nadim I. Wehbe, David H. Sanders, Cory J. Cawwood. Shear retrofit of flared RC bridge columns subjected to earthquakes. J Bridge Eng 2001;3(6):189-97.

[4] Ricardo Perera. A numerical model to study the seismic retrofit of RC columns with advanced composite jacketing. Composites, Part B, engineering 2006;37:337–345.

[5] Sause R, Harries K A, Walkup S L, Pessiki S, Ricles J M. Flexural behavior of concrete columns retrofitted with carbon fiber-reinforced polymer jackets. ACI Struct J 2004;101(5):708–716.

[6] Kim S.H, Shinozuka M. Development of fragility curves of bridges retrofitted by column jacketing. Probabilistic Engineering Mechanics 2004;19:105-12.

[7] Chai YH, Priestley MJN, S Seible F. Seismic retrofit of circular bridge columns for enhancing flexural performance. ACI Struct J 1991;88(5):572–84.

[8] Priestley MJN, Seible F, Xiao Y, Verma R. Steel jacket retrofit of squar RC bridge columns for enhanced shear strength. Part 1: theoretical considerations and test design; Part 2: experimental results. ACI Struct J 1994;91(5):537–51.

[9] Yan Xiao, Hui Wu. Retrofit of reinforced concrete columns using partially stiffened steel jackets. J Struct Eng 2003;129(6):725-32.

[10] Aboutaha RS, Machado RI. Seismic resistant of steel–tube high-strength reinforced-concrete columns. J Struct Eng 1999;125(5):485-94.

[11] Griffith MC, WU YF, Oehlers DJ. Behavior of steel plated RC columns subject to lateral loading. Advances in Structural Engineering 2005;8(4):333-48.

[12] Keh-Chyuan Tsai and Min-Lang Lin. Seismic jacketing of RC columns for enhanced axial load carrying performance. J of the Chinese Institute of Engineers 2002;25(4):389-402.

[13] Priestley MJN, Seibel F, Calvi GM. Seismic design and retrofit of bridge, A Wiley-Interscience Publication, 1996.

[14] M T. Kazemi, R Morshed. Seismic shear strengthening of R/C columns with ferrocement jacket. Cement & Concrete Composites 2005;25:834–42.

[15] Choi E Park, J Nam, T H Yoon, S J. A new steel jacketing method for RC columns. Magazine of Concrete Research 2009;61(10):787-96.

[16] Pedro A. Calderón, Jose M. Adam, Salvador Ivorra, Francisco J. Pallarés and Ester Giménez. Design strength of axially loaded RC columns strengthened by steel caging. Materials & Design 2009;30(10):4069-80.

[17] Xavier Daudey, Andre Fillatrault. Seismic evaluation and retrofit with steel jackets of reinforced concrete bridge piers detailed with lap-splices. Can. J. Civ. Eng 2000;27:1-16.

[18] Chai YH, Priestley MJN, Seible F. Analytical model for steel-jacketed RC circular bridge columns. J Struct Eng 1994;120(8):2358-76.

[19] American Concrete Institute (ACI) 318. Building code requirements for reinforced concrete and commentary, ACI 318-2005/ACI 418R-2005, Farmington Hills, Mich, 2005.

[20] Chai YH. An analysis of the seismic characteristics of steel-jacketed circular bridge columns. Earthquake Engineering and Structural Dynamic 1996;25(2):149-61.

[21] Kwon M, Spacone E. Three-dimensional finite element analyses of reinforced concrete columns. Computers & Structures 2002;80:199-212.

[22] ANSYS, Release 11.0. Element reference. SAS IP, Inc.; 2006.

[23] ANSYS, Release 11.0 Theory reference. SAS IP, Inc.; 2006.

[24] Johansson M, Gylltoft K. Structural behavior of slender circular steel– concrete composite columns under various means of load application. Steel Compos Struct 2001; 4:393–410.

[25] Abedi K, Ferdousi A, Afshin H. A novel steel section for concrete-filled tubular columns. THIN-WALLED STRUCTURES 2008;46:310-19.

[26] CEB-FIB Model Code 90. Laussane, 1991.

[27] Adam JM, Ivorra S, Giménez E, Moragues JJ, Miguel P, Miragall C, Calderón PA. Behavior of axially loaded RC columns strengthened by steel angles and strips. Steel Compos Struct 2007; 7(5):405–19.

[28] Johansson M, Gylltoft K. Structural behavior of slender circular steel–concrete composite columns under various means of load application. Steel Compos Struct 2001; 4:393–410.

[29] Johansson M, Gylltoft K. Mechanical behavior or circular steel-concrete composite stub columns. J Struct Eng 2002; 128(8):1073–81.

[30] Adam JM, Calderón PA, Giménez E, Hidalgo C, Ivorra S. A study of the behavior of the cement mortar interface in reinforced concrete columns strengthened by means of steel angles and strips. Structure Faults Repair 2006, Edinburgh.

J-Researchers

JOURNAL OF CIVIL ENGINEERING RESEARCHERS

The effect of the perforated pattern on the energy absorption capacity of the steel plate shear wall

Hadi Darvishi[a,*]

[a]*Center of Excellence in Structures and Earthquake Engineering, Civil Engineering Department, Sharif University of Technology, P.O. Box 11155-9313, Azadi Ave., Tehran, Iran*

Journals-Researchers use only: Received date here; revised date here; accepted date here

Abstract

In addition to the conventional lateral load resistance system such as different brace system, using of another kind of system that called Steel Plate Shear Wall (SPSW) is extending. Most of the SPSW that used in the construction of the building structure are stiffened by other elements that perpendicular to the frame surface to prevent their buckling. Recent studies show that the performances of this kind of lateral load resistance systems will be improve if the infill plate buckled before the yielding of the surrounding frame. So using of too thick plate is developed that accrued some construction problem and decrease the economic advantage of them. Using of the perforated steel plate shear wall is an applied strategy to remove this problem and lead to the buckle of the infill plate. Using of the perforated steel plate incorporate some confusedness base on the lacking of the code. In this paper 21 number of perforated steel plate shear walls analyzed under cyclic loading by using of the ABAQUS. An appropriate perforated pattern is suggested by study on the hysteresis diagrams. The results show that using of bad pattern reduces the ability of energy absorption and suddenly remove the stability of the SPSW. Otherwise, using of the proper pattern improve the cyclic performance of the perforated steel plate shear wall camper to the other system.

Keywords: Shear wall, Perforated Infill Plates, Low yield steel, Cyclic load;

1. Introduction

Steel Plate Shear Wall (SPSW) is a panel that surrounded by tow beams and columns and a steel plate which is connected to these boundary elements. For construction, this system is too simple and does not have any special complexity; so engineers, technicians and workers can construct it with their knowledge and do not need any newer education. This system can be produced in the factory. So they can consider as a fast assembly, economic and prefabricated system. Steel plate shear walls have initial high stiffness and ductile behaviour under inelastic cyclic deformation; and dissipate the noticeable amount of energy [11, 12]; so they are one of the suitable lateral load resistance systems. Steel plate shear wall is not only used in the construction of new building; they can use for retrofitting of existing structure, too [9, 10, 15].

Finding a plate with actual design thickness is a problem of construction of unstiffened steel plate shear wall, because the plate thickness that calculated

* Corresponding author. Tel.: +989125733178; e-mail: h_darvishi65@yahoo.com

according to the design equations are too small, almost one mm. as the surrounding beams and columns are designed base on infill plate thickness, so using of thinner infill plate can change the dimension of these boundary element. Recently, for removing such a problem, using of the low yield steel [14, 16], cold rolled [9], light-gauge [9] and perforated steel plate [13, 16, 17, 18] and some other method are proposed to decrease the strength and the stiffness of the system. Some studies are conducted on reduced beam section (RBS) as a beam-column connection to reduce the demand of system [16, 17, 18].

In this paper, 21 perforated steel plat shear wall system are analysed under cyclic loading to propose a prorated pattern of perforated plate and study the effect of the perforate arrangement on the ability of the energy absorption.

Please read these instructions carefully and print them. At the end of the instructions you will find a button that removes this text and prepares the document for your text. (Note that this button may not work properly if you change in any way this text.) Use the styles, fonts and point sizes as defined in this template, **but do not change or redefine** them in any way as this will lead to unpredictable results.

2. Method of study

In this paper, a single-story Steel Plate Shear Wall that proposed by Vian and Bruneau is used [18, 19]. As it shown in Fig. 1, the span lengths (L) and the high of the story (h) are equal to 4000 mm and 2000 mm, respectively, so the ratio of the L/h will be 2.0. W18X71 and W18X65 are used as a vertical and horizontal frame section, respectively. And a Low Yield Steel plate with 2.6 mm thickness is used as an infill plate. For ensuring of the beam inelastic behaviour, the RBS beam-column connection is used. By using of the RBS connection the strong-column/weak-beam criteria is satisfied. A solid panel model is shown schematically in Fig. 1.

21 different types of models with perforated infill plate are used. The diameter of all holes is equal to 150 mm. They are named base on the perforated pattern and their angles. The typical name of the models is Number#1-Number#2-(I, II, III) that the Number#1 indicate on the angle between the holes direction and the vertical axes; The Number#2 is referred to the number of the holes and (I, II, III) shows the especial pattern of the hole's location. (Fig. 2)

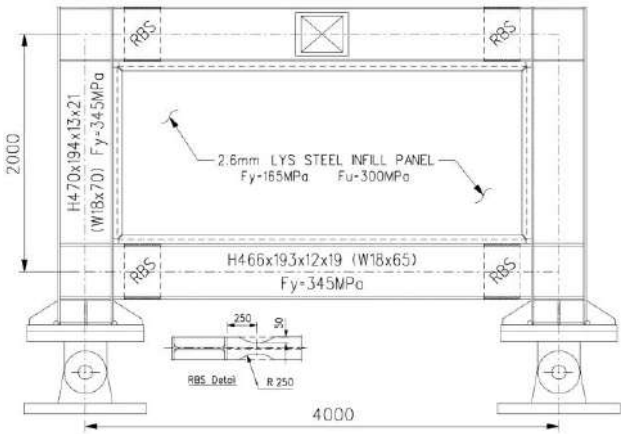

Fig. 1. Typical model dimension Vian, Bruneau et al. [19].

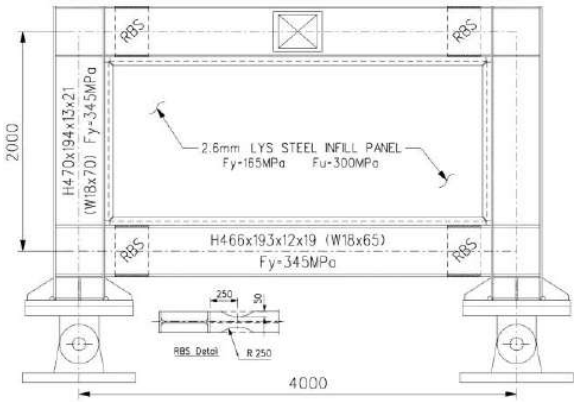

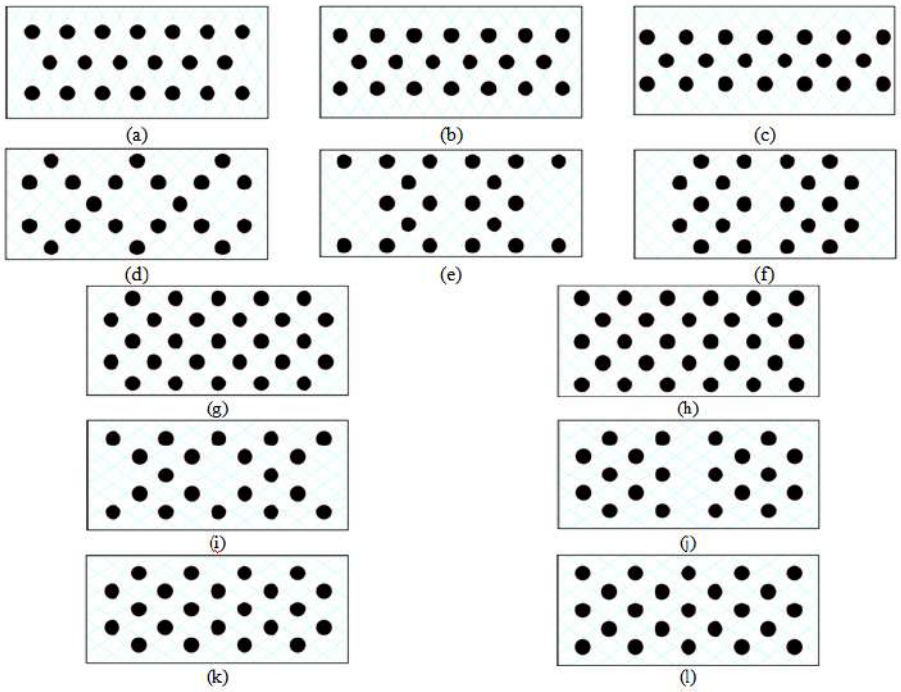

Fig. 2. The perforated pattern: (a) .30°-20, (b) .35°-20, (c) .40°-20, (d) .(45°~50°)-20-I, (e) .(45°~50°)-20-II, (f) .(45°~50°)-20-III, (g) .(45°~50°)-27, (h) .(45°~50°)-28, (i) .(55°~60°)-20-I, (j) .(55°~60°)-20-II,
(k) .(55°~60°)-22, (l) .(55°~60°)-23

3. Material properties

The ASTM-A52 is used as a surrounding frame material with 345 MPa and 540 MPa yield and ultimate stress, respectively Fig. 3-a. Low yield steel with 165 MPa and 300 MPa yield and ultimate stress, respectively is used as infill plate Fig. 3-b. Using of LYS in the infill plate is resulted to the yield of the plate before the boundary elements. For both types of steel, the module of elasticity is 200 GPa and the Poisson's ratio is 0.3.

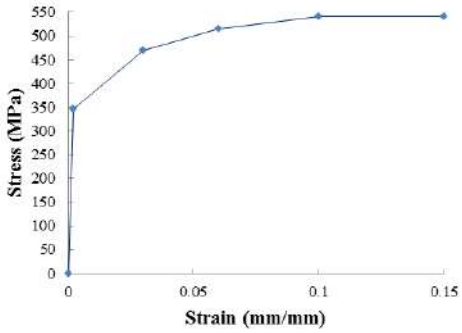

(a). Frame members.

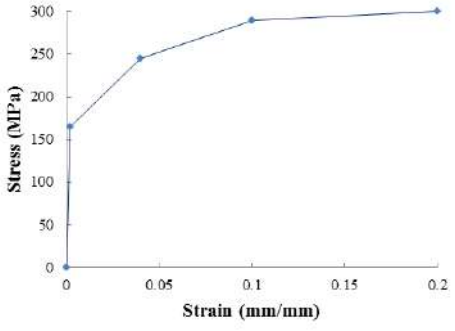

(b). Infill plates.

Fig. 3. Material stress-strain curve

4. Numerical modeling

The buckling and cyclic analyses of the models are conducted by ABAQUS. Nonlinear analysis of the models under static, quasi-static and dynamic loading is the ability of this software. The infill plate is modelled by the shell element and all the models are meshed by four node shell elements (S4R). For connecting the infill plate to the boundary elements the CONN2D3 (a kind of Contact which is available in the ABAQUS) is used. Some ties are used to connect the bottom of the column to the base hinge point that cannot move in all directions and cannot rotate around axes 2 and 3.

Behbahanifard et. al shows that the effect of the initial out of plane imperfection on the results can be neglected if it is limited to the $\because \times \sqrt{L \times h}$. To consider, the initial imperfection which is appeared by fault construction, at first, a buckling analysis is conducted to find the eigenvalue. The first plate buckling mode is multiplied on the too small displacement (for example 1 mm) and considered as an initial boundary condition for all models.

The plastic behaviour of the material is defined by combined hardening, which is included the kinematic and isotropic hardening. It is noticeable that using of the combined hardening is essential when study on the cyclic behaviour of the metals is the main objective. By this method, both the rigid movement of the system and its yield behaviour (the make the expansion and shortage) are considered.

5. Loading regime

The cyclic loading is defined base on the ATC 24 protocols [7]. For finding the yielding stress and its corresponding displacement and the ultimate stress, an axial buoyancy analysis is conducted. The goal displacement of the cyclic loading is considered equal to $\sqrt{\sigma_v}$. In Fig. 4. the amplitude is drown against the number of the cyclic of the loading. The other boundary condition is the same as the axial buoyancy analysis, completely.

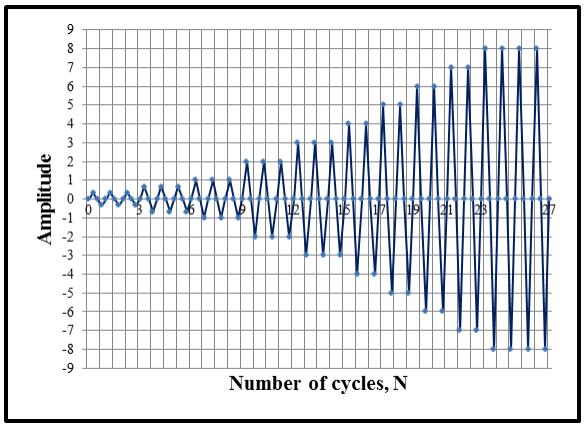

Fig. 4. Loading history

6. Validation and verification of results

Here, two SPSWs that modelled by Vian, Bruneau et al are analysed to evaluate the accuracy of the boundary condition and loading procedure. According to the Fig. 5, the numerical result is almost corresponded to the experimental ones.

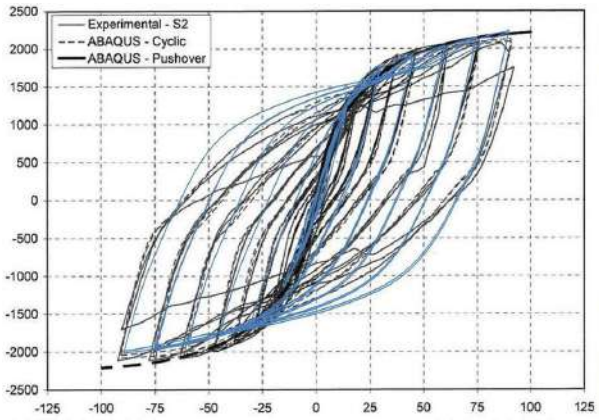

(a). SPSW with solid plate

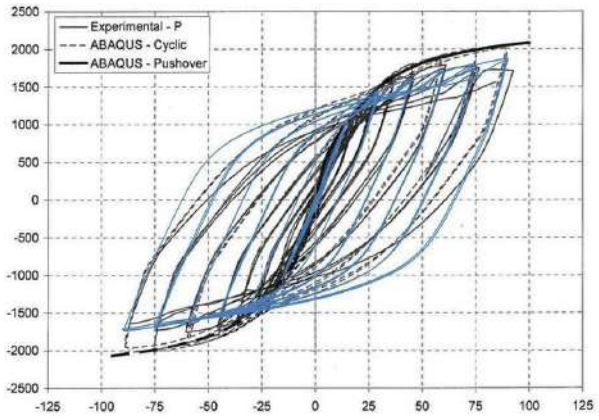

(b). SPSW with perforated plate

Fig. 5. Model hysteresis

In the Fig. 6 the deformation of the unstiffened steel plate shear wall, perforated steel plate shear wall (these models are presented by Vian, Bruneau previously) and the model 45°-28 are shown. In Figures 7 to 11, the force-displacement diagrams of each model are shown. In the table 1, the stiffness and strength of the models are presented. $V_{y.total}/V_{y.total}(S)$ and $K_{total}/K_{total.S}(S)$ are the stress and stiffness ratio of the system with perforated plate to the plate without any holes, respectively.

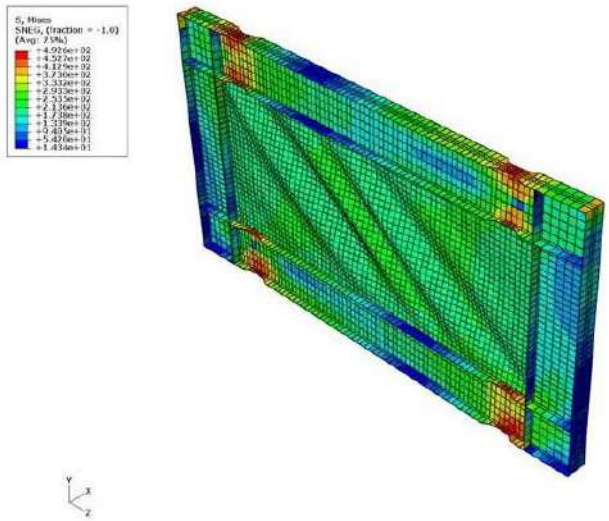

(a). SPSW with solid plate

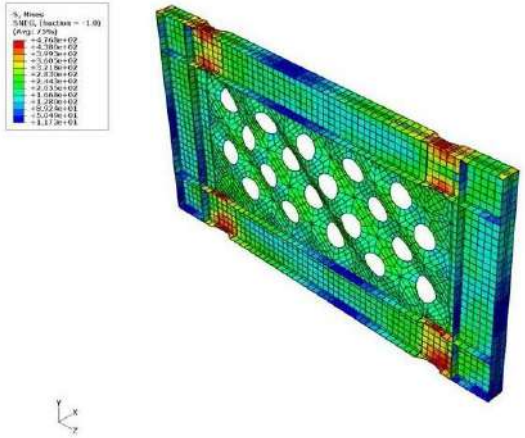

(b). SPSW with perforated plate

Fig. 6. Deformed shape of FE models at 3% drift (et al. Vian, Bruneau [19])

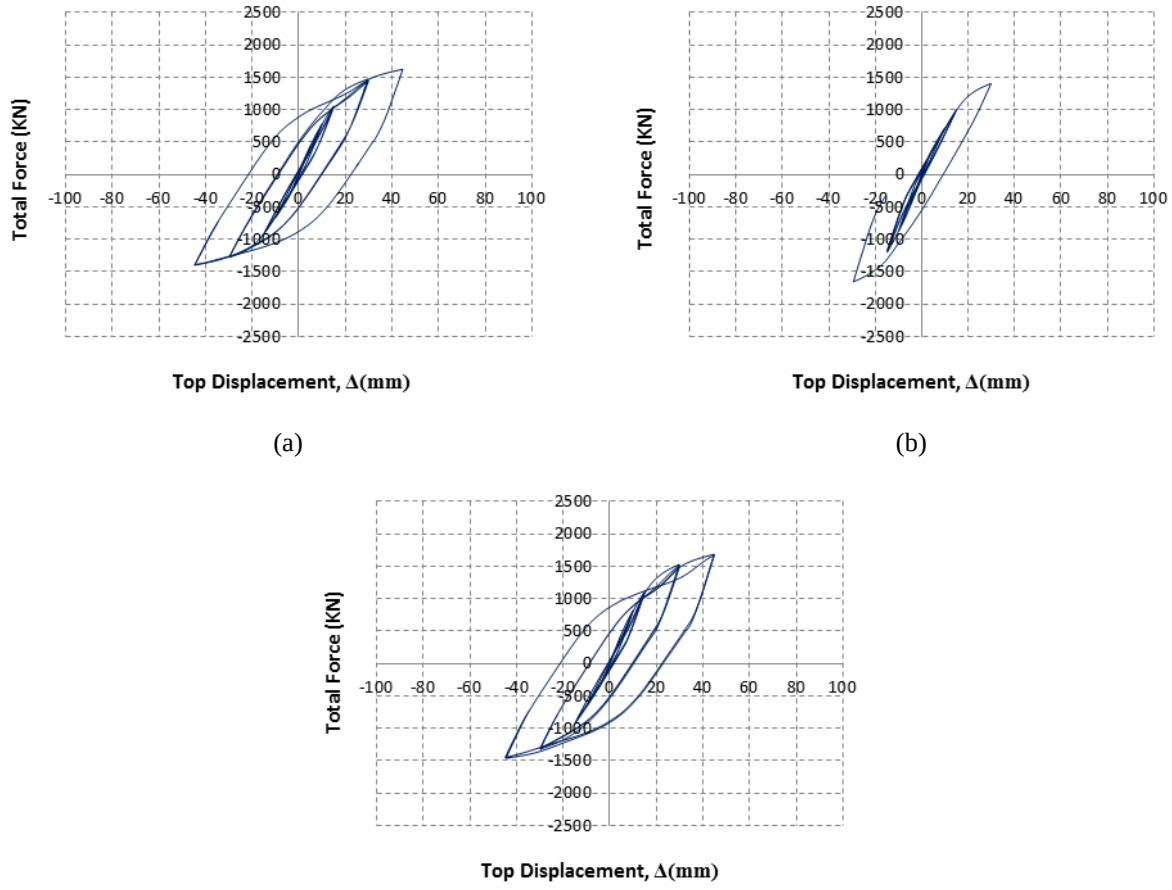

Fig. 7. Model hysteresis: (a) 30°-20, (b) 35°-20, (c) 40°-20

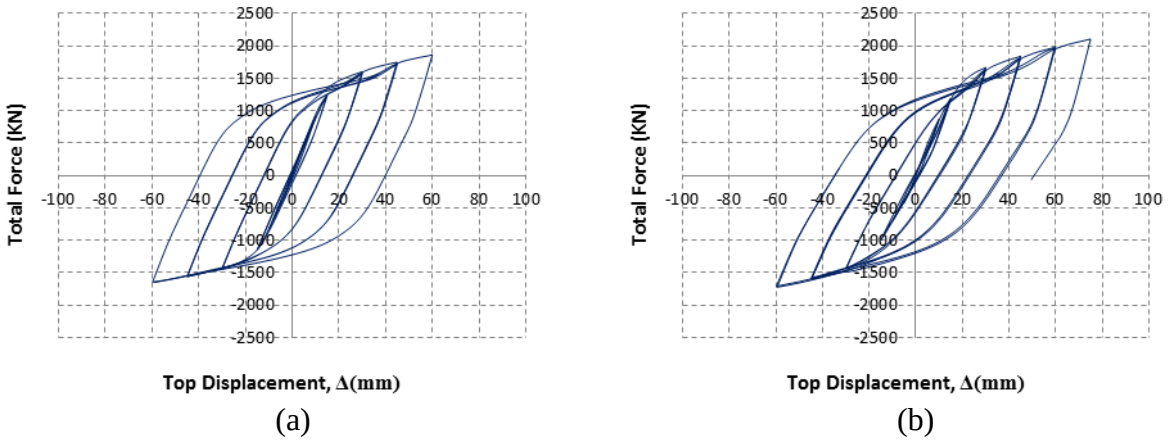

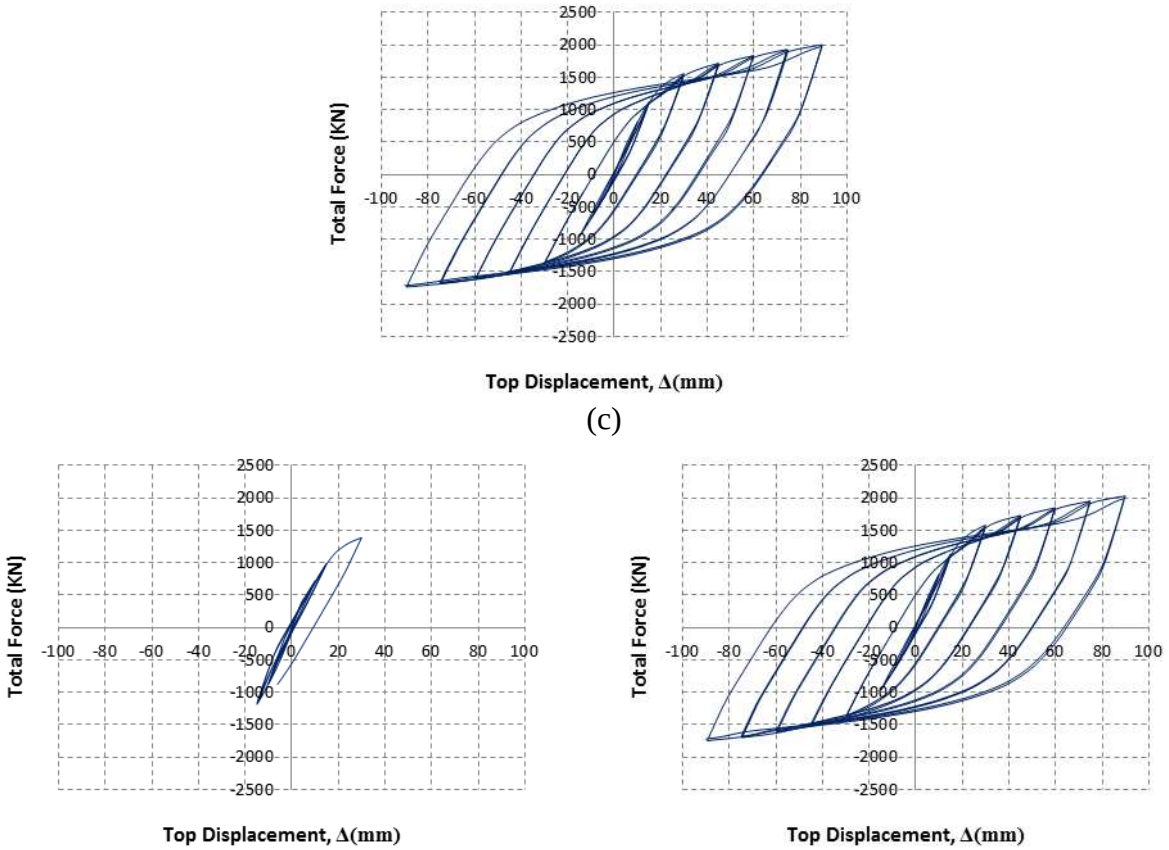

Fig. 8. Model hysteresis: (a) 45°-20-I, (b) 45°-20-II, (c) 45°-20-III, (d) 45°-27, (e) 45°-28

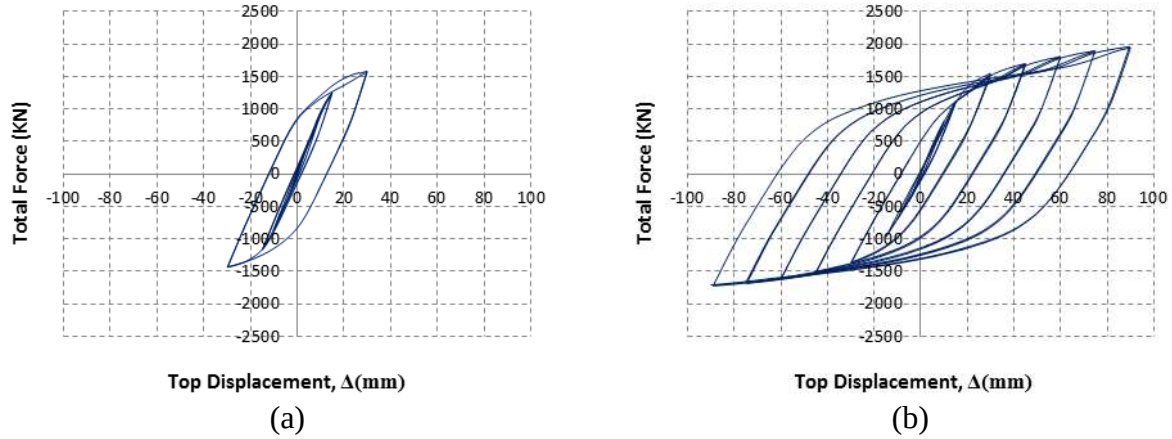

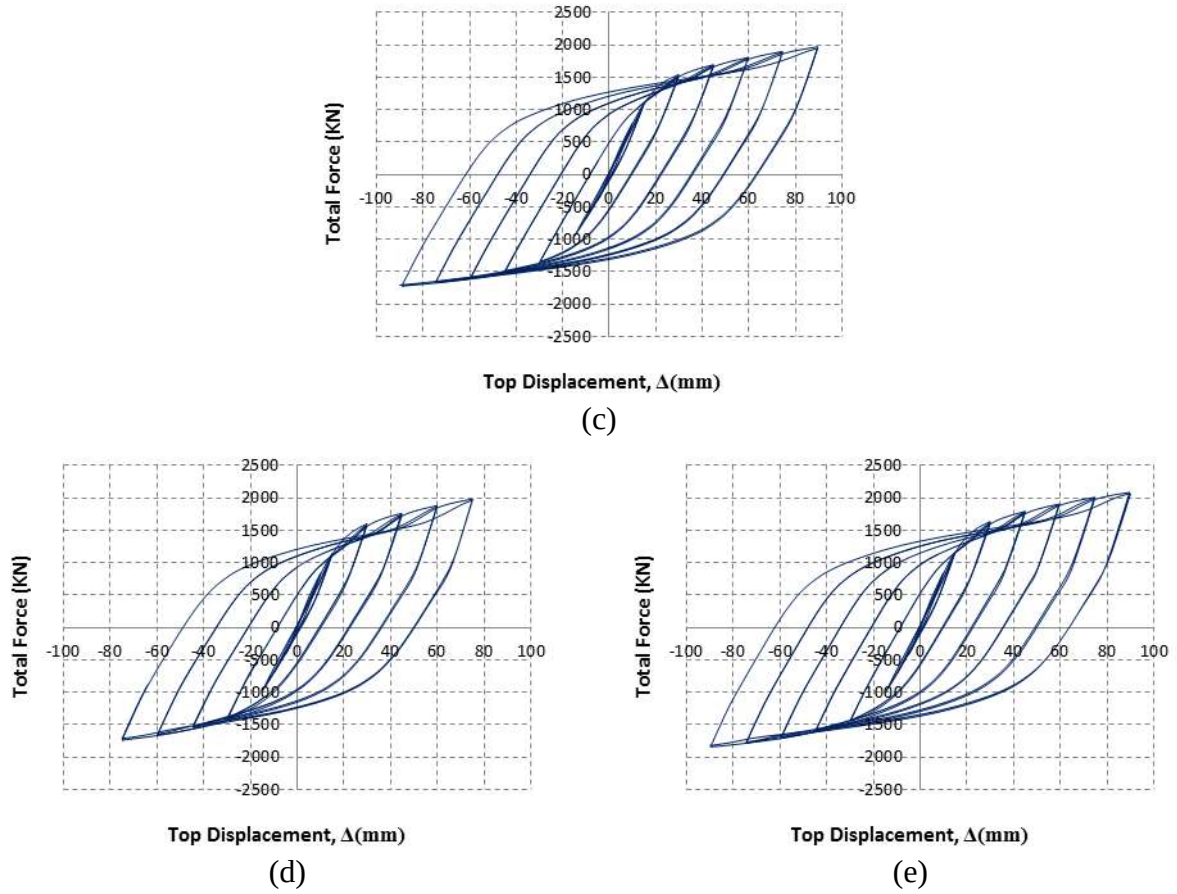

Fig. 9. Model hysteresis: (a) .50°-20-I, (b) .50°-20-II, (c) .50°-20-III, (d) .50°-27, (e) .50°-28

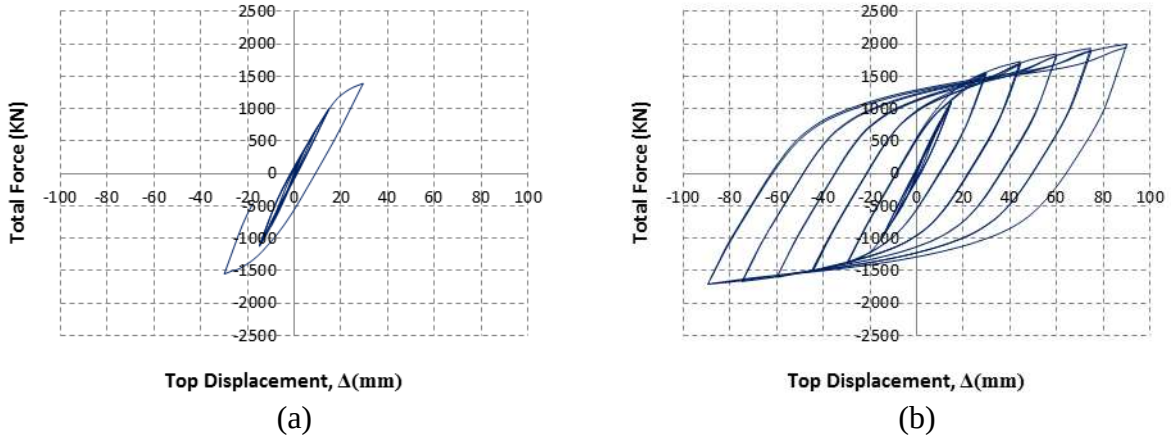

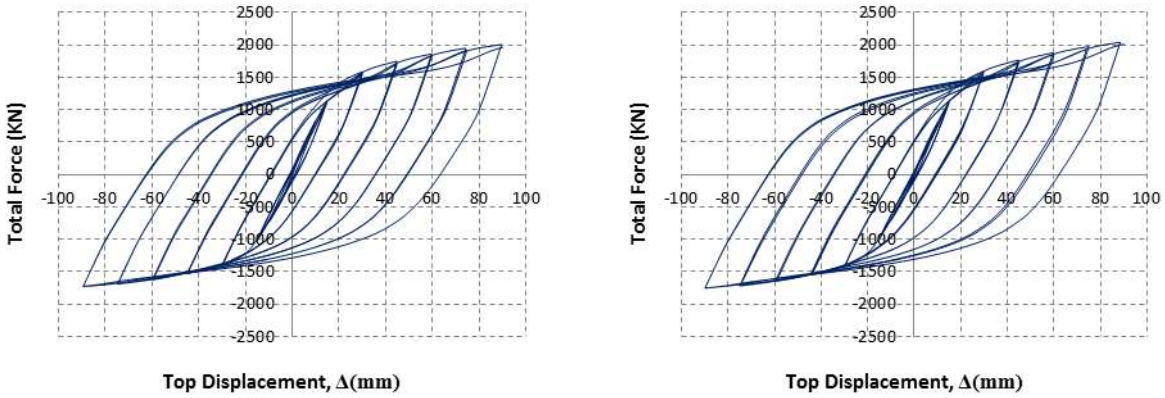

Fig. 10. Model hysteresis: (a) .55°-20-I, (b) .55°-20-II, (c) .55°-22, (d) .55°-23

7. Discussion of Results

Finding the proper pattern of the perforated plate in order to improve the energy absorption ability of the system is the main aim of this paper. According to the figures 7 to 11, Because of the suddenly collapse and reducing of the ultimate loading capacity in the initial cycles, the performance of the models is undesirable if the angle is smaller than 45. The hysteresis diagrams of the I ، 45°-20-II ، 45°-20-III ، 45°-27 and 45°-28 are shown in Fig. 8. By study in these models, it can find that when the perforated pattern is centrally symmetry with uniform distribution, the cyclic loops are more stable compare to the asymmetry and non-uniform ones (Fig. 13). A little bending will be induced in the transfer strip if the distribution of the holes is not uniform, so for the strip with asymmetry holes, based on eccentrically of the axial load, more stress is resulted on the same loading condition compare to the symmetry ones (Fig. 13).

The performance of the type II such as 45°-20-II ، 50°-20-II ، 55°-20-II ، 60°-20-II are better than the type I. But it is undesirable too because the distributions of the holes are not uniform.

Model 45°-20-III and 50°-20-III have a suitable performance under cyclic loading because the perforated pattern is centrally symmetry and the holes distribution are uniform unless near the columns. However it is noticeable that this pattern is not the optimum ones.

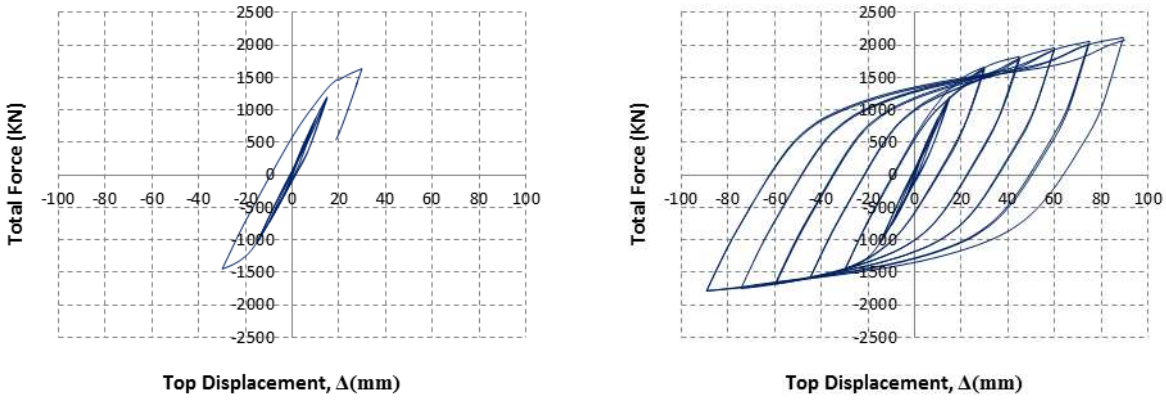

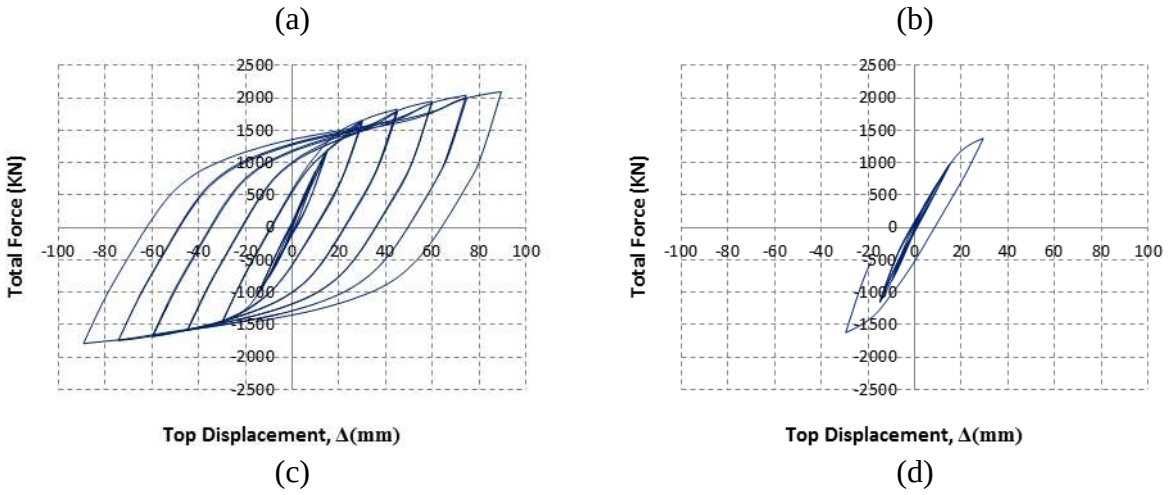

Fig. 11. Model hysteresis: (a) .60°-20-I, (b) .60°-20-II, (c) .60°-22, (d) .60°-23

However the distribution of the holes in models 45°-27, 50°-27, 55°-23 and 60°-23 are uniform, but they are not reasonable performance under cyclic loading because the transfer loading strip is not centrally symmetry (Fig. 13). So, after some initial cycles, the strength of the models will drop and the imperfect loop of energy absorption will be appeared. In models 45°-28, 50°-28, 55°-22 and 60°-22, the transfer strip is centrally symmetry, so the stable hysteresis loop will be formed. Moreover, the distributions of the holes are uniform; therefore the stress distribution will be uniform over the strip and the explained bending is removed. The performance of these models is appropriate under cyclic loading based on these reasons.

According to the table 1, the infill plate has a noticeable effect on the lateral stiffness of the system. And this effect is also seen in the perforated steel plate shear walls.

8. Conclusion

Recent studies show that the buckling of infill plate improves the energy absorption ability of the system. So using of too thin steel plate is essential that produce some construction problems. Using of a perforated steel plate shear wall can be an appropriate solution of this problem. But there is not any code that presented a pattern of the perforated plate. In this paper, for achieving to the suitable pattern of the holes location, 21 perforated steel plate shear walls are analysed under cyclic loading by ABAQUS. The results show that using of the centrally symmetry strip with uniform distribution lead to form of the more stable hysteresis loop compare to the un-symmetry strip with not uniform distribution of the holes. They also show that the angle between the direction of the holes line locations and the vertical axes should be equal or greater than the design angle of the steel plate shear wall (almost 45 degree).

Table 1

Comparison of peak result with simplified perforated panel models

Models	$\%V_{y.total}/V_{y.total}(S)$	$\%K_{total}/K_{total.5}(S)$	K_{Panel} (N/mm)	$\%K_{Panel.5}$
Solid	-	-	93749	-
30°-20	86.2	78.3	64331	68.6
35°-20	86.9	92.6	83710	89.3
40°-20	84	79	65272	69.6
45°-20-I	86.8	93.1	84391	90
45°-20-II	87.7	93.6	85114	90.8
45°-20-III	87.1	93.7	85277	91
45°-27	85.7	92	82850	88.4
45°-28	85.5	91.7	82532	88
50°-20-I	87.8	92.7	83860	89.4
50°-20-II	87.4	85	73521	78.4
50°-20-III	87.5	85.6	74258	79.2
50°-27	85.8	78.8	64999	69.3
50°-28	86.5	91.3	81985	87.4
55°-20-I	87	85.4	73937	78.9
55°-20-II	86.7	92.3	83271	88.8
55°-22	86.2	92.1	82991	88.5
55°-23	87.4	92.86	84059	89.7
60°-20-I	86	85.6	74256	79.2
60°-20-II	86.6	77.9	63776	68
60°-22	86.6	83	70621	75.3
60°-23	86.6	92.9	84157	89.7

Assume K_{Frame} =42 KN/mm, $K_{\text{Panel}} = K_{\text{Total}}$-$K_{\text{Frame}}$

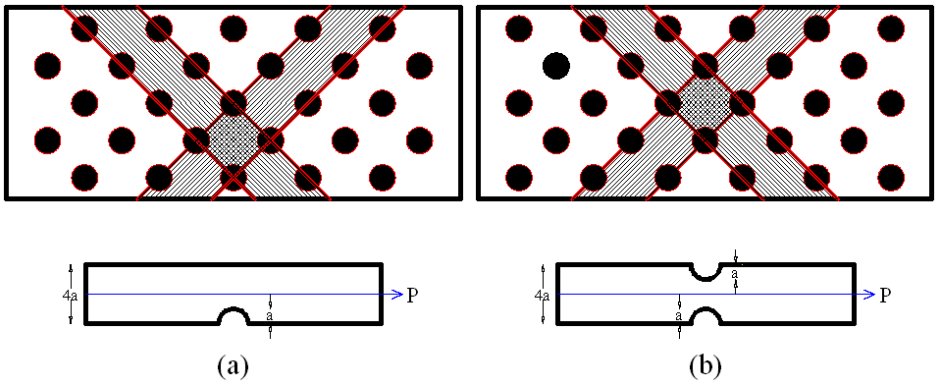

Fig. 13. (a). Unsymmetry ‘(b). Symmetry

References

[1] AISC (2005a), ANSI/AISC 341-05, Seismic Provisions for Structural Steel Buildings, American Institute of Steel Construction Inc., Chicago, IL.

[2] AISC (2005b), ANSI/AISC 360-05, Specification for Structural Steel Buildings, American Institute of Steel Construction Inc., Chicago, IL.

[3] AISC (2005c), ANSI/AISC 358-05, Prequalified Connections for Special and Intermediate Steel Moment Frames for Seismic Applications, American Institute of Steel Construction Inc., Chicago, IL.

[4] AISC-Design Guide 20-Steel plate shear walls (2007). American Institute of Steel Construction, Inc.

[5] A. Gheitasi, M.M. Alinia, (2010). "Slenderness classification of unstiffened metal plates under shear loading," Thin-Walled Structures. Vol 48 pp.508-518

[6] Appendix M, CSA, Standard-CAN/CSA-S16.1-94 (S16.1) Canada's National Standard for Limit States Design of Steel Structures, December 1994.

[7] ATC (1992), Guidelines for Seismic Testing of Components of Steel Structures, Applied Technology Council, Report 24.

[8] Behbahanifard, M. R. (2003). "Cyclic behaviors of unstiffened steel plate shear walls." Ph.D. dissertation, Dept. of Civil Engineering, Univ of Alberta, Edmonton, Alberta, Canada.

[9] Berman, J.W. and Bruneau, M. (2003b), "Experimental Investigation of Light-Gauge Steel Plate Shear Walls for the Seismic Retrofit of Buildings", Technical Report MCEER-03-0001, Multidisciplinary Center for Earthquake Engineering Research, Buffalo, NY.

[10] Bruneau, M. and Bhagwagar, T., (2002). "Seismic Retrofit of Flexible Steel Frames Using Thin Infill Panels", Engineering Structures 24, pp. 443-453.

[11] Driver, R. G. and Kulak, G. L. and Kennedy, D. J. L. and Elwi, A. E., (1998). "Cyclic Test of Four-Story Steel Plate Shear Wall", Struct. Eng, Vol 124., No2., February.

[12] Roberts, T. M. and Sabouri-Ghomi, S., (1991). "Hysteretic Characteristics of Unstiffened Plate Shear Panels", Thin-Walled Structures 12.

[13] Roberts, T. M. and Sabouri-Ghomi, S., "Hysteretic Characteristics of Unstiffened Perforated Steel Plate Shear Panels".

[14] Vian, D., and Bruneau, M. (2005). "Steel plate shear walls for seismic design and retrofit of building structures." Tech. Rep. No. MCEER- 05–0010, Multidisciplinary Center for Earthquake Engineering Research, State Univ. of New York at Buffalo, Buffalo, N.Y.

[15] Vian, D., and Bruneau, M. (2004), "Testing of Special LYS Steel Plate Shear Walls", Proceedings of the 13th World Conference on Earthquake Engineering, Paper No. 978, Vancouver, British Columbia, Canada, August 1- 6, 2004.

[16] Vian, D., and Bruneau, M. (2005). "Steel plate shear walls for seismic design and retrofit of building structures." Tech. Rep. No. MCEER- 05–0010, Multidisciplinary Center for Earthquake Engineering Research, State Univ. of New York at Buffalo, Buffalo, N.Y.

[17] Vian, D., and Bruneau, M. (2004), "Testing of Special LYS Steel Plate Shear Walls", Proceedings of the 13th World Conference on Earthquake Engineering, Paper No. 978, Vancouver, British Columbia, Canada, August 1-6, 2004.

[18] Vian, D., Bruneau, M., Tsai, K. C., and Lin, Y.-C. (2009). "Special perforated steel plate shear walls with reduced beam section anchor beams. I: Experimental investigation." J. Struct. Eng. 135_3_.

[19] Darren Vian, M.ASCE; Michel Bruneau, M.ASCE; and Ronny Purba. "Special Perforated Steel Plate Shear Walls with Reduced Beam Section Anchor Beams. II: Analysis and Design Recommendations", Journal of Structural Engineering, Vol. 135, No. 3, March 1, 2009.

Author Guidelines EditEdit Author Guidelines

GENERAL GUIDELINES FOR AUTHORS

Journal of civil engineering researches invites unsolicited contributions of several forms: articles, reviews and discussion articles, translations, and fora. Contributions should fall within the broad scope of the journal, as outlined in the statement of scope and focus. Contributors should present their material in a form that is accessible to a general anthropological readership. We especially invite contributions that engage with debates from previously published articles in the journal.

Submissions are double-blind peer-reviewed in accordance with our policy. Submissions will be immediately acknowledged but due to the review process, acceptance may take up to three months. Submissions should be submitted via our website submission form (see links above for registration and login). Once you login, make sure your user profile has "author" selected, then click "new submission" and follow the instructions carefully to submit your article. If problems arise, first check the FAQ and Troubleshooting guide posted below. If you are still experiencing difficulty, articles can be submitted to the editors as email attachments.

Each article should be accompanied by a title page that includes: all authors' names, institutional affiliations, address, telephone numbers and e-mail address. Papers should be no longer than 10,000 words (inclusive of abstract 100-150 words, footnotes, bibliography and notes on contributors), unless permission for a longer submission has been granted in advance by the Editors. Each article must include a 100 words "note on contributor(s)" together will full institutional address details, including email address. We request that you submit this material (title page and notes on the contributors) as "supplementary files" rather than in the article itself, which will need to be blinded for peer-review.

We are unable to pay for permissions to publish pieces whose copyright is not held by the author. Authors should secure rights before submitting translations, illustrations or long quotes. The views expressed in all articles are those of the authors and not necessarily those of the journal or its editors. After acceptance, authors and Special Issue guest editors whose institutions have an Open Access library fund must commit to apply to assist in article production costs. Proof of application will be requested. Though publication is not usually contingent on the availability of funding, the Journal is generally under no obligation to publish a work if funding which can be destined to support open access is not made available.

Word template and guidelines

Our tailored Word template and guidelines will help you format and structure your article, with useful general advice and Word tips.

(La)TeX template and guidelines

We welcome submissions of (La)TeX files. If you have used any .bib files when creating your article, please include these with your submission so that we can generate the reference list and citations in the journal-specific style

Artwork guidelines

Illustrations, pictures and graphs, should be supplied with the highest quality and in an electronic format that helps us to publish your article in the best way possible. Please follow the guidelines below to enable us to prepare your artwork for the printed issue as well as the online version.

Format: TIFF, JPEG: Common format for pictures (containing no text or graphs).

EPS: Preferred format for graphs and line art (retains quality when enlarging/zooming in).

Placement: Figures/charts and tables created in MS Word should be included in the main text rather than at the end of the document.

Figures and other files created outside Word (i.e. Excel, PowerPoint, JPG, TIFF, EPS, and PDF) should be submitted separately. Please add a placeholder note in the running text (i.e. "[insert Figure 1.]")

Resolution: Rasterized based files (i.e. with .tiff or .jpeg extension) require a resolution of at least 300 dpi (dots per inch). Line art should be supplied with a minimum resolution of 800 dpi.

Colour: Please note that images supplied in colour will be published in colour online and black and white in print (unless otherwise arranged). Therefore, it is important that you supply images that are comprehensible in black and white as well (i.e. by using colour with a distinctive pattern or dotted lines). The captions should reflect this by not using words indicating colour.

Dimension: Check that the artworks supplied match or exceed the dimensions of the journal. Images cannot be scaled up after origination

Fonts: The lettering used in the artwork should not vary too much in size and type (usually sans serif font as a default).

Authors services:

For reformatting your manuscript to fit the requirement of the Journal of Civil Engineering Researchers and/or English language editing please send an email to the following address:

researchers.services@gmail.com

Noted: There is a fixed charge for these mentioned services that is a function of the manuscript length. The amount of this charge will be notified through a reply email.

FAQ AND TROUBLESHOOTING FOR AUTHORS

I cannot log in to the system. How do I acquire a new user name and password?

If you cannot remember your username, please write an email to (journals.researchers@gmail.com), who will locate your username and notify you. If you know your username, but cannot remember your password, please click the "Login" link on the left-hand menu at homepage. Below the fields for entering your username and password, you will notice a link that asks "Forgot your password?"; click that link and then enter your email adddress to reset your password. You will be sent an automated message with a temporary password and instructions for how to create a new password. TIP: If you do not receive the automated email in your inbox, please check your SPAM or Junk Mail folder. For any other issues, please contact our Managing Editor,Kamyar Bagherinejad (admin@journals-researchers.com).

How do I locate the online submission form and fill it out?

First you need to register or login (see above). Once you are logged in, make sure the "roles" section of your profile has "Author" selected. Once you assign yourself the role of "Author," save your profile and then click the "New Submission" link on your user home page.

Once you arrive at the submission form page, please read the instructions carefully filling out all necessary information. Unless specified otherwise by the editors, the journal section to be selected for your submission should be "Artlcles." Proceed to the remaining sections, checking all boxes of the submission preparation checklist, and checking the box in the copyright notice section (thus agreeing to journals-researchers's copyright terms). Once the first page is completed, click "Save and Continue." The next page allows you to upload your submission. Use the form to choose your file from your computer. Make sure you click "Upload." The page will refresh and you may then click "Save and Continue." You will then proceed to a page for entering the metadata for your article. Please fill out all required fields and any further information you can provide. Click "Save and Continue." The next page allows you to upload supplementary files (images, audiovisual materials, etc.). These are not required, but if you wish to provide supplementary materials, please upload them here (do no forget to click "Upload." Then click "Save and Continue." This brings you to the final page of the submission form. Please click "Finish Submission" in order to close the

submission process. You wil then be notified by email that your article has been successfully submitted. TIP: If you do not receive the automated email in your inbox, please check your SPAM or Junk Mail folder. For any other issues, please contact our Managing Editor, Kamyar Bagherinejad (admin@journals-researchers.com).

Why am I not receiving any email notifications from HAU?

Unfortunately, some automated messages from Open Journal Systems arrive in users' Spam (or Junk Mail) folders. First, check those folders to see if the message was filtered into there. You may also change the settings of your email by editing your preferences to accept all mail from [jcer] and related journals-researchers.com email accounts.

I am trying to upload a revised article following an initial round of peer-review, but I cannot locate where to upload the article. Where do I submit a revised article?

Follow the login process outlined above and when you successfully login you will see on your user home page a link next to "Author" for "active" articles in our system (usually it is only one article, but if you have mulitple submissions currently in our system, the number could be higher. Click the "Active" link and you will be led to a page that lists your authored articles currently in our system. Click the link under the column labeled "Status" and this will take you to a page showing the current review status of your article. At the very bottom of the screen, you will see an upload form under the heading "Editor decision." Here you may upload your revised article. An automated email will be sent to the editors and you may also notify them directly via email. You may then logout.

I successfully submitted an article; how long will it take for the editors to respond to me with a decision.

For all articles that are recommended for peer-review, the editors of JCER strive to notify authors of a decision within 4-6 weeks. You may contact JCER's Managing Editor, Kamyar Bagherinejad (admin@journals-researchers.com). if you have any questions relating to the review process and its duration.

For all other inquiries, please contact: Kamyar Bagherinejad (Managing Editor)

Privacy Statement

The names and email addresses entered in this journal site will be used exclusively for the stated purposes of this journal and will not be made available for any other purpose or to any other party.

Articles

Section default policy

Make a new submission to the Articles section.

Copyright Notice EditEdit Copyright Notice

Journal of Civil Engineering Researchers follows the regulations of the International Committee on Publication Ethics (COPE) and the ethical principles of publishing articles in this journal are set based on the rules of this committee, and in case of problems, it will be treated according to these rules.

Privacy Statement EditEdit Privacy Statement

The names and email addresses entered in this journal site will be used exclusively for the stated purposes of this journal and will not be made available for any other purpose or to any other party.

Scholars Pavilion

Scholars Pavilion or **Scholars Chartagi** is a monument donated by the Islamic Republic of Iran to the United Nations Office at Vienna. The monument architecture is claimed by the Islamic Republic News Agency of Iran to be a combination of Islamic and Achaemenid architecture, although the latter clearly predominates in the decorative features, with Persian columns and other features from Persepolis and other remains from the Achaemenid dynasty. The Chahartaq pavilion form runs through the architecture of Persia from pre-Islamic times to the present.

Statues of four famous Persian medieval scholars, Omar Khayyam, Al-Biruni, Muhammad ibn Zakariya al-Razi and Ibn-Sina are inside the pavilion. This monument donated in June 2009 in occasion of Iran's peaceful developments in science.

J-Researchers